



Title	Growth of MoS ₂ Nanowires by Catalytic Chemical Vapor Deposition
Author(s)	WENG, Mengting
Citation	北海道大学. 博士(総合化学) 甲第13226号
Issue Date	2018-03-22
DOI	10.14943/doctoral.k13226
Doc URL	http://hdl.handle.net/2115/69947
Type	theses (doctoral)
File Information	Mengting_Weng.pdf



[Instructions for use](#)

**Growth of MoS₂ Nanowires by
Catalytic Chemical Vapor Deposition**

WENG Mengting

Hokkaido University

2018

Content

Chapter 1. General Introduction	1
1.1 One-dimensional semiconductor nanostructures	1
1.2 1D MoS ₂ nanostructures	3
1.3 Growth mechanism of catalytic CVD	6
1.3.1 VLS mechanism	7
1.3.2 VSS growth mechanism	8
1.3.3 VS growth mechanism.....	9
1.4 The aim of this study	10
References	11
Chapter 2. Catalysts for the growth of MoS₂ nanowires	17
2.1 Introduction	17
2.2 Experimental section	18
2.2.1 Synthesis	18
2.2.2 Characterization.....	20
2.3 Results and discussion.....	20
2.3.1 Search for the catalysts	20
2.3.2 Catalytic activities of other metal oxides	23
2.4 Conclusions	28

References	28
Chapter 3. Synthesis of MoS₂ nanowires by chemically synthesized FeO nanoparticles.....	32
3.1 Introduction	32
3.2 Experimental section.....	33
3.2.1 Synthesis.....	33
3.2.2 Characterization.....	35
3.3 Results and discussion.....	35
3.3.1 FeO nanoparticles	35
3.3.2 MoS ₂ nanowires.....	38
3.4 Conclusions	50
References	50
Chapter 4. Size and shape effects of catalyst nanoparticles	54
4.1 Introduction	54
4.2 FeO nanoparticles.....	55
4.2.1 Synthesis.....	56
4.2.2 OA/OAm ratio	57
4.2.3 Decomposition temperature.....	58
4.2.4 Deposition time.....	61
4.3.5 Stirring	62

4.3 Shape effect of the catalysts	63
4.4 Size effect of the catalysts	74
4.5 Conclusions	77
References	77
Chapter 5. Other factors for the MoS₂ nanowires control.....	81
5.1 Introduction	81
5.2 Surface pretreatments of the substrates	81
5.2.1 Plasma deposition of Al ₂ O ₃	82
5.2.2 Plasma etching	85
5.2.3 Chemical etching in alkaline solution	87
5.2.4 Carbon coating	89
5.3 Growth temperature.....	93
5.4 Growth time.....	95
5.5 Conclusions	96
References:	97
Chapter 6. General Conclusions.....	101

Chapter 1. General Introduction

1.1 One-dimensional semiconductor nanostructures

Semiconductor materials have been widely used in photonic, electronic, energy and magnetism related applications [1-10]. Recently, semiconductor nanostructures have gained enormous attentions, due to their important roles played in electronic circuit miniaturization [1]. Compared to their bulk materials, the semiconductor nanostructures have novel and unique properties in catalytic [2-4], electronic [5-7] and optoelectronic [8-10] applications, which are attributed to the size confinement effects caused by their nanoscale structures confined in several dimensions. Classified by their dimensionality, the semiconductor nanostructure materials could be divided into 0-dimensional (such as quantum dots, nanoparticles and nanospheres), 1-dimensional (such as nanowires, nanotubes and nanobelts), 2- dimensional (such as nanosheets, nanoplates and nanodisks) and 3-dimensional (such as nanoballs, nanoflowers and nanocones) materials according to the classification scheme reported by Pokropivny and Skorokhod [11].

The interest in 1D semiconductor materials has been emerged over the past three decades due to their unique and peculiar properties [12-17]. For examples, the quantum confinement in racial direction makes the 1D nanostructure materials strong candidates in the application of photovoltaic devices [12-14]. The high surface-to-volume ratios and the nanoscale sizes of the 1D nanostructure materials enable them to the use in sensor devices [15-17]. To date, vast numbers of 1D semiconductor materials have been fabricated and utilized in device applications, such as the carbides [18-20], metal nitrides [21-23],

sulphides [24-26] and oxides [27-29]. Several types of the 1D material are shown in Figure 1-1: nanowires, nanoribbons, nanobelts and nanotubes [1].

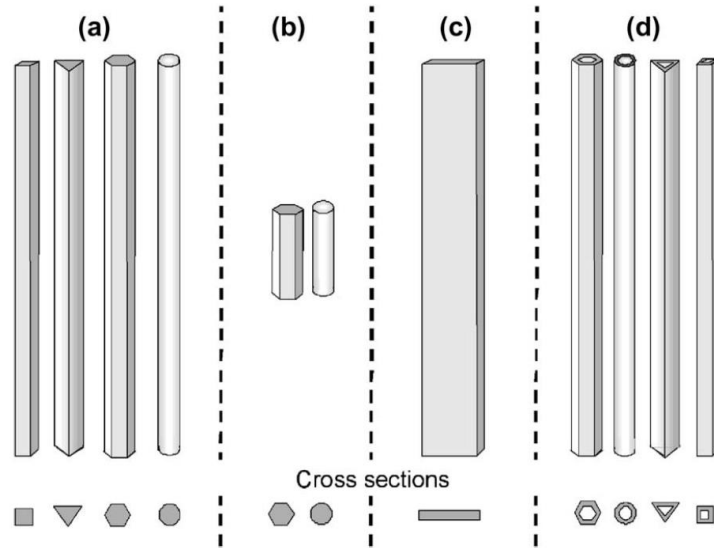


Figure 1-1. Several types of the 1D material: (a) nanowires, (b) nanoribbon, (c) Nanobelts and (d) nanotubes. [1]

Carbon nanotube is one of the most widely known 1D nanostructures. Since the first observation of multi-walled carbon nanotubes by Iijima in 1991 [30], numerous studies have been focused on the synthesis, properties and applications of the carbon nanotubes due to their remarkable physical and chemical properties[31-33]. The structure of the nanotubes can be visualized as rolled sheets of graphite as shown in Figure 1-2(a) [34]. According to the wrapping angles of the sheets, the nanotubes can be classified into zigzag, armchair and chiral nanotubes as shown in Figure 1-2 (b) [34]. The physical properties of the carbon nanotubes are primarily dependent on the chirality of the nanotubes [35-38]. For example, the nanotubes exhibit different conductivities according to the three types of nanotube chirality. All the armchair nanotubes are metallic in conductivity while this is only in the case with chiral or zigzag nanotubes when $(n-m)/3$ is an integer, otherwise they

are semiconductor [38]. However, it is difficult to control the chirality of the carbon nanotube, even though various researches have been made attempting to grow the carbon nanotube in a controlled manner [39-41]. Thus, the interest in similar inorganic structures such as WS₂ [42-44], MoS₂ [45-51] and BN [52-54], has been emerged due to their structures analogous to carbon nanotubes.

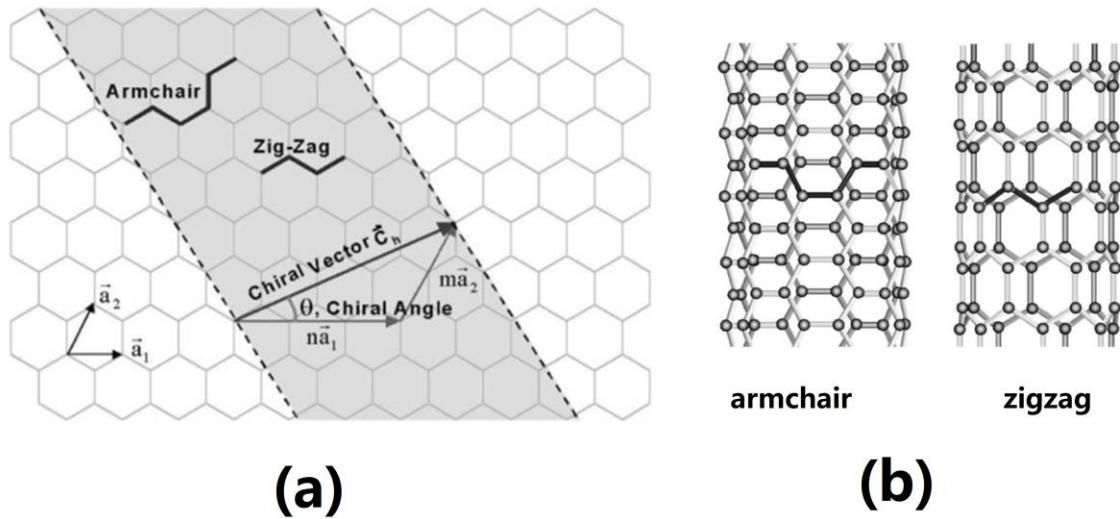


Figure 1-2. (a) Scheme of the roll direction of graphite hexagonal sheets. (b) Atomic structure of the carbon nanotubes. [34]

1.2 1D MoS₂ nanostructures

1D MoS₂ and WS₂ nanostructures can be obtained by the roll up of 2D transition metal dichalcogenides (TMDCs), in a similar way to the formation of carbon nanotubes. TMDCs are materials with MX₂ formulae, where M is a transition metal atom from group IV-VI (for instance Ta, Nb or Mo) and X is a chalcogen atom (S, Se or Te). The layered structure of X-M-X form is a sandwich structure with one layer of metal atoms and two layers of

chalcogen atoms [55]. With the different composition of the TMDC materials, the electronic properties are ranging from metallic to semiconducting, as shown in Table 1-1 [55]. From the table, it is obvious that all the structures of MoS₂ and WS₂ exhibit semiconductor properties.

Table1-1. Summary of the electronic characteristics of TMDCs [55].

	Nb	Ta	Mo	W
	Electronic characteristics			
-S ₂	Metal; superconducting; CDW	Metal; superconducting; CDW	Semiconducting 1L: 1.8 eV Bulk: 1.2 eV	Semiconducting 1L: 2.1 eV 1L: 1.9 eV Bulk: 1.4 eV
-Se ₂	Metal; superconducting; CDW	Metal; superconducting; CDW	Semiconducting 1L: 1.5 eV Bulk: 1.1 eV	Semiconducting 1L: 1.7 eV Bulk: 1.2 eV
-Te ₂	Metal	Metal	Semiconducting 1L: 1.1 eV Bulk: 1.0 eV	Semiconducting 1L: 1.1 eV

As a representative material, the structure of MoS₂ is formed by one layer of Mo atoms sandwiched by two layers of S atoms, as shown in Figure 1-3 (a) [55]. MoS₂ nanotubes or nanowires, the similar structures to carbon nanotubes, are rolled up by the layers of MoS₂. The armchair and zigzag nanostructures are shown in Figure 1-3(b) [56].

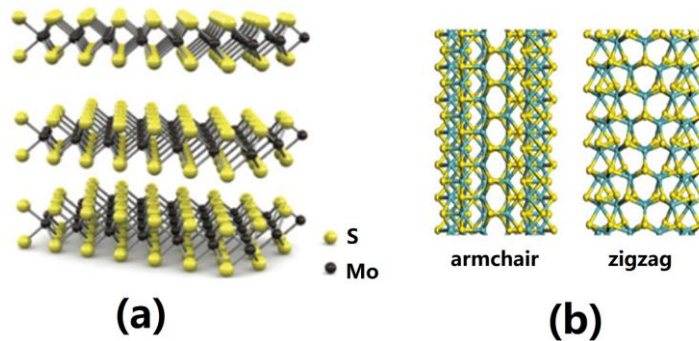


Figure 1-3. (a) Structure of MoS₂ [55] and (b) atomic structures of MoS₂ nanotubes [56].

1D MoS₂ nanostructures can be used in a wide application due to their intriguing physical and chemical properties. For examples, in the application of field effect transistor (FET), 1D MoS₂ nanostructures can be good candidates due to their large on/off ratio [57] and high mobility. In the application of sensors, the high sensitivity and the stability make them as better choices than Si or GaAs, because of no capping layers on the surface. In the application of lubricants, the excellent lubrication and the one-dimensionality enable it to promote lubrication when used in composites. Several methods have been used to grow the 1D MoS₂ nanostructures [45-51].

Template method [45, 46]: Peter K. Dorhout et al have synthesized the tubules and fibers of MoS₂ by using a porous aluminum oxide (Al₂O₃) template with the precursors of (NH₄)₂MoS₄ and (NH₄)₂Mo₃S₁₃ [45]. The diameter of MoS₂ tubules and fibers can be obtained in 50 or 330 nm and the length can be up to 30 μm; however, the bamboo structure can be found by HRTEM. The factors related to this interesting structure have been investigated by Rivera-Munoz in 2007 [46].

Catalytic transport reaction [47, 48]: Remskar et al have reported to fabricate single-walled MoS₂ nanotubes by transported method with C₆₀ as the catalyst in 2001[47]. The source material in this method was MoS₂ and the spent time was 22 days. An important development of the method has been made in 2011[48]. The improved method was separated into two steps. First was the fabrication of the Mo₆S₄I₆ precursor nanowires. It was synthesized by transporting the vapor of Mo, sulfur and I₂ into an evacuated quartz ampoules. The second step was the sulfurization of the precursor nanowires by the Ar gas mixed with H₂S and H₂. The time for the preparation of the nanowires was at least 2 days.

Thermal decomposition [49]: Tremel et al have synthesized the MoS₂ nanotubes by H₂S reduction of the mixture of MoO₃ and Mo_{5.3}O_{14.5} (OH)_{2.8}(H₂O)_{1.36}. The MoS₂ nanotubes were obtained by this method from the sulfurization of the rod-like MoO₃.

Hydrothermal treatment [50]: G. Gonzalez et al have synthesized the MoS₂ nanotubes by the hydrothermal treatment of the Li_{0.1}MoS₂(HAD) and Li_{0.1} MoS₂(ODA). The nanotubes synthesized by this method were mixed with MoS₂ lamella.

Nevertheless, these methods are still limited in terms of the growth control of the high-quality MoS₂ nanotubes or nanowires. Thus, new approaches are needed to be developed. Catalytic chemical vapor deposition (CVD) has been reported to produce high selective yield of single-chirality carbon nanotubes by using a catalyst with high melting points, which can maintain their crystal structures during the high-temperature experimental process [58-60]. Since CVD have been widely used in the synthesis of MoS₂ monolayers or thin films [61, 62], the catalytic CVD seems to be a feasible method to fabricate MoS₂ nanotubes or nanowires.

1.3 Growth mechanism of catalytic CVD

Catalytic CVD is a method to fabricate the 1D nanostructure materials using solid catalysts [58-60]. Slight changes in shape or composition of the catalysts used in the synthesis process will have an influence on nucleation and growth of the products, leading to the formation of different structures. Thus, it is essential to have a fundamental understanding of their growth mechanism.

Since the method we used is CVD, the source materials are in vapor phase, suggesting the major growth mechanism in the catalytic CVD is vapor-liquid-solid (VLS) [63-68], vapor-solid-solid (VSS) [69-70] and vapor-solid (VS) [71, 72].

1.3.1 VLS mechanism

In the name of the VLS, “V” is the vapor phase of the precursor materials, “L” is the formation of liquid alloy droplets and “S” is the precipitation of the 1D nanostructures. The process of the VLS mechanism is described briefly as follows and the schematic process is shown in Figure 1-4 [63]:

- (1) The gaseous reactants will be dissolved into the catalytic nanoparticles to form liquid alloy droplets.
- (2) The nucleation of the nanowires will be induced by the supersaturation of the liquid alloy droplets.
- (3) The 1D nanostructures will be precipitated and grown from the supersaturated liquid alloy droplets.

One of the most important steps in the process of VLS is the formation of liquid alloy droplets. Thus, finding an appropriate catalyst for the precursor materials is crucial in the VLS method.

This process has been widely employed in the synthesis of 1D nanostructures, such as the SiO₂ [64], SiC [65], ZnS [66] and GaN [67], since the first found in the growth of Si whiskers by Wagner and Ellis in 1960s [68]. The size of the 1D nanostructures synthesized by VLS mechanism can be controlled in various ways. For examples, the length of the

nanowires can be controlled by the modulation in growth time; the nanowire diameter can be controlled by using the different sizes of the catalyst.

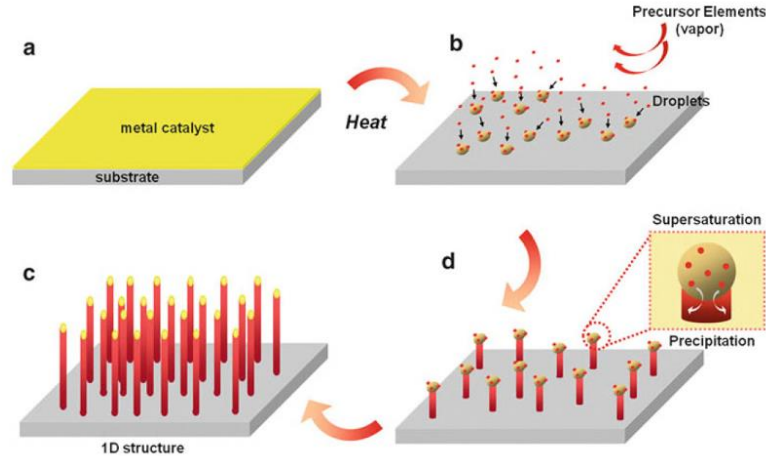


Figure 1-4. Scheme of the VLS process [63].

1.3.2 VSS growth mechanism

In the name of VSS, “V” is the vapor phase of the precursor materials, the first “S” is the solid catalytic nanoparticles and the second “S” is the precipitation of the 1D nanostructures. The process of VSS growth mechanism is described as follows and the schematic process is shown in Figure 1-5 [69]:

- 1) The gaseous reactants will be delivered to the surface of the catalytic nanoparticles and the precursor materials will be decomposed at the growth temperature;
- 2) The atoms by the decomposition of the precursor material will be delivered to the interface between the catalyst nanoparticle and the nanowire by diffusion process;
- 3) The 1D nanostructures will be grown by the atoms incorporated at the interface.

The application of VSS mechanism mainly focused on the growth of Si and Ge [69, 70] nanowires. It required that the precursor materials must be decomposed to some degree to provide sufficient atoms deposited on the surface of catalytic nanoparticles. In both VLS and VSS growth mechanism, the nanoparticle caps could be observed at the top of 1D nanostructures. In VLS growth, the particles are round due to the formation of liquid alloy droplets, while in VSS growth, the abrupt interface could be observed in the nanoparticles. Compared to the VLS growth, some advantages of the VSS growth need to be considered [69, 70].

- (1) The growth temperature in VSS mechanism is lower than the eutectic temperature of the catalytic nanoparticles and the precursor materials;
- (2) The growth direction of the 1D nanostructures can be better controlled;
- (3) The 1D nanostructures will have more abrupt interfaces.

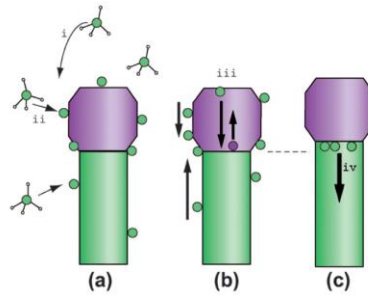


Figure 1-5. Scheme of the VSS process [69].

1.3.3 VS growth mechanism

Many plausible growth mechanisms in the growth of 1D nanostructures are considered to be VS growth mechanism [71, 72]. The process of VS growth mechanism is described as follows:

- (1) The gaseous reactants will deposit on the surface of the catalytic nanoparticles to form nucleation sites;
- (2) The 1D nanostructures will be grown by the continued supply of the precursor materials.

It requires that (1) sufficient vapor of precursor materials; (2) screw dislocation or defects can be found on the surface of the nanoparticles.

1.4 The aim of this study

As introduced in the general introduction, 1D MoS₂ nanostructures can be widely used due to their similar structure to carbon nanotubes. However, little attention has been paid on the growth of 1D MoS₂ nanostructures. Thus, I planned to synthesize MoS₂ nanowires by catalytic CVD method.

Firstly, I searched the effective catalyst for the growth of the nanowires among the commercially available catalyst nanoparticles (Chapter 2). Then, after the comparison of the catalytic activities of the catalysts, I tried to synthesize the catalyst nanoparticles by myself and used the synthesized nanoparticles to grow the MoS₂ nanowires with high aspect ratio (Chapter 3). The structure, chirality and the growth mechanism of the MoS₂ nanowires were discussed in detail. The size and shape effects of the catalytic nanoparticles on the morphology and composition of the nanowires were planned to be investigated (Chapter 4). To improve the growth density of the nanowires, substrate surface treatments were taken by various methods. To control the aspect ratio of the nanowires, the effects of growth temperature and time were tried to be investigated (Chapter 5).

References:

1. S. Barth, F. Hernandez-Ramirez, J.D. Holmes and A. Romano-Rodriguez, *Prog. Mater. Sci.*, 2010, **55**, 563-627.
2. U.G. Akpan and B.H. Hameed, *J. Hazard. Mater.*, 2009, **170**, 520-529.
3. H. Wang, L. Zhang, Z. Chen, J. Hu, S. Li, Z. Wang, J. Liu and X. Wang, *Chem. Soc. Rev.*, 2014, **43**, 5234-5244.
4. Y. Lin, G. Yuan, R. Liu, S. Zhou, S.W. Sheehan and D. Wang, *Chem. Phys. Lett.*, 2011, **507**, 209-215.
5. K. van Benthem, C. Elsässer and R.H. French, *J. Appl. Phys.*, 2001, **90**, 6156-6164.
6. J. Wyss, D. Bisello and D. Pantano, *Nuclear Instruments and Methods in Physics Research Section A: Accelerators, Spectrometers, Detectors and Associated Equipment*, 2001, **462**, 426-434.
7. A. Tsumura, H. Koezuka and T. Ando, *Appl. Phys. Lett.*, 1986, **49**, 1210-1212.
8. T. Pauporté and D. Lincot, *Electrochim. Acta*, 2000, **45**, 3345-3353.
9. R.D. Vispute, V. Talyansky, S. Choopun, R.P. Sharma, T. Venkatesan, M. He, X. Tang, J.B. Halpern, M.G. Spencer, Y.X. Li, L.G. Salamanca-Riba, A.A. Iliadis and K.A. Jones, *Appl. Phys. Lett.*, 1998, **73**, 348-350.
10. L. Cao, J.S. White, J. Park, J.A. Schuller, B.M. Clemens and M.L. Brongersma, *Nat. Mater.*, 2009, **8**, 643-647.
11. V.V. Pokropivny and V.V. Skorokhod, *Materials Science and Engineering: C*, 2007, **27**, 990-993.
12. S. Kim, R.W. Day, J.F. Cahoon, T.J. Kempa, K. Song, H. Park and C.M. Lieber, *Nano Lett.*, 2012, **12**, 4971-4976.

13. K.S. Leschkies, R. Divakar, J. Basu, E. Enache-Pommer, J.E. Boercker, C.B. Carter, U.R. Kortshagen, D.J. Norris and E.S. Aydil, *Nano Lett.*, 2007, **7**, 1793-1798.
14. L. Hu and G. Chen, *Nano Lett.*, 2007, **7**, 3249-3252.
15. J.H. Chua, R. Chee, A. Agarwal, S.M. Wong and G. Zhang, *Anal. Chem.*, 2009, **81**, 6266-6271.
16. A. Kolmakov, Y. Zhang, G. Cheng and M. Moskovits, *Adv. Mater.*, 2003, **15**, 997-1000.
17. M. Law, J. Goldberger and P. Yang, *Annu. Rev. Mater. Res.*, 2004, **34**, 83-122.
18. P. Xiao, X. Ge, H. Wang, Z. Liu, A. Fisher and X. Wang, *Adv. Funct. Mater.*, 2015, **25**, 1520-1526.
19. X. Sun, C. Li, W. Wong, N. Wong, C. Lee, S. Lee and B. Teo, *J. Am. Chem. Soc.*, 2002, **124**, 14464-14471.
20. Q. Gao, C. Zhang, S. Xie, W. Hua, Y. Zhang, N. Ren, H. Xu and Y. Tang, *Chem. Mater.*, 2009, **21**, 5560-5562.
21. Z. Zhong, F. Qian, D. Wang and C.M. Lieber, *Nano Lett.*, 2003, **3**, 343-346.
22. X. Lu, M. Yu, T. Zhai, G. Wang, S. Xie, T. Liu, C. Liang, Y. Tong and Y. Li, *Nano Lett.*, 2013, **13**, 2628-2633.
23. V. Chakrapani, J. Thangala and M.K. Sunkara, *Int. J. Hydrogen Energ.*, 2009, **34**, 9050-9059.
24. J. Chen, S.Z. Deng, N.S. Xu, S. Wang, X. Wen, S. Yang, C. Yang, J. Wang and W. Ge, *Appl. Phys. Lett.*, 2002, **80**, 3620-3622.
25. W. Hong, J. Wang, Z. Li and S. Yang, *Energy*, 2015, **93**, 435-441.
26. Q. Wang, X. Gang and H. Gaorong, *J. Solid State Chem.*, 2005, **178**, 2680-2685.

27. X. Feng, K. Shankar, O.K. Varghese, M. Paulose, T.J. Latempa and C.A. Grimes, *Nano Lett.*, 2008, **8**, 3781-3786.
28. Z.R. Dai, J.L. Gole, J.D. Stout and Z.L. Wang, *J. Phys. Chem. B*, 2002, **106**, 1274-1279.
29. J. Cui, *Mater. Charact.*, 2012, **64**, 43-52.
30. S. Lijima, *Nature*, 1991, **354**, 56-58.
31. Q. Liu, J. Tian, W. Cui, P. Jiang, N. Cheng, A.M. Asiri and X. Sun, *Angew. Chem. Int. Ed.*, 2014, **53**, 6710-6714.
32. J. Deng, P. Ren, D. Deng, L. Yu, F. Yang and X. Bao, *Energy Environ. Sci.*, 2014, **7**, 1919-1923.
33. D. Deng, L. Yu, X. Chen, G. Wang, L. Jin, X. Pan, J. Deng, G. Sun and X. Bao, *Angew. Chem. Int. Ed.*, 2013, **52**, 371-375.
34. E.T. Thostenson, Z. Ren and T. Chou, *Composites Science and Technology*, 2001, **61**, 1899-1912.
35. B. Vedhanarayanan, V.S. Nair, V.C. Nair and A. Ajayaghosh, *Angew. Chem. Int. Ed.*, 2016, **55**, 10345-10349.
36. N.K. Subbaiyan, S. Cambré, A.N.G. Parra-Vasquez, E.H. Hároz, S.K. Doorn and J.G. Duque, *ACS Nano*, 2014, **8**, 1619-1628.
37. W. Hou, S. BeigzadehMilani, C.T. Jafvert and R.G. Zepp, *Environ. Sci. Technol.*, 2014, **48**, 3875-3882.
38. U. Schubert and N. Husing, *Synthesis of Inorganic Materials*, 2005.
39. T. Ohashi and T. Shima, *Carbon*, 2015, **87**, 453-461.
40. X. Li, X. Tu, S. Zaric, K. Welsher, W.S. Seo, W. Zhao and H. Dai, *J. Am. Chem. Soc.*, 2007, **129**, 15770-15771.

41. W. Chiang and R. Mohan Sankaran, *Nat. Mater.*, 2009, **8**, 882-886.
42. S. Sharma, B.P. Jaisi, K.P. Sharma, M.I. Araby, G. Kalita and M. Tanemura, *Physica Status Solidi (a)*, 2017, 1700566.
43. A. Sengupta, *Applied Physics A*, 2017, **123**.
44. A.Y. Polyakov, L. Yadgarov, R. Popovitz-Biro, V.A. Lebedev, I. Pinkas, R. Rosentsveig, Y. Feldman, A.E. Goldt, E.A. Goodilin and R. Tenne, *J. Phys. Chem. C*, 2014, **118**, 2161-2169.
45. C.M. Zelenski and P.K. Dorhout, *J. Am. Chem. Soc.*, 1998, **120**, 734-742.
46. E.M. Rivera-Muñoz, *J. Appl. Phys.*, 2007, **102**, 94302.
47. M. Remskar, A. Mrzel, Z. Skraba, A. Jesih, M. Ceh, J. Demsär, P. Stadelmann, F. Levy and D. Mihailovic, *Science*, 2001, **292**, 479-481.
48. M. Remskar, A. Mrzel, M. Virsek, M. Godec, M. Krause, A. Kolitsch, A. Singh and A. Seabaugh, *Nanoscale Res. Lett.*, 2011, **6**, 26.
49. H.A. Therese, N. Zink, U. Kolb and W. Tremel, *Solid State Sci.*, 2006, **8**, 1133-1137.
50. V. Lavayen, N. Mirabal, C. O Dwyer, M.A. Santa Ana, E. Benavente, C.M. Sotomayor Torres and G. González, *Appl. Surf. Sci.*, 2007, **253**, 5185-5190.
51. S. Fathipour, M. Remskar, A. Varlec, A. Ajoy, R. Yan, S. Vishwanath, S. Rouvimov, W.S. Hwang, H.G. Xing, D. Jena and A. Seabaugh, *Appl. Phys. Lett.*, 2015, **106**, 22114.
52. A.A. Peyghan, S.A. Aslanzadeh and A. Samiei, *Monatshefte für Chemie - Chemical Monthly*, 2014, **145**, 1083-1087.
53. E. Chigo Anota and G.H. Coccoletzi, *Physica E: Low-dimensional Systems and Nanostructures*, 2014, **56**, 134-140.

54. X. Jiang, Q. Weng, X. Wang, X. Li, J. Zhang, D. Golberg and Y. Bando, *J. Mater. Sci. Technol.*, 2015, **31**, 589-598.
55. Q.H. Wang, K. Kalantar-Zadeh, A. Kis, J.N. Coleman and M.S. Strano, *Nat. Nanotechnol.*, 2012, **7**, 699-712.
56. W. Li, G. Zhang, M. Guo and Y. Zhang, *Nano Res.*, 2014, **7**, 518-527.
57. D. Yin, M. Wu, Y. Yang, W. Cen and H. Fang, *Physica E: Low-dimensional Systems and Nanostructures*, 2016, **83**, 232-237.
58. B.C. Liu, B. Yu and M.X. Zhang, *Chem. Phys. Lett.*, 2005, **407**, 232-235.
59. S. Chai, S.H.S. Zein and A.R. Mohamed, *Solid State Commun.*, 2006, **140**, 248-250.
60. T. Ižák, T. Daniš, M. Veselý, M. Marton and M. Michalka, *Vacuum*, 2007, **82**, 134-137.
61. I.S. Kim, V.K. Sangwan, D. Jariwala, J.D. Wood, S. Park, K. Chen, F. Shi, F. Ruiz-Zepeda, A. Ponce, M. Jose-Yacamán, V.P. Dravid, T.J. Marks, M.C. Hersam and L.J. Lauhon, *ACS Nano*, 2014, **8**, 10551-10558.
62. J. Shi, D. Ma, G. Han, Y. Zhang, Q. Ji, T. Gao, J. Sun, X. Song, C. Li, Y. Zhang, X. Lang, Y. Zhang and Z. Liu, *ACS Nano*, 2014, **8**, 10196-10204.
63. G.C. Yi, *Semiconductor Nanostructures for Optoelectronic Devices*, 2012.
64. A. Gomez-Martinez, F. Márquez and C. Morant, *J. Sol-Gel Sci. Techn.*, 2017, **81**, 321-326.
65. S. Chen, P. Ying, L. Wang, F. Gao, G. Wei, J. Zheng, Z. Xie and W. Yang, *RSC Adv.*, 2014, **4**, 8376-8382.
66. K. Lin, P. Yao, J. Zhao, S. Guo and F. Tian, *Mater. Lett.*, 2017, **203**, 21-23.

67. A. Jaud, L. Auvray, A. Kahouli, T. Abi-Tannous, F. Cauwet, G. Ferro and C. Brylinski, *Physica Status Solidi (a)*, 2017, **214**, 1600428.
68. R.S. Wagner, W.C. Ellis, K.A. Jackson and S.M. Arnold, *J. Appl. Phys.*, 1964, **35**, 2993-3000.
69. J.L. Lensch-Falk, E.R. Hemesath, D.E. Perea and L.J. Lauhon, *J. Mater. Chem.*, 2009, **19**, 849.
70. C.Y. Wen, M.C. Reuter, J. Tersoff, E.A. Stach and F.M. Ross, *Nano Lett.*, 2010, **10**, 514-519.
71. K. Lee, S. Lee, R.R. Vanfleet and W. Sigmund, *Chem. Phys. Lett.*, 2003, **376**, 498-503.
72. A. Umar, Y.H. Im and Y.B. Hahn, *J. Electron. Mater.*, 2006, **35**, 758-765.

Chapter 2. Catalysts for the growth of MoS₂ nanowires

2.1 Introduction

As I mentioned in the general introduction, MoS₂ has gained widespread attention due to its potential for a wide application in electronics, energy and catalysis field [1-10]. Numerous researches have been focused on its monolayer [11-23], while little attention was paid on its 1D nanostructures [24-29]. Here, I will provide a new approach to synthesize MoS₂ nanowires by catalytic CVD.

Catalytic CVD is a promising method to synthesize 1D MoS₂ nanostructures, which has been reported to produce carbon nanotubes by using a catalyst with high melting points [30-37]. In the previous work in our laboratory [38], MoS₂ nanowires have been observed when we fabricated MoS₂ thin films with contaminated SiO₂/Si substrates (Figure 2-1). It was found that the growth of nanowires could be induced by metal oxide particles remained on the contaminated substrates. The existence of the particles containing Fe can promote the growth of nanowires.

It is of great interest to investigate the effective catalyst for the fabrication of MoS₂ nanowires. From the results of the EDS elemental analysis at five different points of the nanowire, no other elements were found except O, S, Fe, Ta, and Mo (Ta element was found in all the regions due to the signal from the TEM grid), indicating that the particles containing Fe belong to iron oxides or iron. The common iron oxides group is consist of wüstite (FeO), hematite (α -Fe₂O₃), maghemite (γ -Fe₂O₃), magnetite (Fe₃O₄) and so on.

In this Chapter, I will search the effective catalyst for the growth of MoS₂ nanowires in the iron and iron oxides group, and study the catalytic activities of oxides of Fe, Mn, Ni and Cu for the growth of MoS₂ nanowires [39].

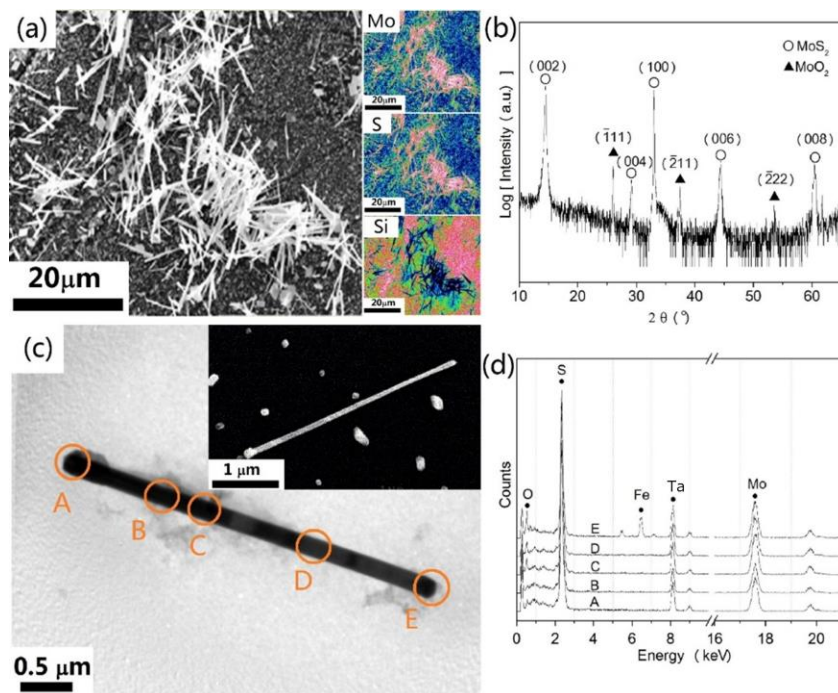


Figure 2-1. (a) SEM and EDS mapping images of nanowires, and its (b) XRD patterns. (c) TEM and FESEM images of a nanowire, and (d) EDS elemental analysis at five different points. [38]

2.2 Experimental section

2.2.1 Synthesis

The CVD apparatus [39-42] to synthesize the MoS₂ nanowires is shown in Figure 2-2. The information of the materials and substrates are as follows.

Source materials: 0.15g MoO₃, bought from Kanto Chemicals; 1.5g sulfur, bought from Kanto Chemicals.

Carrier gas: Ar (purity 99.9995%), Hokkaido Air and Water Company.

Substrates: Si wafers with 285 nm SiO₂ layers, purchased from Graphene supermarket. It was cleaned by RCA method [43] before use.

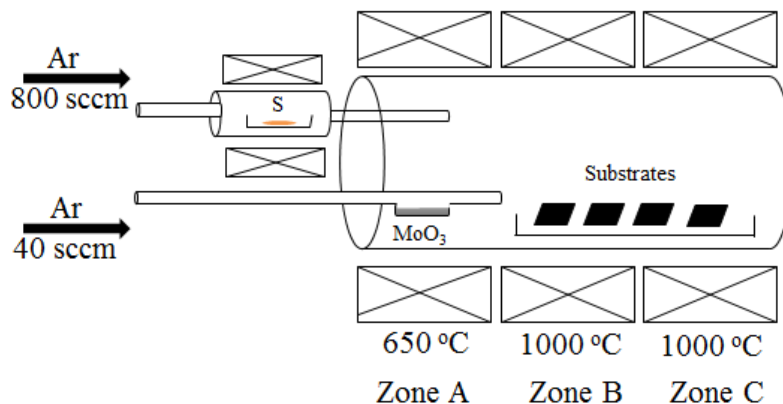


Figure 2-2. Schematic image of the CVD growth chamber. Sulfur was placed in a separated furnace. MoO₃ was located at the up-stream of the furnace, named Zone A. Substrates were placed in the down-stream area of the furnace, named Zone B and Zone C.

MoO₃ and sulfur were carried in separated carrier gas flows: the flow rate of MoO₃ was 40 sccm and the rate of sulfur was 800 sccm. The substrates were spin-coated with the catalyst candidates, which will be described in details in the results part. Temperatures of sulfur furnace, Zone A and Zone B and C were 280 °C, 650 °C and 1000 °C, respectively. The pressure of the apparatus during the growth was kept at 1 atm and the growth time of the nanowires was 1 h.

2.2.2 Characterization

Scanning electron microscope [SEM, JSV-6510LA (JEOL)] and a field-emission SEM [FESEM, JSM-6500F (JEOL)] were employed to characterize the morphologies of the nanoparticles and the CVD products.

Transmission electron microscope [TEM, 200 kV, JEM-2010(JEOL)] was used to characterize the structure of the nanowires. Before the TEM characterization, Micro pickup system (Axis Pro, Microsupport Inc.) was used to pick up nanowires grown on the substrates.

Raman microscope (Ranishaw Invia) with 532nm excitation was used to identify the composition of the nanowires.

2.3 Results and discussion

2.3.1 Search for the catalysts

In attempting to reveal the actual catalyst for the MoS₂ nanowires growth, I intentionally dispersed Fe, FeO and Fe₂O₃ particles on the RCA-cleaned SiO₂/Si substrate surface: for the experiment of Fe, 10-nm thickness of Fe was coated on the substrate surface by sputtering method; in the other cases, the particles of FeO and Fe₂O₃ were spin coated on the substrates by an ethanol suspension method, respectively. FeO and Fe₂O₃ were bought from Sigma-Aldrich and grinded into smaller particles before being dispersed into ethanol.

Figure 2-3 (a) ~ (d) display the SEM images after dispersing (a) (b) FeO and (c) (d) Fe₂O₃ particles on the substrates. The morphology, size and number density of particles

can be observed in Figure 2-3. We can see that the size dispersion and the shape of the both particles are not uniform. Most of the particles tended to be aggregated into larger species evidently [Figure 2-3 (a) and(c)] but some smaller nanoparticles (about 100 nm) were still existed [Figure 2-3 (b) and (d)].

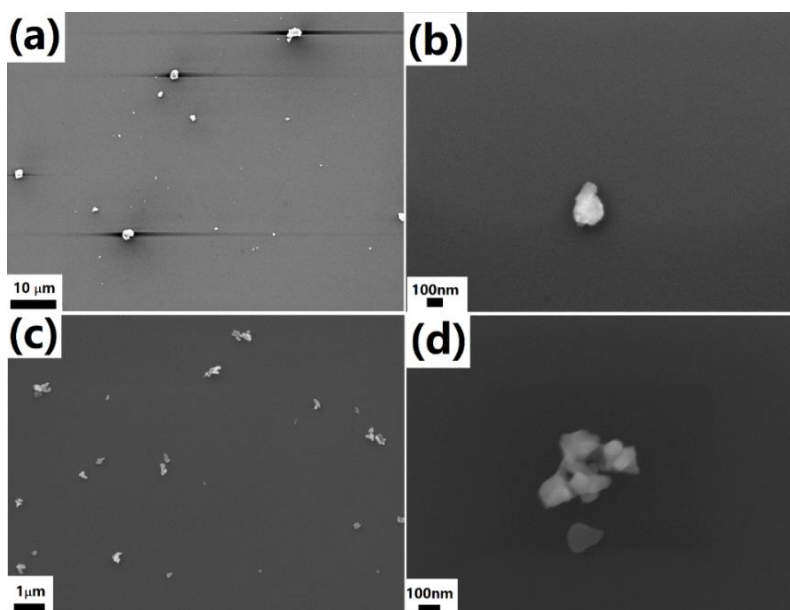


Figure 2-3. SEM images of substrate surfaces after dispersed (a) (b) FeO and (c) (d) Fe₂O₃ particles.

The CVD results are shown in Figure 2-4 (a) ~ (c). It can be seen that thin standing leaf- like structure and lumps were grown on the substrates in the case of Fe and Fe₂O₃ [Figure 2-4 (a), (c)], indicating that Fe or Fe₂O₃ could not promote the growth of 1D MoS₂ nanostructures. In the case of FeO, randomly dispersed nanowires could be found grown on the edge side of the substrate [Figure 2-4 (b)]. TEM and Raman were taken to characterize the composition of these nanowires, as shown in Figure 2-5.

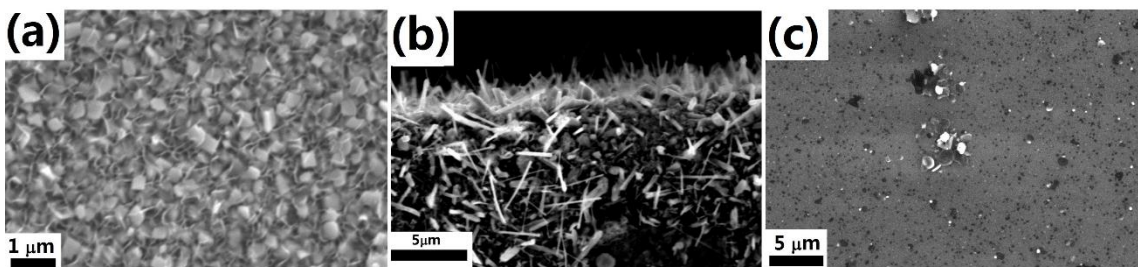


Figure 2-4. SEM images after CVD with (a) Fe, (b) FeO and (c) Fe₂O₃.

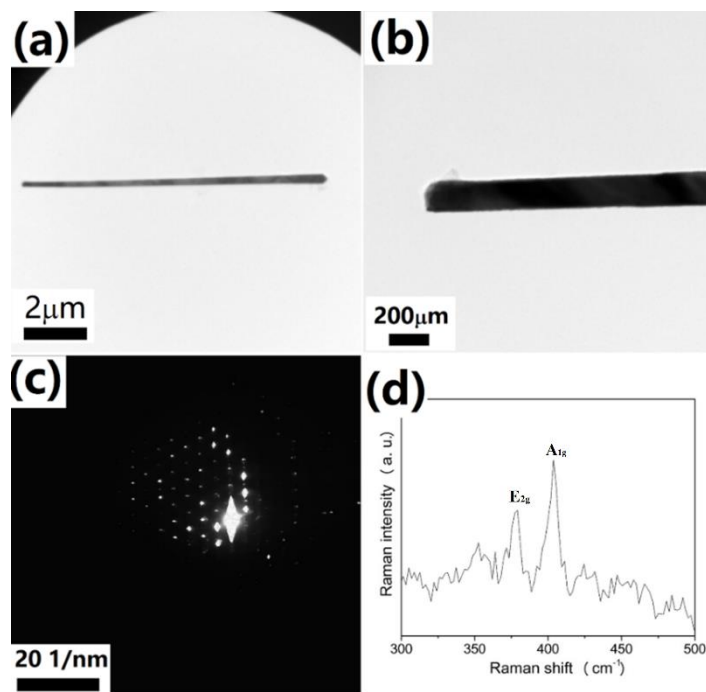


Figure 2-5. TEM images of (a) a whole nanowire and (b) an end of the nanowire. (c) SAED of the nanowire in Figure 2-5(b). (d) Raman spectra of the nanowire.

Figure 2-5 (a) shows that the length of the nanowire is about 9.6 μm , and the diameter of the nanowire is increasing from 160 nm to 260 nm. The selected area electron diffraction (SAED) of one end of the nanowire [Figure 2-5(b)] was measured, as shown in Figure 2-5(c). We can see that the spots in the diffraction image are identified as hexagonal lattice. The constant of the lattice is 0.32 nm, which is in accordance with the lattice parameter of a MoS₂. The Raman peaks at 379 and 404 cm^{-1} could be observed in the Raman microscope

scan of the picked-up nanowire [Figure 2-5(d)]. These correspond to E¹_{2g} and A_{1g} vibrational modes of the MoS₂ [41] respectively, which further confirmed the composition of the nanowire is MoS₂.

From the above results, I could draw a conclusion that the effective catalyst for the growth of MoS₂ nanowires in iron and iron oxide group is FeO. As I mentioned in the introduction part, both Fe₂O₃ and FeO are the members of the common iron oxides. Their different catalytic behaviors performed in the growth of MoS₂ nanowires are suggested to be attributed to the different oxidation states. FeO is an iron oxide which only contain divalent Fe. The structure of FeO is similar to NaCl and it is usually non-stoichiometric with O-vacancy [44]. Due to its defective structure, it is unstable and easier to react with other chemical species.

2.3.2 Catalytic activities of other metal oxides

A comparative study to select suitable catalysts is essential for the growth of MoS₂ nanowires. In order to use the same conditions, I chose commercially available metal oxide particles, such as MnO, CuO, NiO and Cu₂O.

All of them were bought from Sigma-Aldrich. The ethanol suspensions of nanoparticles of MnO, CuO, NiO and Cu₂O were spin-coated on the cleaned substrates before CVD process. The diameters of them are 50-200 nm. Figure 2-6 (a) and (b) show the dispersion of NiO and Cu₂O particles.

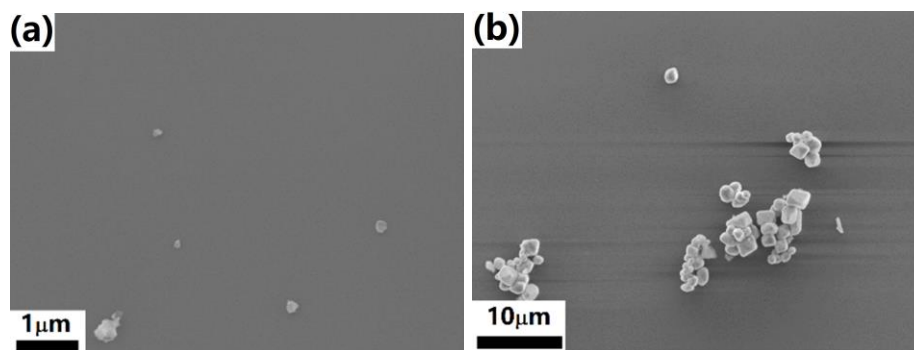


Figure 2-6. SEM images of substrate surfaces after dispersion of (a) NiO and (b) Cu₂O.

CVD experiments were conducted after spin-casting the catalysts on the substrates. The SEM images of the products are shown in Figure 2-7 (a) ~ (d). It is obvious that MnO and CuO could not act as the catalysts for the growth of MoS₂ nanowires, instead, particles and leafs were fabricated on the surface of the substrates [Figure 2-7 (a) and (b)]. In the cases of NiO and Cu₂O, MoS₂ microcrystals and needles (thick nanowires) were grown, as shown in Figures 2-7(c) and (d).

TEM were taken after picking up one nanowire from the substrates, as given in Figure 2-8. Figure 2-8 (a) shows the whole nanowire fabricated by using NiO nanoparticles, and Figure 2-8 (b) and (c) are the magnification image of part of the nanowire and its diffraction image, respectively. The nanowire shown in Figure 2-8 (a) has a length of 3.5 μm and a diameter of 300 nm. It is so thick that the electron beam of TEM could not go throughout the nanowire, as a result of showing dark region of the whole nanowire in the image. The composition of the nanowire was determined to be MoS₂, as the spots observed in Figure 2-6 (c) are in hexagonal lattice and the lattice constant is the same with MoS₂.

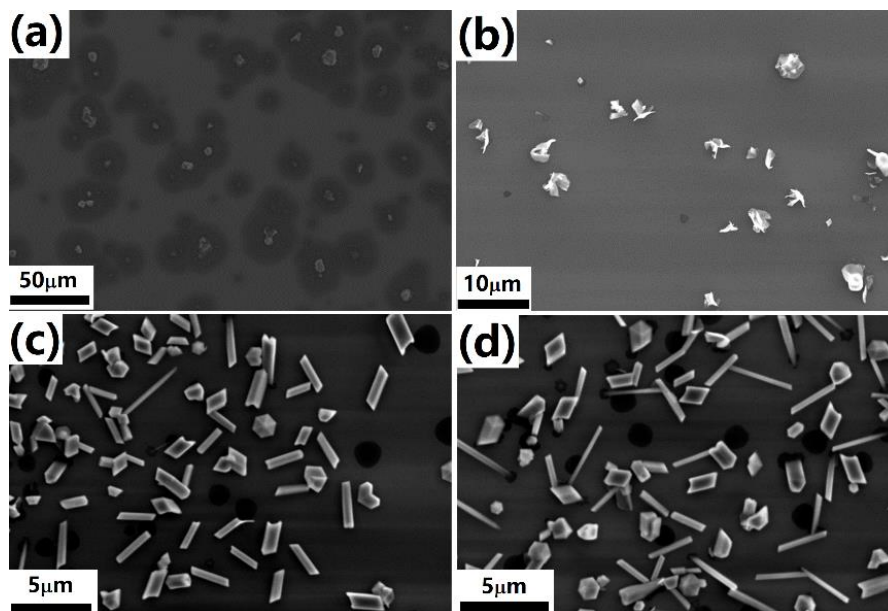


Figure 2-7. SEM images after CVD with (a) MnO, (b) CuO, (c) NiO and (d) Cu₂O catalyst particles.

The nanowires grown by Cu₂O particles were also characterized by TEM. Figure 2-8 (d) ~ (f) are the corresponding results. The diameter of the nanowire was 450 nm and the length was 4 μm. Also, the composition of the nanowire was confirmed to be MoS₂ by the analysis of its diffraction image in Figure 2-8 (f). It seems that the results of using NiO and Cu₂O are similar.

Raman and XRD were also taken to characterize the products, as shown in Figure 2-9. Raman peaks at 380-381 and 405-407 cm⁻¹ in the Raman spectra are corresponding to E_{12g}¹ and A_{1g} vibrational modes of the MoS₂, respectively [41]. The XRD spectra was obtained to examine the crystal structure of these nanowires [Figure 2-9 (b)]. From the SEM image (Figure 2-7), we can find that the substrates are not only covered with MoS₂ nanowires, but most regions are filled with impurities, such as microcrystals and particles. Some peaks are well indexed to MoS₂, whereas other peaks belong to MoO₂. In the XRD

patterns of MoS₂, (002), (004), (006) and (008) are characteristic of the basal plane of the MoS₂ layers, while the distinct peak (100)_{MoS₂} is suggesting a characteristic crystal orientation of the nanowires.

It should be noted that the concentration of all the catalysts is the same and the solvent of all the particle suspensions is ethanol. Compared the results of FeO, NiO and Cu₂O [Figure 2-4(b), 2-7(c) and 2-7(d)], it can be seen that the density of the nanowires is high when using catalyst FeO, while it is low when using NiO and Cu₂O. This indicates that FeO is more active than NiO and Cu₂O in the growth of MoS₂ nanowires.

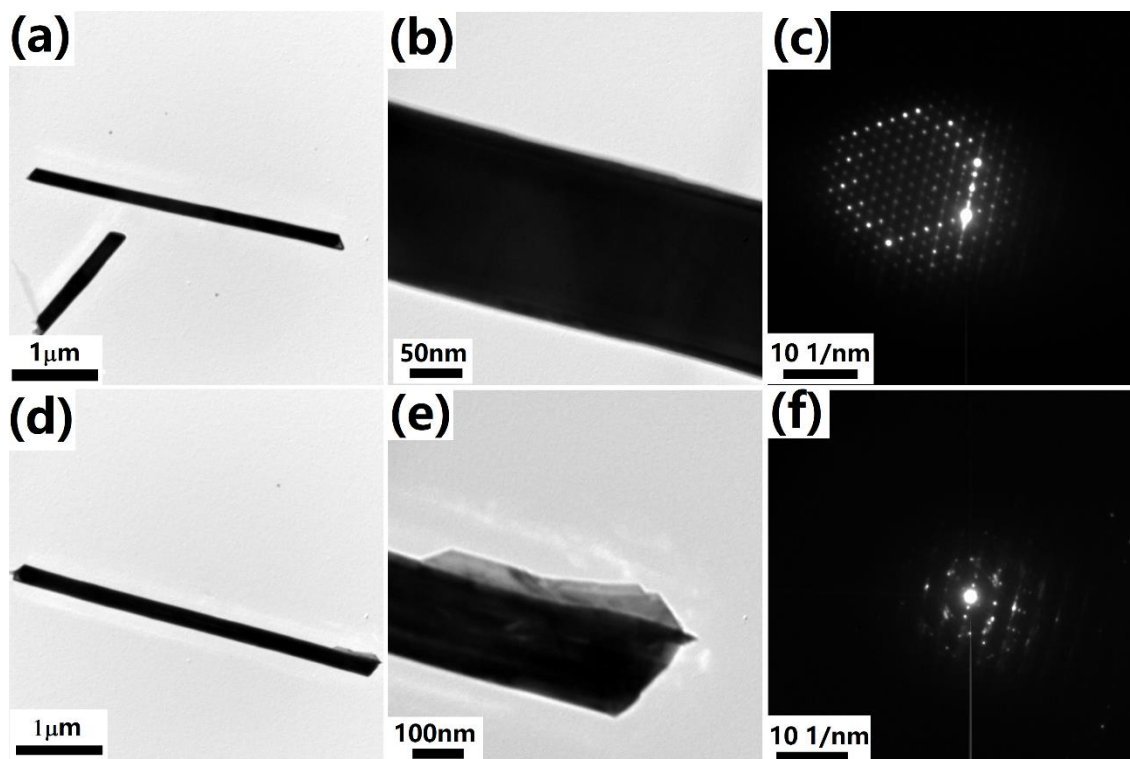


Figure 2-8. (a) (b) TEM images and (c) SAED of the nanowire grown by NiO. (d) (e) TEM images and (f) SAED of the nanowire grown by Cu₂O.

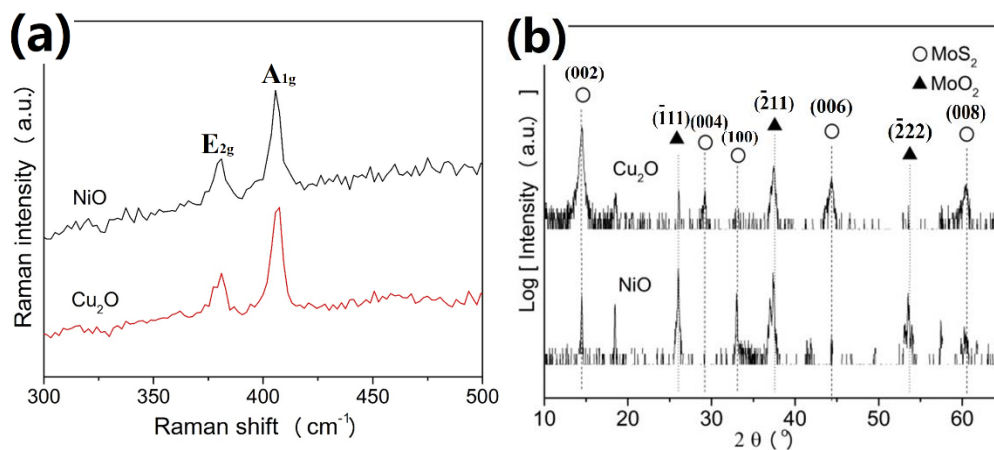


Figure 2-9. (a) Raman spectra and (b) XRD patterns of the nanowires grown by Cu₂O and NiO particles.

It is interesting to investigate the reasons for the excellent catalytic activity found in only FeO particles. I examined the stable compounds of M-Mo-S system (M: Fe, Cu and Ni). Through the search in the inorganic crystal structure database (ICSD Fiz Karlsruhe, version 2017-1) [45], we found that the layered structures existed in the compounds of M-Mo-S system are only found in the compounds of Fe-Mo-S system, as shown in Figure 2-10. It is supposed that the formation of layered Fe_xMoS₂ seeds during the synthesis can facilitate the growth of MoS₂ nanowires.

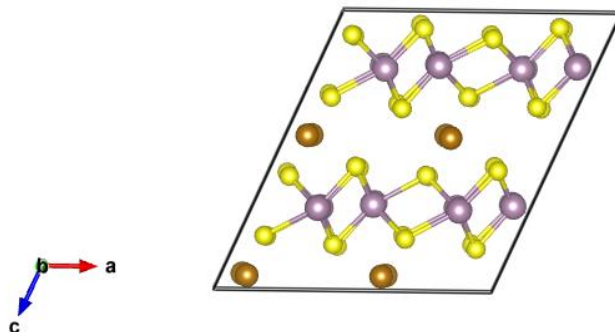


Figure 2-10. Layered structure in the compounds of Fe-Mo-S system.

2.4 Conclusions

In this Chapter, I have found that only FeO can be the catalyst for the growth of MoS₂ nanowires in the iron and iron oxides group. SEM, TEM and Raman were employed to characterize the composition and the structure of the MoS₂ nanowires. The length of the nanowires could be up to 9.6 μm but the diameter was greater than 150 nm. The catalytic activities of other transitional metal oxides nanoparticles (MnO, CuO, NiO and Cu₂O) were also searched. It is found that NiO and Cu₂O can promote the growth of 1D MoS₂ nanostructures but MnO, CuO cannot. Comparing the CVD results of using FeO, NiO and Cu₂O catalytic particles, FeO has the best catalytic activity in the growth of MoS₂ nanowires.

References:

1. H. Hwang, H. Kim and J. Cho, *Nano Lett.*, 2011, **11**, 4826-4830.
2. C. Zhang, Z. Wang, Z. Guo and X.W.D. Lou, *ACS Appl. Mater. Inter.*, 2012, **4**, 3765-3768.
3. G. Eda and S.A. Maier, *ACS Nano*, 2013, **7**, 5660-5665.
4. M.S. Choi, D. Qu, D. Lee, X. Liu, K. Watanabe, T. Taniguchi and W.J. Yoo, *ACS Nano*, 2014, **8**, 9332-9340.
5. D. Kong, H. Wang, J.J. Cha, M. Pasta, K.J. Koski, J. Yao and Y. Cui, *Nano Lett.*, 2013, **13**, 1341-1347.
6. Y. Yu, S. Huang, Y. Li, S.N. Steinmann, W. Yang and L. Cao, *Nano Lett.*, 2014, **14**, 553-558.
7. D. Gopalakrishnan, D. Damien and M.M. Shaijumon, *ACS Nano*, 2014, **8**, 5297-5303.

8. J. Shi, D. Ma, G. Han, Y. Zhang, Q. Ji, T. Gao, J. Sun, X. Song, C. Li, Y. Zhang, X. Lang, Y. Zhang and Z. Liu, *ACS Nano*, 2014, **8**, 10196-10204.
9. O.Y. Gutiérrez, S. Singh, E. Schachtl, J. Kim, E. Kondratieva, J. Hein and J.A. Lercher, *ACS Catal.*, 2014, **4**, 1487-1499.
10. Y. Zhang, Q. Ji, G. Han, J. Ju, J. Shi, D. Ma, J. Sun, Y. Zhang, M. Li, X. Lang, Y. Zhang and Z. Liu, *ACS Nano*, 2014, **8**, 8617-8624.
11. Y. Lin, N. Lu, N. Perea-Lopez, J. Li, Z. Lin, X. Peng, C.H. Lee, C. Sun, L. Calderin, P.N. Browning, M.S. Bresnehan, M.J. Kim, T.S. Mayer, M. Terrones and J.A. Robinson, *ACS Nano*, 2014, **8**, 3715-3723.
12. J. Shi, D. Ma, G. Han, Y. Zhang, Q. Ji, T. Gao, J. Sun, X. Song, C. Li, Y. Zhang, X. Lang, Y. Zhang and Z. Liu, *ACS Nano*, 2014, **8**, 10196-10204.
13. I.S. Kim, V.K. Sangwan, D. Jariwala, J.D. Wood, S. Park, K. Chen, F. Shi, F. Ruiz-Zepeda, A. Ponce, M. Jose-Yacamán, V.P. Dravid, T.J. Marks, M.C. Hersam and L.J. Lauhon, *ACS Nano*, 2014, **8**, 10551-10558.
14. M. Kan, J.Y. Wang, X.W. Li, S.H. Zhang, Y.W. Li, Y. Kawazoe, Q. Sun and P. Jena, *J. Phys. Chem. C*, 2014, **118**, 1515-1522.
15. S. Wu, C. Huang, G. Aivazian, J.S. Ross, D.H. Cobden and X. Xu, *ACS Nano*, 2013, **7**, 2768-2772.
16. K. Liu, W. Zhang, Y. Lee, Y. Lin, M. Chang, C. Su, C. Chang, H. Li, Y. Shi, H. Zhang, C. Lai and L. Li, *Nano Lett.*, 2012, **12**, 1538-1544.
17. X. Wang, H. Feng, Y. Wu and L. Jiao, *J. Am. Chem. Soc.*, 2013, **135**, 5304-5307.
18. D. Kong, H. Wang, J.J. Cha, M. Pasta, K.J. Koski, J. Yao and Y. Cui, *Nano Lett.*, 2013, **13**, 1341-1347.

19. Y. Kang, S. Najmaei, Z. Liu, Y. Bao, Y. Wang, X. Zhu, N.J. Halas, P. Nordlander, P.M. Ajayan, J. Lou and Z. Fang, *Adv. Mater.*, 2014, **26**, 6467-6471.
20. Y. Lee, X. Zhang, W. Zhang, M. Chang, C. Lin, K. Chang, Y. Yu, J.T. Wang, C. Chang, L. Li and T. Lin, *Adv. Mater.*, 2012, **24**, 2320-2325.
21. K.M. McCreary, A.T. Hanbicki, J.T. Robinson, E. Cobas, J.C. Culbertson, A.L. Friedman, G.G. Jernigan and B.T. Jonker, *Adv. Funct. Mater.*, 2014, **24**, 6449-6454.
22. Y. Yu, C. Li, Y. Liu, L. Su, Y. Zhang and L. Cao, *Sci Rep-Uk*, 2013, **3**.
23. W. Zhang, J. Huang, C. Chen, Y. Chang, Y. Cheng and L. Li, *Adv. Mater.*, 2013, **25**, 3456-3461.
24. M. Remskar, A. Mrzel, Z. Skraba, A. Jesih, M. Ceh, J. Demsjör, P. Stadelmann, F. Levy and D. Mihailovic, *Science*, 2001, **292**, 479-481.
25. S. Fathipour, M. Remskar, A. Varlec, A. Ajoy, R. Yan, S. Vishwanath, S. Rouvimov, W.S. Hwang, H.G. Xing, D. Jena and A. Seabaugh, *Appl. Phys. Lett.*, 2015, **106**, 22114.
26. M. Remskar, A. Mrzel, M. Virsek, M. Godec, M. Krause, A. Kolitsch, A. Singh and A. Seabaugh, *Nanoscale Res. Lett.*, 2011, **6**, 26.
27. V. Lavayen, N. Mirabal, C. O Dwyer, M.A. Santa Ana, E. Benavente, C.M. Sotomayor Torres and G. González, *Appl. Surf. Sci.*, 2007, **253**, 5185-5190.
28. E.M. Rivera-Muñoz, *J. Appl. Phys.*, 2007, **102**, 94302.
29. H.A. Therese, N. Zink, U. Kolb and W. Tremel, *Solid State Sci.*, 2006, **8**, 1133-1137.
30. G. Zheng, K. Kouda, H. Sano, Y. Uchiyama, Y. Shi and H. Quan, *Carbon*, 2004, **42**, 635-640.
31. L.F. Su, J.N. Wang, F. Yu and Z.M. Sheng, *Chem. Vapor Depos.*, 2005, **11**, 351-354.
32. E. Flahaut, C. Laurent and A. Peigney, *Carbon*, 2005, **43**, 375-383.

33. G. Ortega-Cervantez, G. Rueda-Morales and J. Ortiz-López, *Microelectron. J.*, 2005, **36**, 495-498.
34. B.C. Liu, B. Yu and M.X. Zhang, *Chem. Phys. Lett.*, 2005, **407**, 232-235.
35. S. Chai, S.H.S. Zein and A.R. Mohamed, *Solid State Commun.*, 2006, **140**, 248-250.
36. M. Kohno, T. Orii, M. Hirasawa, T. Seto, Y. Murakami, S. Chiashi, Y. Miyauchi and S. Maruyama, *Applied Physics A*, 2004, **79**, 787-790.
37. T. Ižák, T. Daniš, M. Veselý, M. Marton and M. Michalka, *Vacuum*, 2007, **82**, 134-137.
38. Y. Hashimoto, *Master Thesis*, Hokkaido Univ., 2014.
39. M. Weng, M. Zhang, T. Yanase, F. Uehara, T. Nagahama and T. Shimada, *Jpn. J. Appl. Phys.*, in press.
40. M. Weng, T. Yanase, F. Uehara, S. Watanabe, T. Miura, T. Nagahama and T. Shimada, *CrystEngComm*, 2017, **19**, 3915-3920.
41. T. Yanase, S. Watanabe, M. Weng, T. Nagahama, and T. Shimada, *J. Nanosci. Nanotechnol.*, 2016, **16**, 3223-3227.
42. T. Yanase, S. Watanabe, M. Weng, M. Wakeshima, Y. Hinatsu, T. Nagahama and T. Shimada, *Crys. Growth & Des.*, 2016, **16**, 4467-4472.
43. W. Kern, *J. Electrochem. Soc.*, 1990, **137**, 1887-1892.
44. R. M. Cornell and U. Schwertmann, *The iron oxides: structure, properties, reactions, occurrence, and uses*. VCH, Weinheim; New York, 1996.
45. G. Bergerhoff and I.D. Brown, in "Crystallographic Databases", F.H. Allen et al. (ed.) Chester, International Union of Crystallography, 1987.

Chapter 3. Synthesis of MoS₂ nanowires by chemically synthesized FeO nanoparticles

3.1 Introduction

In Chapter 2, I have found that some of the commercial transition metal oxides (FeO, NiO and Cu₂O) particles can promote the growth of MoS₂ nanowires by using CVD method. The nanowires fabricated with the FeO nanoparticles exhibited the high growth density and the aspect ratio of the nanowires was the highest among the synthesized nanowires. However, the length of the synthesized nanowires was about 9.6 μm and the diameter was larger than 150 nm, which was still in a low aspect ratio. The length and the diameter of the nanowires are critical factors for the properties. The physical properties, such as electron and photon absorption, are closely linked to the size of the nanowires [1-8]. Thus, the aspect ratio of the nanowires must be improved.

Catalyst is one of the most important factors in the nanowire growth by catalytic CVD. As I mentioned in the general introduction, slight changes in size, shape or composition of the catalysts used in the CVD synthesis process, will have an influence on nucleation and growth of the products, leading to the formation of different structures [9-14]. Hence, it is crucial to choose a suitable catalyst in the catalytic growth of MoS₂ nanowires.

FeO has been found to be the most effective catalyst among the transition metal oxides nanoparticles used in Chapter 2, when the concentration of the nanoparticle

solutions was the same and the sizes of the particles were in a similar scale. Furthermore, except the catalytic activity, the size of the catalyst nanoparticles is another factor needed to be considered. The diameter of octahedral FeO nanoparticles can be controlled as small as 32 nm as reported in literature [15-28]. Therefore, FeO is the best choice to be used as the catalyst for the growth of MoS₂ nanowires.

In this Chapter, I will synthesize FeO nanoparticles and use it as the catalyst for the growth of MoS₂ nanowires by CVD method [29]. The structure, the chirality and the growth mechanism of the nanowires are also discussed in details [30].

3.2 Experimental section

3.2.1 Synthesis

Catalyst - FeO nanoparticles

30 nm six-horned FeO nanoparticles were synthesized by thermal decomposition of iron (III) acetylacetonate [Fe(acac)₃] (purity 99.9%, Sigma-Aldrich) [25]. 0.7g Fe(acac)₃ was mixed with 5.5 ml oleic acid (OA) and 5 ml oleylamine (OAm) to form a scarlet suspension liquid. The suspension was heated at 120 °C for 2h to form a dark solution. During the heat process, the solution was pumped to remove the air and water. Then, it was heated to 220 °C and kept for 30 min. After that, the solution was heated to 300 °C at a rate of 2 °C/min and it was kept for 30 min at 300 °C. The flow chart of the 30 nm six-horned octahedra FeO particles synthesis is shown in Figure 3-1.

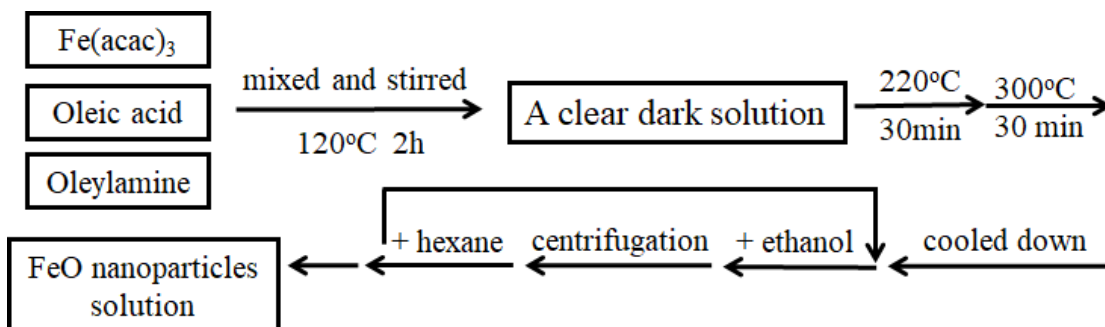


Figure 3-1. Flow chart of the 30 nm six-horned octahedra FeO particles synthesis.

MoS₂ nanowires

MoS₂ nanowires were fabricated by using the same CVD apparatus as shown in Figure 2-2. The source materials and the experimental conditions were the same as the CVD experiments described in Chapter 2. Here, I will explain the process of the CVD method briefly. Prior to the CVD process, the RCA-cleaned substrates were drop-coated by the 30 nm six-horned octahedra FeO particle solution. The source materials were 0.15g MoO₃ and 1.5g sulfur powders, respectively. The conditions of the CVD methods were as follows: 280 °C for sulfur sources, 650 °C for MoO₃ sources (Zone A) and 1000 °C for reaction zones (Zone B and Zone C). The growth time was 1 hour and the pressure was 1 atmosphere. After the reaction, the furnace was cooled down to room temperature (RT) naturally to take the substrates out.

3.2.2 Characterization

TEM equipped with EDS was utilized to characterize the composition and the structure of the FeO catalyst nanoparticles and MoS₂ nanowires.

XRD was used to measure the crystal structure of the FeO nanoparticles.

SEM and FESEM were employed to characterize the morphology of the MoS₂ nanowires.

Raman spectroscopy with 532 nm excitation was utilized to identify the composition of MoS₂ nanowires.

3.3 Results and discussion

3.3.1 FeO nanoparticles

The FeO nanoparticles with mono-dispersion were successfully synthesized by the decomposition of Fe(acac)₃ mixed with OA and OAm at high temperature under Ar atmosphere. Figure 3-2(a) shows the typical TEM image of the FeO catalyst nanoparticles and Figure 3-2(b) is the high magnification image. The six-horned octahedral shape of the nanoparticles can be easily seen in the figure. The size of the particles is 30 nm, the average length of one side to another side. Also, the shape and the size of the particles could be controlled by changing the heat conditions and the ratio of the OA/OAm [25]. The detailed information will be given in Chapter 4.

FeO nanoparticles are not stable as I mentioned in Chapter 2. It is prone to be oxidized if leak happened to the equipment during the synthesis process or it is exposed to air for a long time. Thus the valence state of Fe is needed to be characterized. I used XRD

to characterize the redox state of Fe. The XRD pattern (Figure 3-3) shows the characteristic peaks (111), (200), (220), (311) and (222) of FeO fcc structure, indicating that the synthesized nanoparticles were composed of FeO. In addition, it is clear from the figure that there is a small shoulder located at 34.5°, as a result of a surface oxidation of the particles and the formation of a Fe₃O₄ coating layer.

As the CVD heat condition is as high as 1000 °C, it is interesting to investigate the morphology of the nanoparticles at such a high temperature. FESEM was taken after heating the nanoparticles dropped on SiO₂/Si substrates at 1000 °C, as shown in Figure 3-4. It can be seen that the morphology of the six-horned particles has been turned into frustum shape. Even through the change of morphology has occurred, the catalysts still have sharp edges and acute angles, which will promote the growth of the nanowires. Detailed information will be discussed in the growth mechanism part.

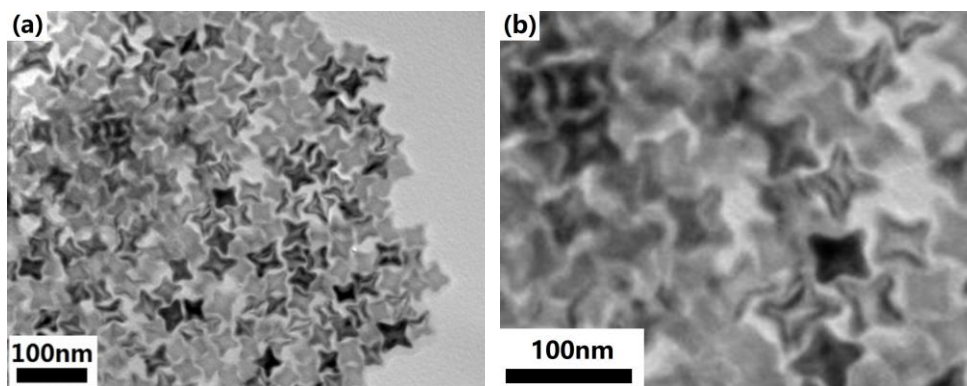


Figure 3-2. (a) TEM image and (b) the high magnification TEM image of 30 nm six-horned FeO nanoparticles.

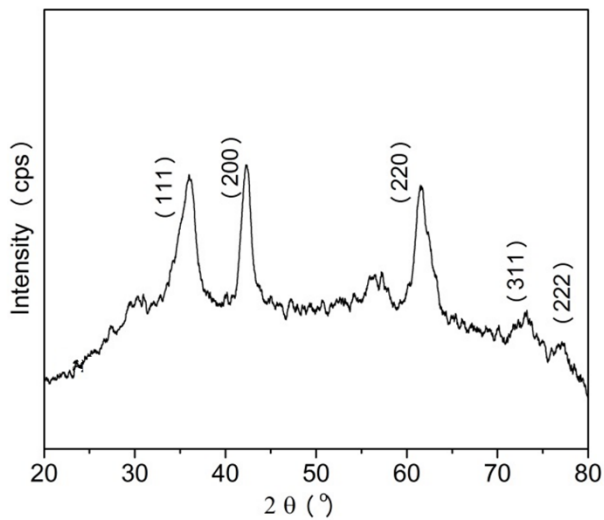


Figure 3-3. XRD pattern of the 30 nm six-horned FeO nanoparticles.

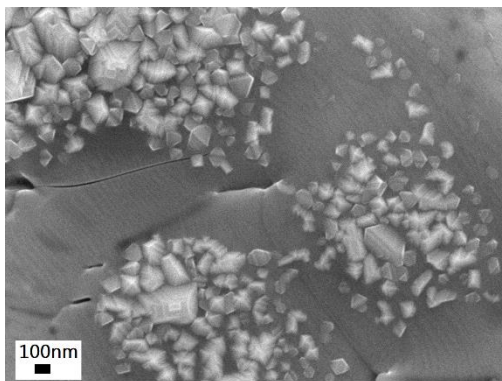


Figure 3-4. FESEM image of the 30 nm six-horned FeO nanoparticles heated at 1000 °C.

3.3.2 MoS₂ nanowires

Morphology of the MoS₂ nanowires

With the synthesized 30 nm six-horned FeO particles, I fabricated the MoS₂ nanowires on RCA-cleaned SiO₂/Si substrates by CVD with flowing MoO₃ and sulfur in separated carrier gas flows. The results are shown in Figure 3-5. From the figure, randomly oriented nanowires could be observed on the substrates. The length of these nanowires was up to 10 μm, and the diameter of them was ranging from 40 to 80 nm. Compared with the one synthesized by commercial FeO particles [Figure 2-4 (b)], the aspect ratio of the nanowires has been significantly improved and the diameter in distribution of them has become more uniform. In addition, most of the nanowires have their ends closed, which will be discussed in the structure part.

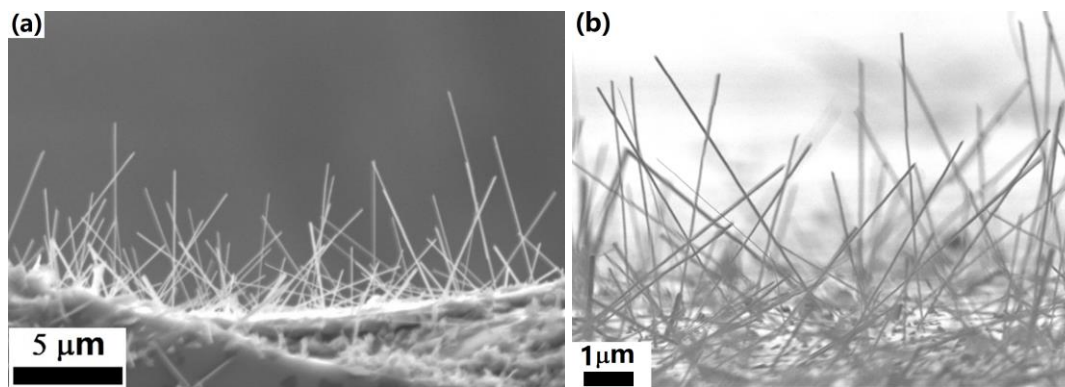


Figure 3-5. (a) SEM image and (b) high magnification TEM image of MoS₂ nanowires synthesized by CVD.

It should be noted that the substrate surfaces after CVD were not only covered by the nanowires, but many regions were filled with impurities, such as particles, thin films and lumps. Thus it is important to pick up one nanowire and moved on other substrate to take

the characterization. Raman was taken first to characterize the composition of the nanowire, as shown in Figure 3-6. The Raman peaks located at 380 and 407 cm⁻¹ are corresponding to E_{2g}¹ and A_{1g} vibrational modes of the MoS₂ respectively [31], indicating that the nanowires I synthesized by the 30 nm six-horned FeO particles are composed of MoS₂.

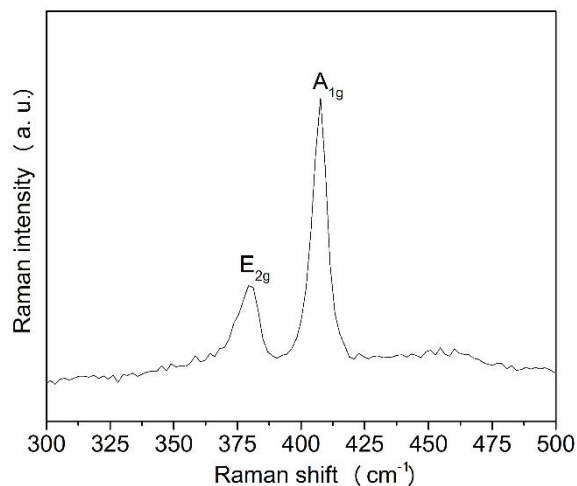


Figure 3-6. Raman spectra of a nanowire.

Structure of the MoS₂ nanowires

The structure of the nanowire was characterized by TEM equipped with EDS, as shown in Figure 3-7(a) ~ (c). From Figure 3-7 (a), we can observe a nanowire showing multilayered tubular structure. The inner diameter of the nanowire was 34 nm and the outer diameter of it was 61 nm. S peak and Mo peak could be obviously detected in the EDS result [Figure 3-7(c)], indicating the composition of the nanowire is MoS_x, which further proves that the nanowire is composed of MoS₂. The SAED pattern of the central part of the Figure 3-7 (a) is given in Figure 3-7 (b). The spots are identified as hexagonal lattice

with the lattice constant of 0.32 nm, in accordance with the lattice parameter of a MoS₂. Some additional weak spots could be observed in the SAED pattern. I consider that the stacking fault in the multilayers is the reason for these spots corresponding to 2×2 superlattice with streaks.

A boundary between the inner area and the shell structure could be found clearly in Figure 3-7 (a), suggesting that the inner region and the shell have the different structures. It should be noted here that the composition of the nanowire was MoS₂ (Raman and EDS). The shell of the nanowire was multilayers and the corresponding diffraction pattern has been observed in Figure 3-7 (b). Moreover, there was no diffuse rings from amorphous found in the diffraction pattern, indicating that the inner region was void and the nanowire was hollow.

The top end of the MoS₂ nanowires was characterized by FESEM and TEM. The results are shown in Figure 3-8. From Figure 3-8 (a), we can see that the cross section of the nanowire was in rectangular shape. When it comes to the TEM image, a cap at the top end of the nanowire could be observed, as shown in Figure 3-8 (b). It is suggested that the reason of the curvature of the top is due to the frustum shape of the seed FeO catalyst particles (shown in Figure 3-4) of vapor-solid (VS) growth mechanism, which will be discussed in detail in the growth mechanism part.

Above all, I can describe the structure of the nanowires synthesized by CVD with 30 nm six-horned FeO catalyst particles. The nanowires were multilayered and have a hollow structure. The cross section of the nanowire was in rectangular shape and the end was closed. The schematic illustration of the nanowire structure are shown in Figure 3-9.

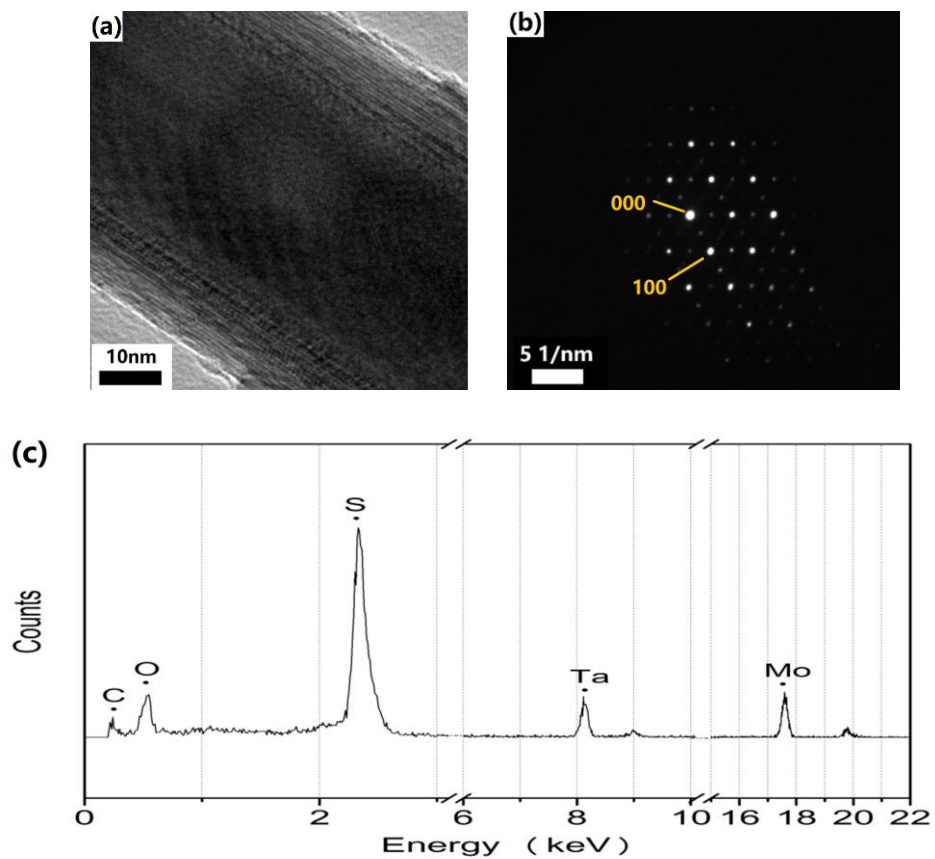


Figure 3-7. (a) TEM image, (b) SAED image and (c) EDS of a MoS₂ nanowire.

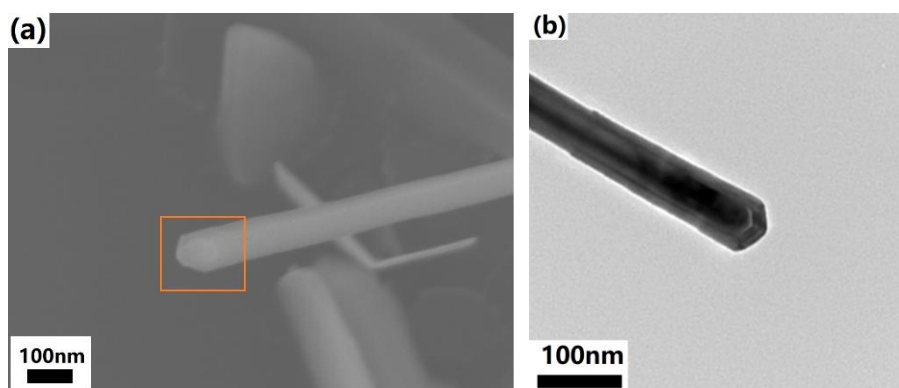


Figure 3-8. (a) SEM image and (b) TEM image of a top end of a MoS₂ nanowire.

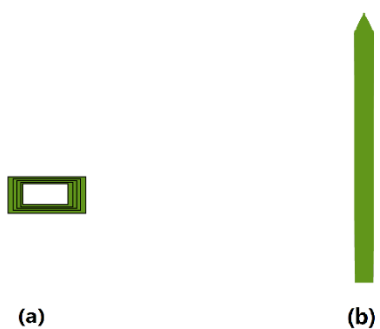


Figure 3-9. The schematic illustration of the nanowire structure: (a) cross section and (b) the whole nanowire.

Chirality of the MoS₂ nanowires

It is essential to determine the chirality of the nanowires, as it is closely associated with the application to edge-based catalysts [32], valleytronics [33] and superconductivity [34], as I mentioned in the Chapter 1. The chirality of the MoS₂ nanowires was determined by the way the sheet of MoS₂ was wrapped, as shown in Figure 3-10 (a). In the case of “zigzag” structure, the direction of the Mo-Mo (or S-S) nearest neighbor is perpendicular, 30 ° or 150 ° off to the nanowire; whereas in the case of “armchair” structure, the direction of Mo-Mo (or S-S) nearest neighbor is parallel, 60 ° or 120 ° off to the direction of the nanowire. The schematic illustrations of the zigzag and armchair structure are shown in Figure 3-10 (b) and (c).

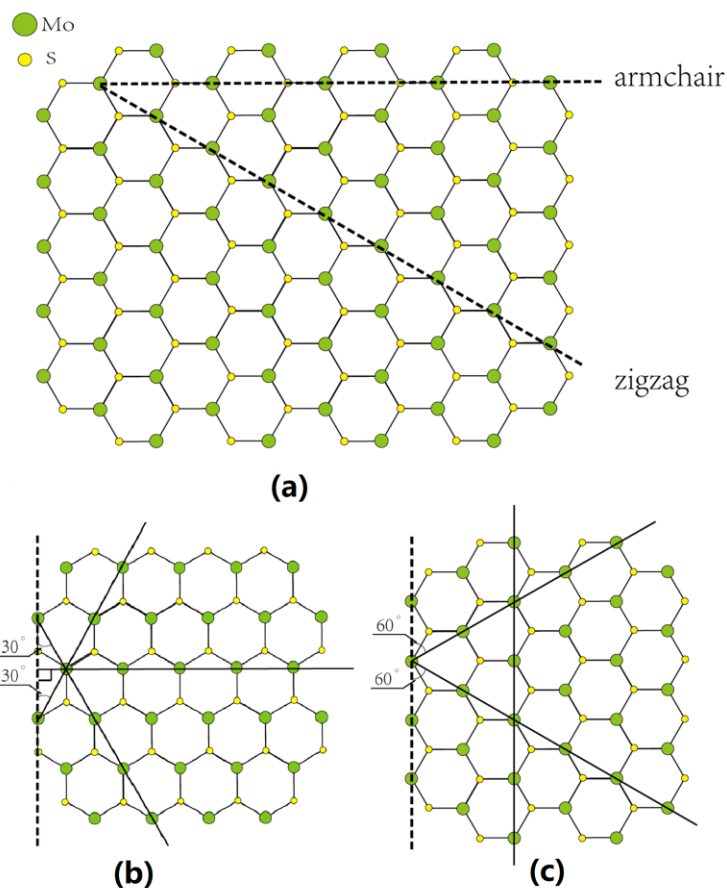


Figure 3-10. Schematic illustrations of (a) the sheet, (b) zigzag and (c) armchair structure.

From the diffraction pattern of the TEM image, as shown in Figure 3-7 (b), we can see that the length of the nanowire and the hexagonal lattice are aligned parallel. The direction of 100 diffraction is 30° off to the orientation of the nanowire. As it is well known, in the hexagonal system, the reciprocal lattice is 30°-rotated from the real-space lattice. Thus, the direction of S-S (or Mo-Mo) nearest neighbor is parallel to the orientation of the nanowire, indicating that the nanowire shown in Figure 3-7 (a) was in armchair structure. The model structure of MoS₂ nanowires is shown in Figure 3-11.

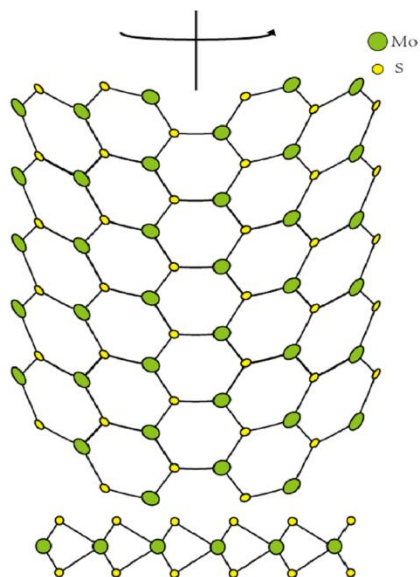


Figure 3-11. The model structure of MoS₂ nanowires synthesized with 30 nm six-horned FeO nanoparticles by CVD method.

Growth mechanism of MoS₂ nanowires

As introduced in the general introduction, a detailed understanding of the growth mechanism of the grown nanowires is an essential foundation for the ultimate control of the nanowire morphology and composition. To identify the growth mechanism, the physical phases of the feeder and the catalytic nanoparticles during the synthesis process are essential to be determined. The feeder phase, which is the phase of source materials incorporated into the nanowires, is in a range of phases, such as solid, gas, liquid, solution. The structure of the catalytic nanoparticles has been explained into a variety of phases, such as liquid, alloy, eutectic and solid. Thus, the growth mechanism of the nanowires is labelled as VLS, VSS, VS, solid-liquid-solid, solution-liquid-solid or others.

The heat conditions of our experiment are as follows: three distinct temperatures (280 °C for sulfur source, 650 °C for MoO₃, and 1000 °C in the growth zone) and the pressure was an atmospheric pressure and the reaction time was 1 h. During the nanowire growth, the Ar gas would carry the MoO₃ and sulfur (40 sccm of MoO₃, and 800 sccm of sulfur vapor) into the reaction zone. Thus, the feeder phases of our experiment were in vapor phase, suggesting that the growth mechanism was among VLS, VSS and VS.

In VLS mechanism [35-40], the structure of catalyst particles is liquid alloy at the reaction temperature. The precursor materials will be dissolved into the liquid alloy to form supersaturation, which will lead to the nucleation of the nanowires. The nanowire growth is by the continued process absorption of the precursor materials and precipitation of the supersaturated liquid particles. In VSS mechanism [41, 42], the catalytic particles are kept solid during the reacted process. The atoms of the precursor materials will be delivered to the surface of the catalyst particles and incorporated at the growth interface, which will lead to the growth of the nanowires. In both VLS and VSS, the catalyst particles are at the top end of the wire, which is a typical feature to distinguish them from VS.

TEM equipped EDS was used to characterize the top morphology and composition of the nanowire, as shown in Figure 3-12. From the TEM image [Figure 3-12 (a)], the tip of the nanowire was closed but no nanoparticles could be observed. EDS was also taken to measure the composition of the tip layer, as shown in Figure 3-12 (c). The intensive peaks of Mo and sulfur indicate that the tip of the nanowire was composed of only MoS₂. Thus, we can understand that the growth mechanism of the MoS₂ nanowires is not VLS or VSS. It is in VS growth mechanism.

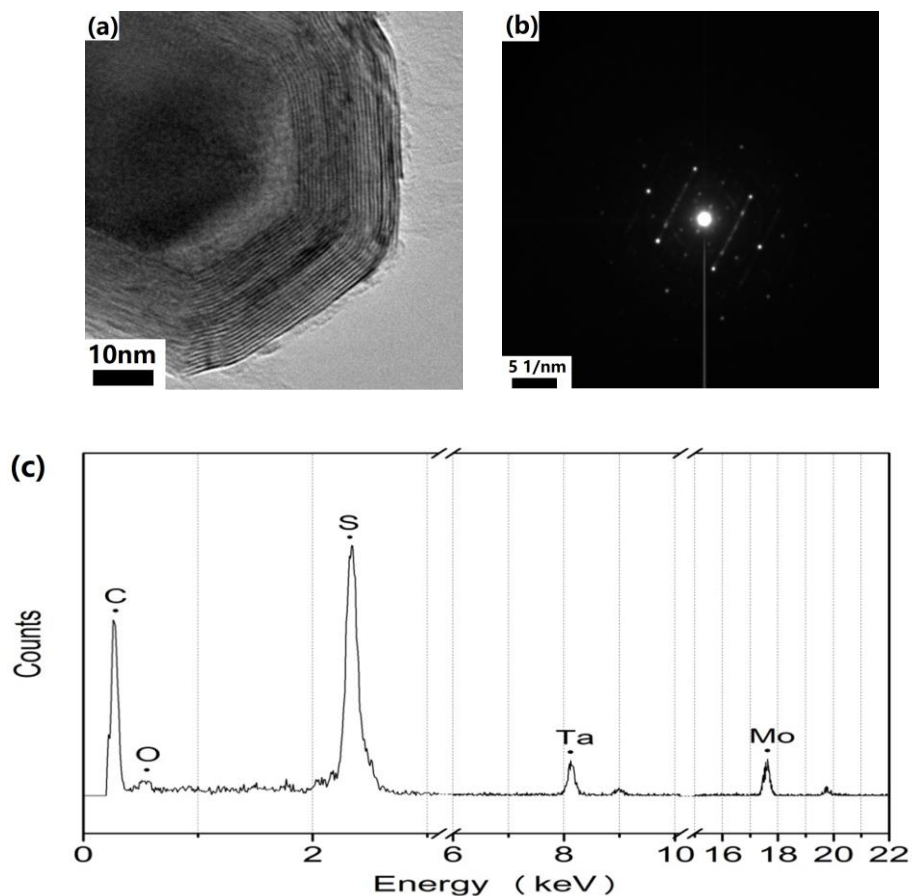


Figure 3-12. (a) TEM image, (b) SAED image and (c) EDS of the tip of MoS₂ nanowire.

The melting point of the FeO is 1377 °C [43], and it will be decreased when it is in nanosize. The morphology of the FeO nanoparticles after heating to 1000 °C has been observed (Figure 3-4). The shape of these nanoparticles was changed from six-horned octahedra to frustums, but the shape edges and the acute angles have still existed. The schematic image of the FeO nanoparticles with frustum shape is shown in Figure 3-13.



Figure 3-13. Schematic image of the frustum shape.

Since the flows of precursor materials (sulfur and MoO₃) in our experiments were separated, the composition of the nuclei sites at the nucleation step is supposed to be MoO_x or MoS₂. On one hand, I conducted a CVD experiment with only MoO₃ flow to demonstrate whether MoO₃ nanowires could be grown in the given conditions with six-horned FeO nanoparticles. SEM was used to characterize the morphology of the products, as shown in Figure 3-14. From the image, we can see the surface of the substrate was partially covered by thin films. No nanotubes or nanowires were observed on the substrates, indicating that MoO_x cannot be the nuclei sites for the growth of nanowires. On the other hand, as I discussed in Chapter 2, the layered structure could be found in the Fe-Mo-S system [44]. The formation of layered Fe_xMoS₂ seeds was supposed to be attribute to the nucleation of MoS₂ nanowires.

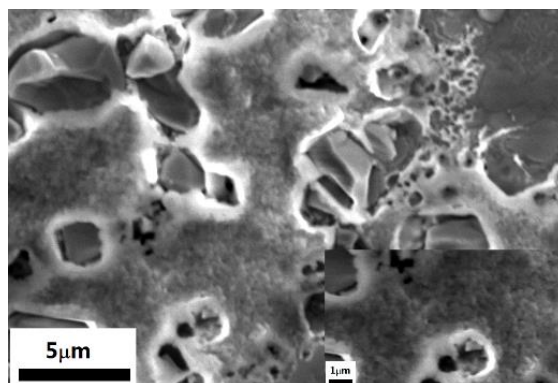


Figure 3-14. SEM image of the CVD results with flowing only MoO₃.

In the growth step, two assumptions were made to describe the process, as shown in Figure 3-15 (a) and (b). One of them is that the nanowires are grown from bottom to top, and another one is that the nanowires are grown from thin to thick.

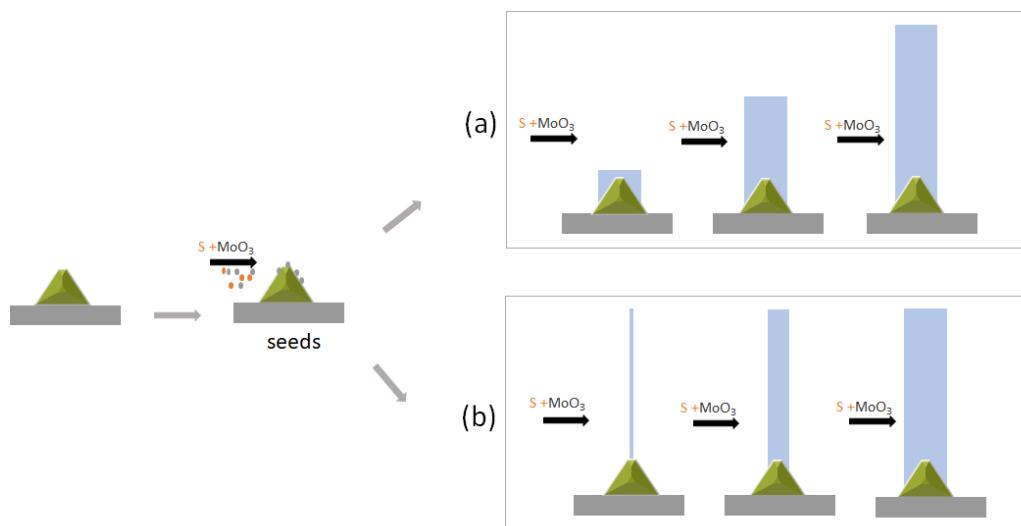


Figure 3-15. Two assumptions of MoS₂ nanowires growth process.

The morphologies of the products in these two assumptions are totally different. To determine the growth process of the nanowires, some experiments were conducted. Firstly, CVD experiments with different growth time (5 and 30 min) were taken. The SEM images are shown in Figure 3-16. In the case of 30 min, the length of the nanowires was about 1 μm and the diameter of them was about 40-80 nm. Compared them with the results of 60 min (Figure 3-5, the length was about 10 μm and the diameter was 40-80 nm), it is obvious that the length of the nanowires was increased while the diameter of the nanowires had no significant change, indicating that the growth process of the nanowires may be well described by assumption one.

Then, CVD experiment with two heating temperatures was conducted. The conditions are as follows: the heating temperature of sulfur source and reaction zones were kept the same as the MoS₂ nanowires growth; the heating temperature of the MoO₃ was separated into two steps: 650 $^{\circ}\text{C}$ for 30min and 630 $^{\circ}\text{C}$ for 30min. The results are shown in Figure 3-16. Figure 3-16 (b) is the high magnification image of Figure 3-16 (a). From the image,

we can clearly observe a shrink in the middle of the nanowire, indicating that the diameter of the nanowires decreased with decrease of the temperature. Furthermore, from the change of the nanowire diameter with the different heating temperatures, it can be speculated that the length of the nanowires is increased when the growth time is extended, which further confirms that the growth process is from bottom to top.

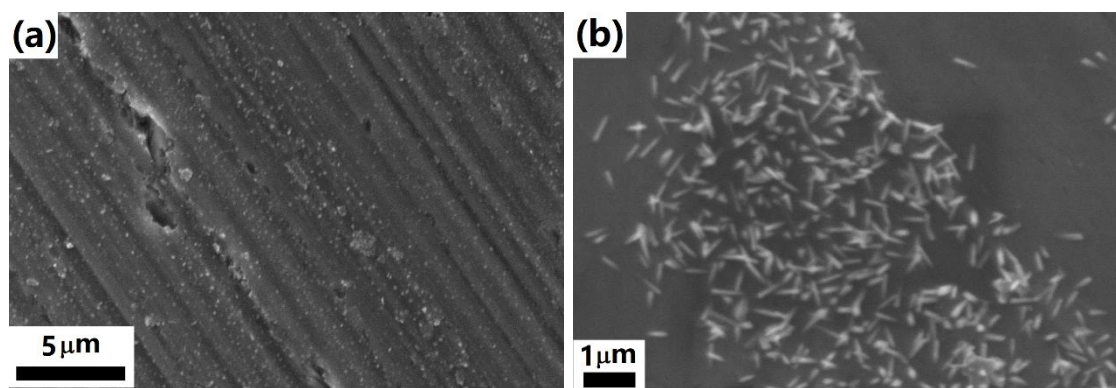


Figure 3-16. CVD results with different growth time: (a) 5 min and (b) 30 min.

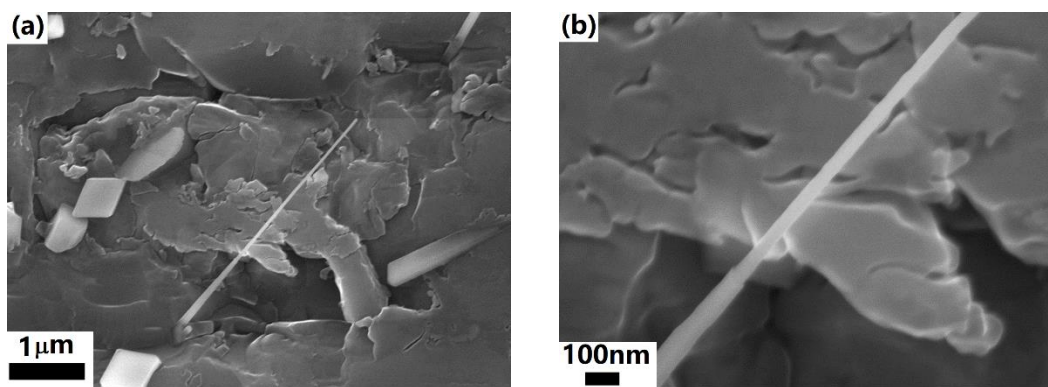


Figure 3-16. (a) SEM image and (b) high magnification SEM image of the nanowires grown with the changed temperature.

Finally, the growth mechanism of the MoS₂ nanowires is described as follows:

- (1) At the first stage, the six horned FeO nanoparticles are turned into frustum shape at the high temperature.
- (2) The nuclei sites will be formed by the formation of layered Fe_xMoS₂ seeds.
- (3) The initially formed nuclei sites could promote the further growth of the nanowires in the presence of sulfur and MoO₃ vapor.

3.4 Conclusions

In this Chapter, I have successfully synthesized the 30 nm six-horned FeO nanoparticles and used it as the catalyst for the growth of MoS₂ nanowires. SEM, FESEM, XRD, Raman and TEM were used to characterize the morphology and the structure of the FeO nanoparticles and MoS₂ nanowires. It was found that the nanowires were multilayered and had a hollow structure. The cross section of the nanowires exhibited rectangular shape and the end was closed. The direction of S-S (or Mo-Mo) nearest neighbor was parallel to the orientation of the nanowire indicating that the nanowires were in armchair structure. The growth mechanism of the nanowires was proved to be VS growth.

References:

1. S. Link and M.A. El-Sayed, *J. Phys. Chem. B*, 2005, **109**, 10531-10532.
2. S. Eustis and M. El-Sayed, *J. Phys. Chem. B*, 2005, **109**, 16350-16356.
3. K. Lee and M.A. El-Sayed, *J. Phys. Chem. B*, 2005, **109**, 20331-20338.

4. A. Magrez, S. Kasas, V. Salicio, N. Pasquier, J.W. Seo, M. Celio, S. Catsicas, B. Schwaller and L. Forró, *Nano Lett.*, 2006, **6**, 1121-1125.
5. M. Lucas, W. Mai, R. Yang, Z.L. Wang and E. Riedo, *Nano Lett.*, 2007, **7**, 1314-1317.
6. C. Greiner, A. Del Campo and E. Arzt, *Langmuir*, 2007, **23**, 3495-3502.
7. J. Li, P.C. Ma, W.S. Chow, C.K. To, B.Z. Tang and J.K. Kim, *Adv. Funct. Mater.*, 2007, **17**, 3207-3215.
8. Y. Du, L. Shi, T. He, X. Sun and Y. Mo, *Appl. Surf. Sci.*, 2008, **255**, 1901-1905.
9. Y.Y. Wei, G. Eres, V.I. Merkulov and D.H. Lowndes, *Appl. Phys. Lett.*, 2001, **78**, 1394-1396.
10. Y. Li, J. Liu, Y. Wang and Z.L. Wang, *Chem. Mater.*, 2001, **13**, 1008-1014.
11. S.H. Overbury, L. Ortiz-Soto, H. Zhu, B. Lee, M.D. Amiridis and S. Dai, *Catalysis Letters*, 2004, **95**, 99-106.
12. V. Jourdain and C. Bichara, *Carbon*, 2013, **58**, 2-39.
13. H. Wang, Y. Yuan, L. Wei, K. Goh, D. Yu and Y. Chen, *Carbon*, 2015, **81**, 1-19.
14. C. Hoecker, F. Smail, M. Bajada, M. Pick and A. Boies, *Carbon*, 2016, **96**, 116-124.
15. S. Sun and H. Zeng, *J. Am. Chem. Soc.*, 2002, **124**, 8204-8205.
16. T. Hyeon, *Chem. Commun.*, 2003, 927-934.
17. W. Wu, Q. He and C. Jiang, *Nanoscale Res. Lett.*, 2008, **3**, 397-415.
18. Y. Hou, Z. Xu and S. Sun, *Angew. Chem.*, 2007, **119**, 6445-6448.
19. S. Laurent, D. Forge, M. Port, A. Roch, C. Robic, L. Vander Elst and R.N. Muller, *Chem. Rev.*, 2008, **108**, 2064-2110.
20. P. Liu, W. Cai and H. Zeng, *J. Phys. Chem.C*, 2008, **112**, 3261-3266.

21. M. Gheisari, M. Mozaffari, M. Acet and J. Amighian, *J. Magn. Magn. Mater.*, 2008, **320**, 2618-2621.
22. N.A. Frey, S. Peng, K. Cheng and S. Sun, *Chem. Soc. Rev.*, 2009, **38**, 2532.
23. Z. Xu, C. Shen, Y. Hou, H. Gao and S. Sun, *Chem. Mater.*, 2009, **21**, 1778-1780.
24. R. Strobel and S.E. Pratsinis, *Adv. Powder Technol.*, 2009, **20**, 190-194.
25. S.K. Sharma, J.M. Vargas, K.R. Pirota, S. Kumar, C.G. Lee and M. Knobel, *J. Alloy. Compd.*, 2011, **509**, 6414-6417.
26. R. Strobel and S.E. Pratsinis, *Adv. Powder Technol.*, 2009, **20**, 190-194.
27. H.T. Hai, H.T. Yang, H. Kura, D. Hasegawa, Y. Ogata, M. Takahashi and T. Ogawa, *J. Colloid Interf. Sci.*, 2010, **346**, 37-42.
28. S.K. Sharma, J.M. Vargas, K.R. Pirota, S. Kumar, C.G. Lee and M. Knobel, *J. Alloy. Compd.*, 2011, **509**, 6414-6417.
29. M. Weng, T. Yanase, F. Uehara, S. Watanabe, T. Miura, T. Nagahama and T. Shimada, *CrystEngComm*, 2017, **19**, 3915-3920.
30. M. Weng, M. Zhang, T. Yanase, F. Uehara, T. Nagahama and T. Shimada, *Jpn. J. Appl. Phys.*, in press.
31. T. Yanase, S. Watanabe, M. Weng, T. Nagahama, and T. Shimada, *J. Nanosci. Nanotechnol.*, 2016, **16**, 3223-3227.
32. B. Hinnemann, P.G. Moses, J. Bonde, K.P. Jørgensen, J.H. Nielsen, S. Horch, I. Chorkendorff, and J.K. Nørskov, *J. Am. Chem. Soc.*, 2005, **127**, 5308-5309
33. J.R. Schraibley, H. Yu, G. Clark, P. Rivera, J. S. Ross, K.L. Seyler, W. Yao, and X. Xu, *Nature Rev. Mater.* 2016, **1**, 16055.

34. F. Qin, W. Shi, T. Ideue, M. Yoshida, A. Zak, R. Tenne, T. Kikitsu, D. Inoue, D. Hashizume, and Y. Iwasa, *Nat. Commun.*, 2017, **8**, 14465.
35. R.S. Wagner, W.C. Ellis, K.A. Jackson and S.M. Arnold, *J. Appl. Phys.*, 1964, **35**, 2993-3000.
36. Z. Xiao, L. Zhang, G. Meng, X. Tian, H. Zeng and M. Fang, *J. Phys. Chem. B*, 2006, **110**, 15724-15728.
37. S. Chen, P. Ying, L. Wang, F. Gao, G. Wei, J. Zheng, Z. Xie and W. Yang, *RSC Adv*, 2014, **4**, 8376-8382.
38. A. Gomez-Martinez, F. Márquez and C. Morant, *J. Sol-Gel Sci. Techn.*, 2017, **81**, 321-326.
39. K. Lin, P. Yao, J. Zhao, S. Guo and F. Tian, *Mater. Lett.*, 2017, **203**, 21-23.
40. A. Jaud, L. Auvray, A. Kahouli, T. Abi-Tannous, F. Cauwet, G. Ferro and C. Brylinski, *Physica Status Solidi (a)*, 2017, **214**, 1600428.
41. J.L. Lensch-Falk, E.R. Hemesath, D.E. Perea and L.J. Lauhon, *J. Mater. Chem.*, 2009, **19**, 849.
42. C.Y. Wen, M.C. Reuter, J. Tersoff, E.A. Stach and F.M. Ross, *Nano Lett.*, 2010, **10**, 514-519.
43. FeO, [https://en.wikipedia.org/wiki/Iron\(II\)_oxide](https://en.wikipedia.org/wiki/Iron(II)_oxide).
44. G. Bergerhoff and I.D. Brown, in "Crystallographic Databases", F.H. Allen et al. (ed.) Chester, International Union of Crystallography, 1987.

Chapter 4. Size and shape effects of catalyst nanoparticles

4.1 Introduction

In Chapter 3, I have successfully synthesized MoS₂ nanowires by catalytic CVD with synthesized 30 nm six-horned octahedra FeO nanoparticles. As I mentioned in the general introduction, 1D MoS₂ nanostructures are promising materials for the application in gas sensors [1-8], transistors [9-18] and solar cells [19-24]. The properties of the nanowires are dominated by the physical and the chemical structures. For example, the length and the diameter of the nanowires are critical factors for their sensitivity as sensors and catalytic activities [25-27]. The composition, crystal structure, impurities, the facets of the nanowires are closely linked to the band gap tuning and chemical stability [28-34]. Thus, the controlled fabrication of the nanowires is a key issue to be investigated.

I have studied in Chapter 3 that the growth mechanism of MoS₂ nanowires synthesized in our experiment is VS mechanism. The growth of the MoS₂ nanowires includes two steps: the nucleation and the growth. In the nucleation step, the precursor materials were transported and deposited on the surface of the catalytic nanoparticles with frustum shape to form nuclei sites. In the growth step, the MoS₂ nanowires were grown by sequential incorporation of the precursor materials in the presence of sulfur and MoO₃ vapor. In this method, the physical and chemical structures of the nanowires are dependent

on several factors, such as the catalytic activities of the catalysts, the reaction temperatures as well as the proportion of the reactants in the carrier gas flow.

In this Chapter, I will focus on the effects of the catalytic FeO nanoparticles with different shapes and sizes on the morphology and composition of the nanowires synthesized by the catalytic CVD. When using different shapes of the FeO nanoparticles, I found a switching of the products between SiO_x nanowires and MoS₂ nanowires. SiO_x nanowires were grown in the presence of spherical nanoparticles, whereas MoS₂ nanowires were formed in the presence of six-horned octahedral nanoparticles. The crystal structures, morphology and element composition have been fully investigated to explain the reason of the switching. [35]

4.2 FeO nanoparticles

In Chapter 3, I have reported the synthesis of 30 nm six-horned octahedra FeO particles by the thermal decomposition of Fe(acac)₃ in the mixture of OA and OAm. Many factors have been believed to play significant roles in determining the final nanoparticles. Some of them have been published in literature [36], such as the decomposition time and the composition of the solution, while many other factors were paid little attention. Thus, the section below will give information about the effects of several other factors on the final products. It should be noted here all the decomposition experiments of Fe(acac)₃ were under Ar atmosphere and the products are composed of FeO.

4.2.1 Synthesis

The thermal deposition of $\text{Fe}(\text{acac})_3$ was taken under different conditions. The process is similar with the case of 30 nm six-horned octahedral FeO nanoparticles described in Chapter 3: firstly, a suspension of 0.7g $\text{Fe}(\text{acac})_3$ in the mixture of OA and OAm were heated to 120 °C to remove the air and humid. Then it was heated to 220 °C and kept for a set time. Finally it was heated to 300 °C at the rate of 2 °C/min and also kept for a set time. The schematic flow chart is shown in Figure 4-1. TEM was employed to characterize the morphology of the nanoparticles.

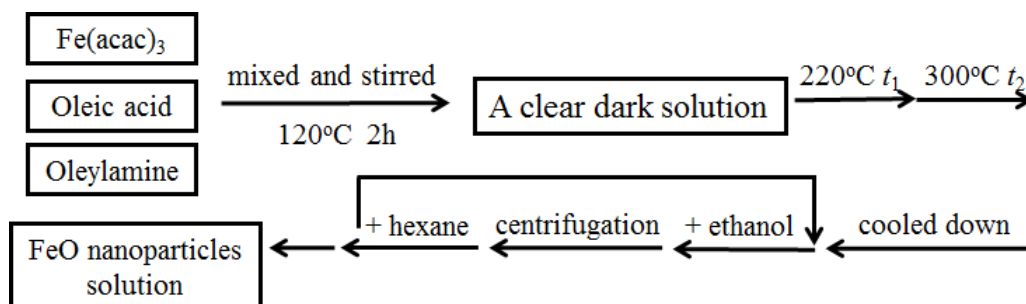


Figure 4-1. The flow chart of the FeO particles synthesis.

Table 4-1. The conditions of the FeO particles synthesis.

	d_{FeO}	V_{OA}	V_{OAm}	t_1	t_2	stirring
(a)	9 nm	4 ml	6 ml	0.5 h	0.5 h	×
(b)	24 nm	5.5 ml	5 ml	0.5 h	1 h	○
(c)	30 nm	5.5 ml	5 ml	0.5 h	0.5 h	×
(d)	50 nm	5.5 ml	5 ml	0.5 h	1 h	×
(e)	100 nm	5.5 ml	5 ml	1 h	1 h	×

4.2.2 OA/OAm ratio

As reported in the literature [36], both of OA and OAm are acted as surfactants and solvents, promoting the stabilization of FeO nanoparticles. In their experiments, the spherical FeO nanoparticles were fabricated in the mixture of 8 ml OA and 12 ml OAm, while the truncated octahedra FeO nanoparticles were synthesized in the mixture of 10 ml OA and 10 ml OAm. The explanation are as follows: OA can promote the growth in the (100) direction, giving a rise in the truncated octahedra shape of the nanoparticles, while OAm can facilitate the growth in all the crystal plane, leading to the formation of spherical shape.

In our experiment, the similar results were obtained when we used the excess OAm in the mixture of OA and OAm. The conditions of the experiments are shown in Table 4-1 (a) and (c). Figure 4-2 displays the results. When I used the mixture of 4 ml OA and 6ml OAm, 14 nm spherical FeO nanoparticles were fabricated, as shown in Figure 4-2(a); while the mixture of 5 ml OA and 5.5 ml OAm was used, 30 nm six-horned octahedral FeO nanoparticles (the one I used in Chapter 3) were formed. The similar results to the literature indicate that we can control the shape of the FeO nanoparticles by regulating the composition ratio of the OA and OAm mixture.

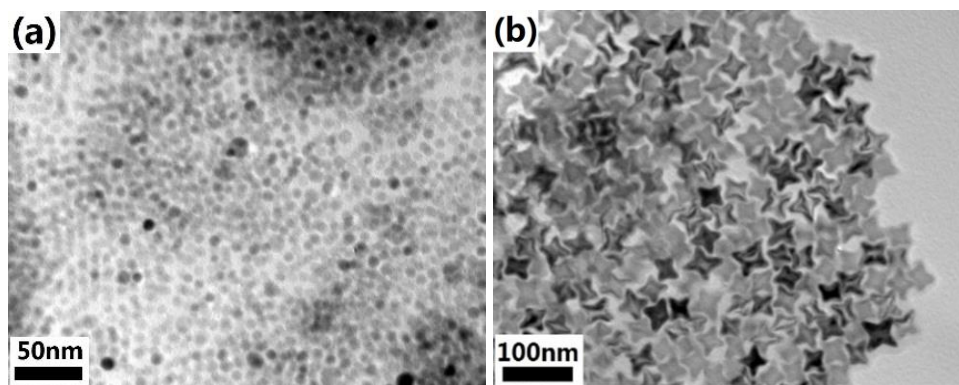


Figure 4-2. TEM images of the (a) 14 nm spherical FeO nanoparticles and (b) 30 nm six-horned octahedral FeO nanoparticles.

4.2.3 Decomposition temperature

The decomposition process of $\text{Fe}(\text{acac})_3$ in air has been reported in literature, as shown in Figure 4-3 and Figure 4-4 [37]. It could be seen that the decomposition of the $\text{Fe}(\text{acac})_3$ is step by step at different temperature ranges. Between 195.11°C to 232.66°C , the first acetylacetonate group is removed from $\text{Fe}(\text{acac})_3$ and the second one is removed between 232.66°C to 264.01°C . The removal of the third acetylacetonate group occurs from 264.01°C to 361.49°C to form the iron oxides. From the described process, we can see that the third process (I will call it “formation temperature” below) is the crucial for the form of the nanoparticle shape. The temperature I used to synthesize 30 nm six-horned octahedral FeO nanoparticles was 300°C . Thus, it is of great interest to study the effect of the formation temperature on the shape and the size of the nanoparticles.

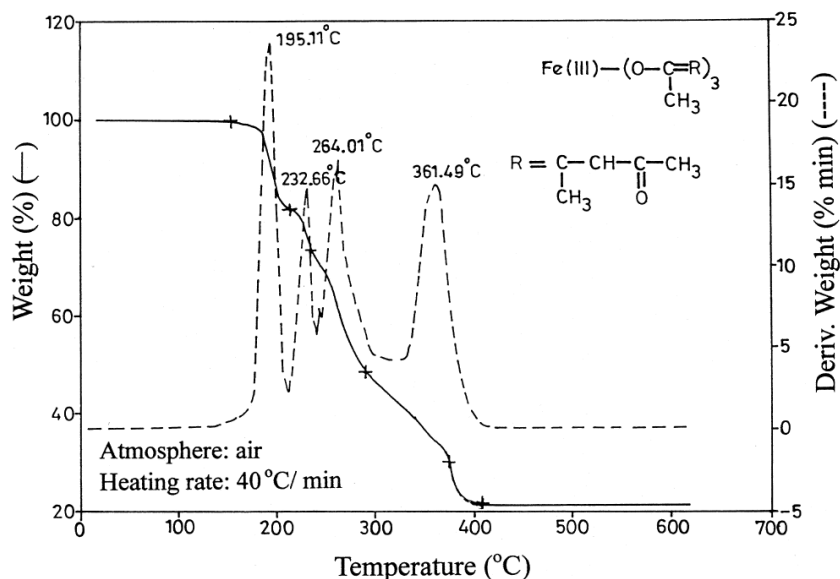


Figure 4-3. TGA plot of the $\text{Fe}(\text{acac})_3$ decomposed in air. [37]

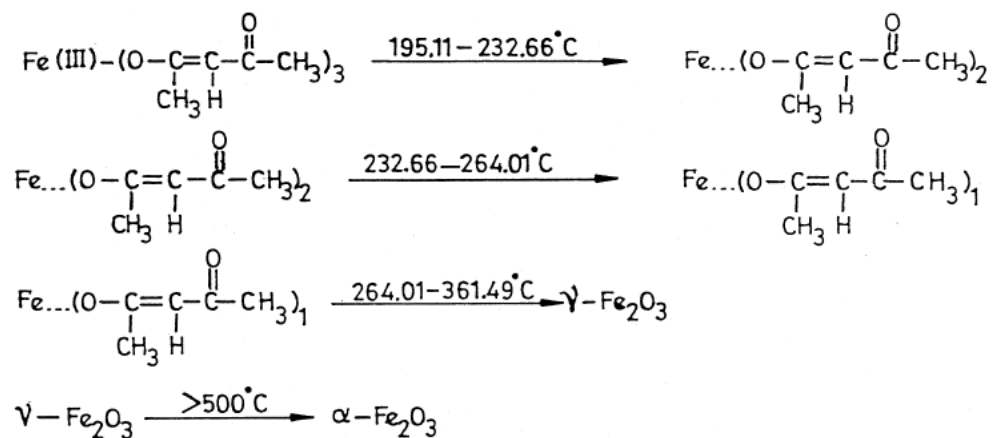


Figure 4-4. Scheme of the $\text{Fe}(\text{acac})_3$ decomposition steps.[37]

The formation temperature of the nanoparticles I chose was 270 °C, 280 °C, 290 °C, 300 °C. It should be noted here that the other conditions were the same, as shown in Table 4-1 (c). The TEM images of the results are shown in Figure 4-5. From the images, we can see the shapes of the nanoparticles differed from the various formation temperatures. Kept

at 270 °C for 30 min, six-horned octahedron shape was not formed, instead, cuboctahedron shape was formed. When the formation temperature raised to 280 °C, we can see cuboctahedron and six-horned octahedron were both existed, as shown in Figure 4-5 (b). When the temperature increased to 290 °C and 300 °C, 25 nm and 30 nm six-horned octahedra nanoparticles with mono-dispersity were fabricated, respectively, as shown in Figure 4-5(c) and (d). The changing process of the nanoparticle shape from lower to higher temperature suggests that the higher formation temperature can facilitate the formation of the nanoparticles and the size of the nanoparticles can be controlled slightly by setting the different formation temperature.

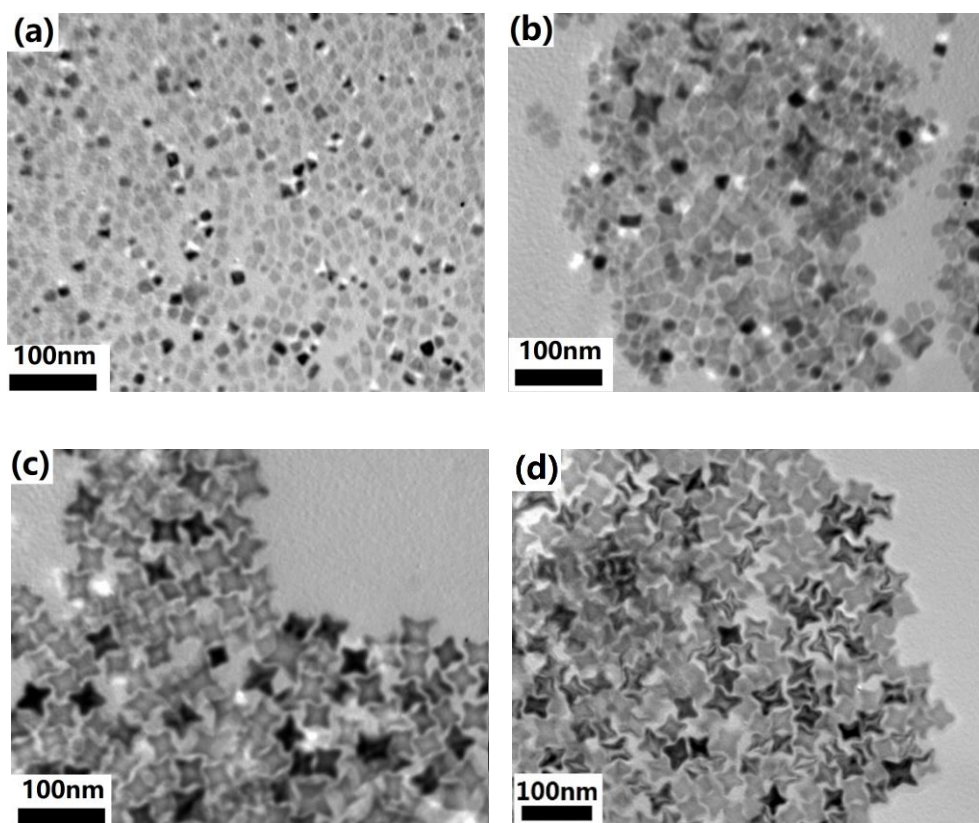


Figure 4-5. TEM images of the FeO nanoparticles synthesized at (a) 270 °C, (b) 280 °C , (c) 290 °C and (d) 300 °C.

4.2.4 Deposition time

The deposition time kept at the heat temperature is an important factor to control the size of the nanoparticles, as reported [36]. The size of the nanoparticles is increased with longer deposition time at the heat temperatures. To synthesize a series size of the six-horned octahedra FeO nanoparticles, the experiments [Table 4-1(c), (d) and (e)] were conducted. TEM was used to characterize the morphologies of the nanoparticles, as shown in Figure 4-6. 30 nm six-horned octahedral FeO nanoparticles, which was obtained by heating the mixture at 220 °C for 30 min and 300 °C for 30 min. When the decomposition time at 220 °C increased to 60 min, 50 nm six-horned octahedral FeO nanoparticles were acquired, as shown in Figure 4-6 (a). Furthermore, when both of the decomposition time at 220 °C and 300 °C increased to 60 min, 100 nm six-horned octahedral FeO nanoparticles were obtained, as shown in Figure 4-6 (b).

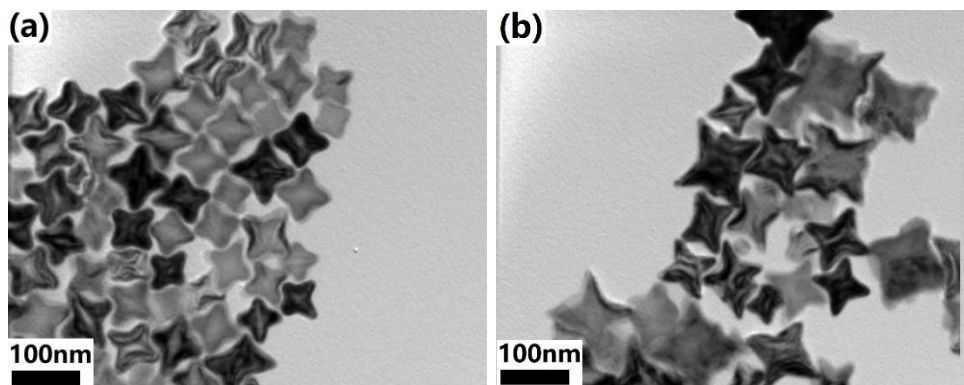


Figure 4-6. TEM images of the (a) 50 nm and (b) 100 nm six-horned octahedral FeO nanoparticles.

4.3.5 Stirring

All the decomposition experiments were kept stirring at 120 °C for the purpose of removing the air and the water in the mixture; but the effect of stirring at the decomposition temperature is still remained a question. I will discuss the effect of stirring on the morphology of the nanoparticles in this section. The experiment conditions are presented in Table 4-1 (b) and (d). The TEM images of the nanoparticles are shown in Figure 4-7. From the images, we can find that the 50 nm six-horned octahedral nanoparticles were transferred into 24 nm spherical nanoparticles when I kept stirring during the whole experiment. The effect of the stirring on the formation of the nanoparticles is supposed to be the reason of the shape and size change of the nanoparticles.

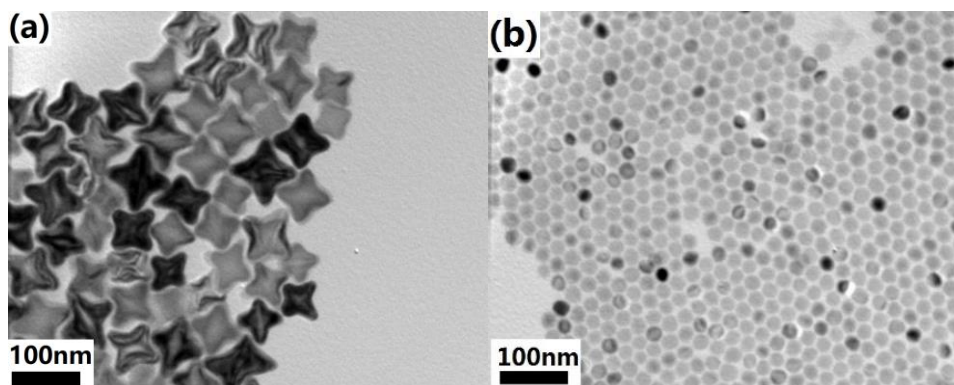


Figure 4-7. TEM images of the (a) 50 nm six-horned octahedral FeO nanoparticles and (b) 24 nm spherical FeO nanoparticles.

I have discussed the effect of factors on the size and shape of the nanoparticles, such as the composition of the mixture, the decomposition temperature and time, and the stirring during the decomposition. Furthermore, I can control the size and shape of the nanoparticles by regulating the decomposition conditions. In the following sections, I will

discuss the shape and size effects of the catalysts on the morphology and composition of the nanowires.

4.3 Shape effect of the catalysts

Little attention has been paid on the effect of the shape of catalysts on the CVD nanowires growth in any materials. In this work, I have synthesized different shapes of FeO nanoparticles, thus it is interesting to investigate the morphology and the composition of nanowires when I used the catalysts with different shapes. The FeO nanoparticles I chose as the catalysts were 9 nm, 24 nm spherical and 30 nm six-horned octahedral particles, as shown in Figure 4-8.

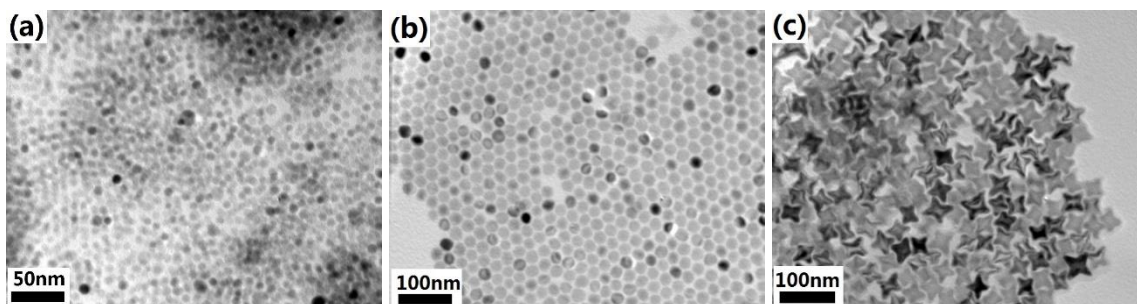


Figure 4-8. TEM images of (a) 9 nm, (b) 24 nm spherical and (c) 30 nm six-horned octahedral FeO nanoparticles.

XRD was employed to characterize the crystal structures of these nanoparticles, as shown in Figure 4-9. It can be seen in the figure that the characteristic peaks (111), (200), (220), (311) and (222) of FeO fcc structure can be observed in all the samples, demonstrating that the particles I used are composed of FeO. Also, the smaller shoulder at 34.5° can be found in the three cases, indicating that the particles I synthesized by the

thermal decomposition of the $\text{Fe}(\text{acac})_3$ in the mixture of OA/OAm were surrounded by a layer of Fe_3O_4 coating.

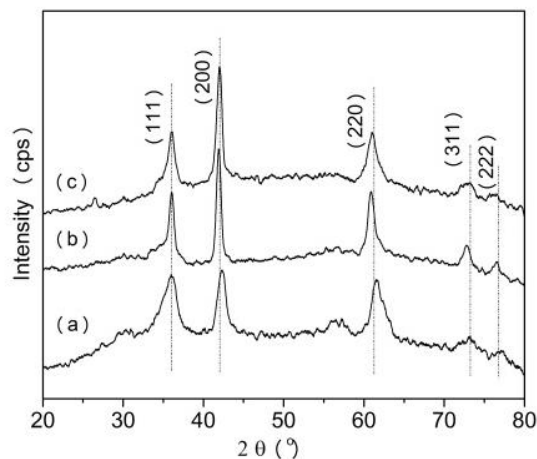


Figure 4-9. XRD patterns of FeO nanoparticles: (a) 9-nm, (b) 24-nm and (c) 30-nm six-horned octahedral nanoparticles.

Because the experimental conditions of CVD were the same with the one used in Chapter 2 and 3, the morphology of the FeO nanoparticles at 1000 °C is important. The nanoparticles were annealed at 1000 °C and FESEM was used to observe their morphologies as presented in Figure 4-10 and Figure 3-4. Figure 4-10 (a) and (b) display the morphologies of 9 nm and 24 nm spherical nanoparticles heated at 1000 °C, respectively. From the images, we can find that the spherical nanoparticles have turned into dome shape. Comparing the results of the three nanoparticles at 1000 °C, it can be seen that even through some changes in morphology of the nanoparticles have occurred at the reaction temperature, the size and the shape of the three nanoparticles are still distinct from each other. XRD was also used to characterize their composition, as shown in Figure 4-11. As the samples were exposed to air during the XRD process, the peaks of Fe_2O_3 could be observed in all the samples, indicating that FeO was transformed into another stable iron

oxide. In the practical CVD experiment, the apparatus was under Ar atmosphere, by which the transformation of the nanoparticles can be suppressed to a certain degree.

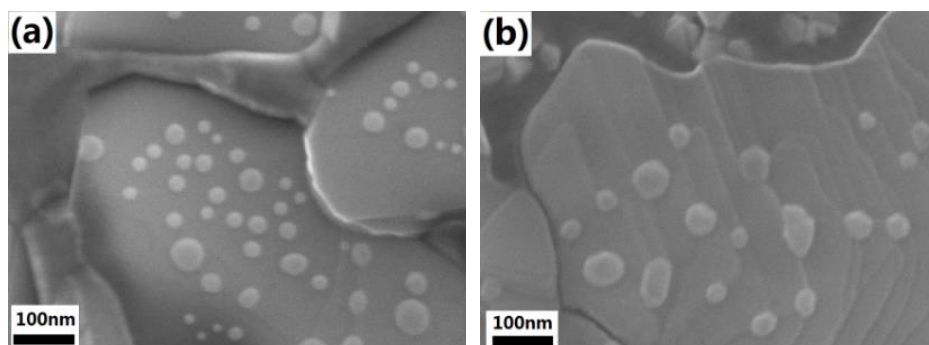


Figure 4-10. FESEM images of the (a) 9 nm and (b) 24 nm spherical nanoparticles heated at 1000 °C.

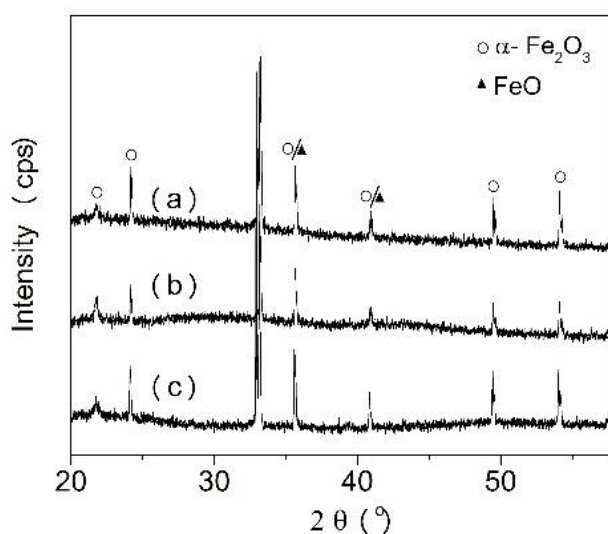


Figure 4-11. XRD of the (a) 9 nm, (b) 24 nm spherical and (c) 30 nm six-horned octahedral nanoparticles heated at 1000 °C.

CVD experiments were taken under the same conditions as in Chapter 2 and 3: the substrates were 285 nm SiO₂/Si substrates, the source materials were MoO₃ and sulfur, the

growth time was 1 hour and the pressure was 1 atm. SEM and FESEM were employed to characterize the morphology of the products grown on the substrates. TEM equipped with EDS was used to identify the composition and structure of the products. Raman spectroscopy was utilized to identify the local structure of the products.

The results after CVD with the 9 nm, 24 nm spherical and 30 nm six-horned octahedral nanoparticles are shown in Figure 4-12(a) ~ (f). The crystal structure and the composition at different locations of the nanowires were measured by TEM equipped with EDS, as shown in Figure 4-13, Figure 3-7 and Figure 3-12. From the given SEM and FESEM images, [Figure 4-12 (a) and (b)]. We can find that when I used the 9 nm spherical FeO particles as the catalyst, nanowires with high aspect ratio were fabricated. The length of the nanowires was in 10 μm and the diameter of the nanowires was around 40 nm. The growth density of the nanowires was high. The structure and composition of the nanowires were identified by TEM and EDS. The results are given in Figure 4-13. It was found that these nanowires were composed of SiO_x . Also, from the TEM image, a particle cap can be observed clearly at the tip of the nanowire, which was composed of Mo, Fe and S elements.

When I used the 24 nm spherical FeO particles as the catalyst, the morphology of the products was changed, as shown in Figure 4-12 (c) and (d). The growth density of the nanowires became lower and the aspect ratio was lower, compared with results of 9 nm spherical FeO particles. Besides the nanowires, most parts of the substrates were covered by MoS_2 films. A cap of particle can be clearly observed on the top of the nanowire, as shown in Figure 4-12(d). It was suggested to be SiO_x nanowires due to the Raman spectra and EDS results.

When I used the 30 nm six-horned octahedra FeO nanoparticles, the MoS₂ nanowires were grown, as shown in Figure 4-12 (e) and (f). The composition, structure and chirality were described in detail in Chapter 3.

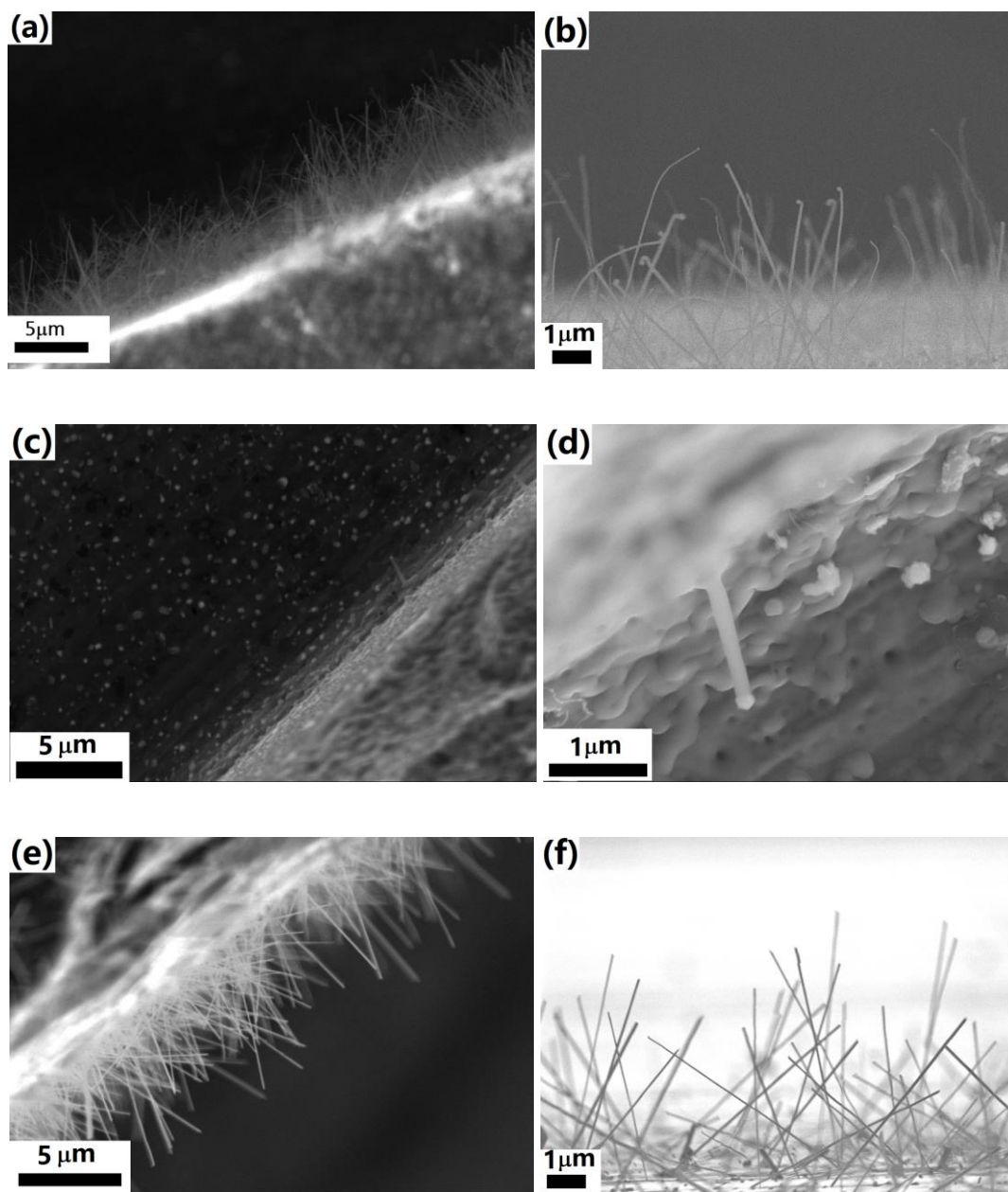


Figure 4-12. SEM images after CVD with (a) (b) 9 nm, (c) (d) 24 nm and (e) (f) 30 nm catalyst nanoparticles.

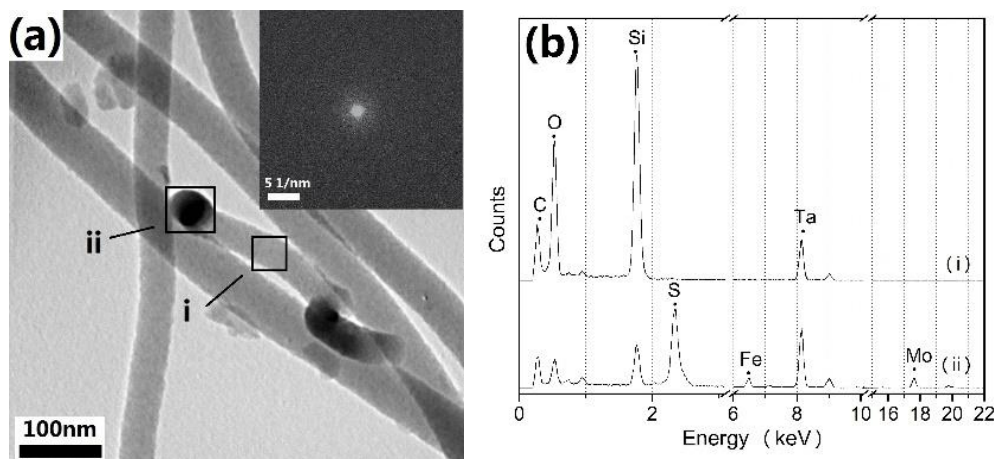


Figure 4-13. (a) TEM image and (b) EDS results of SiO_x nanowires.

Summarizing the above results, I can conclude the shape of catalyst plays an important role in the process of nanowire growth. In the presence of spherical catalyst nanoparticles, SiO_x nanowires were obtained, while in the presence of six-horned octahedral catalyst nanoparticles, MoS_2 nanowires were formed. The results are summarized in the first row of Table 4-2. It is of great interest to investigate the switching of the CVD products with the different shapes of the nanoparticles. As I mentioned in the general introduction, the morphology of the products is closely linked to their growth manner. Thus, it is essential to study on the growth mechanism of these products.

To study the growth process of these nanowires, some additional experiments were needed to be conducted. Similar to the experiments conducted in Chapter 3 (Figure 3-14), the CVD experiments with only flowing MoO_3 (no S) were proceeded and the results are shown in Figure 4-14. From the images, it is clearly shown that randomly dispersed particles were grown on the substrates in all the samples and no nanowires could be found. Raman spectroscopy was used to characterize the composition of these particles. The results using 9 nm, 24 nm spherical and 30 nm six-horned octahedral catalysts are shown

in Figure 4-15 (a), (b) and (c), respectively. In the case of using 9 nm spherical catalysts, the peaks of MoO_x ($x=2$ and 3) and FeO_y ($y=1, 3/2, 4/3$) could be observed, while in the case of using 24 nm spherical catalysts, only peaks of FeO_y could be observed and no MoO_x peaks existed on the curves. These results indicates that MoO_3 tends to be deposited on the smaller spherical nanoparticles. The results of using 30 nm six-horned octahedral catalysts have been described in Chapter 3, in which, the intensive peaks of MoO_x could be found compared to the cases of using 9 nm and 24 nm spherical particles. The morphologies of these nanoparticles at the growth temperature were described in the catalyst section (Figure 4-10 and Figure 3-4): the spherical shape turned into domes and the six-horned octahedra shape became frustums. It is supposed that the intensive deposition of MoO_3 in the case of six-horned octahedra nanoparticles is attributed to the acute angles and sharp edges in frustum shape.

Table 4-2. Summary of the CVD products.

Catalysts (FeO particles)	9 nm sphere	24 nm sphere	30 nm six-horned octahedra
Growth of nanowires (flow MoO_3 and S)	SiO_x nanowires	few SiO_x nanowires	MoS_2 nanowires
MoO_x Raman peaks (only flow MoO_3)	weak	None	strong

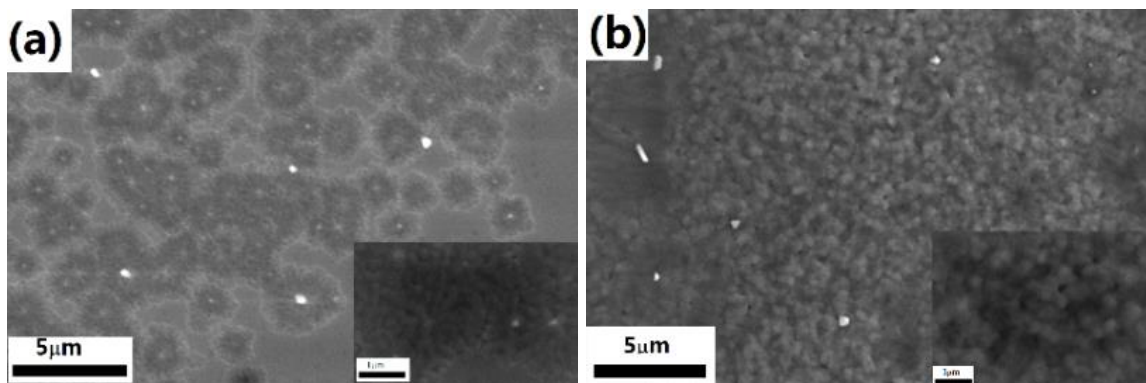


Figure 4-14. SEM images after CVD by flowing MoO_3 on substrates coated with (a) 9 nm and (b) 24 nm FeO particles.

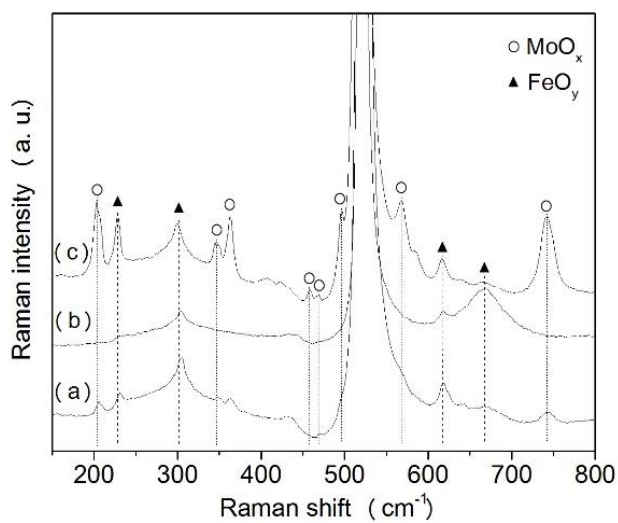


Figure 4-15. Raman spectra after CVD with (a) 9 nm, (b) 24 nm and (c) 30 nm FeO particles by flowing only MoO_3 .

The above experiments were summarized in the second row of Table 4-2. Based on the results presented in Table 4-2, I will describe the growth mechanism in the following sections. The source materials and the growth conditions are as follows: 0.15 g MoO_3 and 1.5 g sulfur were used as the source materials, 285 nm SiO_2/Si substrates were used, the growth temperature was 1000 °C and the pressure was kept at 1 atmosphere.

In the case of 9 nm spherical FeO particles, SiO_x nanowires were grown. The source of SiO_x is suggested to be from the evaporation of SiO since the vapor pressure of SiO₂ at 1000 °C is very low. By reaction $\text{SiO}_2 + \text{S} \rightarrow \text{SiO} + \text{SO}_2$, SiO is produced. Since SiO has a vapor pressure of ~1.33 Pa at 1000 °C [38], it can provide the source for the growth of the SiO_x nanowires.

The partial pressure of MoO₃ during the reaction is estimated from the following panel:

After the CVD, about a 10% mass loss of MoO₃ was found. Therefore, the amount of MoO₃ m_{MoO_3} loaded into the reaction zones is

$$m_{\text{MoO}_3} = 10\% \times 0.15\text{g} = 0.015\text{g}$$

$$n_{\text{MoO}_3} = 0.015\text{g} / 144\text{g/mol} = 10^{-4}$$

The flow rate of Ar with S and MoO₃ is 800 sccm and 40 sccm, respectively. The reaction time is 60 min, and the total volume of Ar is

$$V_{\text{Ar}} = (800+40) \text{ sccm} \times 60 \text{ min} = 51200 \text{ cm}^3$$

The reaction pressure of the system is 1 atmosphere. Thus the estimated partial pressure of MoO₃ is

$$P_{\text{MoO}_3} = 10^5 \times 10^{-4} \times 22.4 \text{ L/mol} / 51.2 \text{ L} = 4 \text{ Pa.}$$

Based on the estimation of partial pressure of MoO₃ and the vapor pressure of SiO recorded in reference [38], it can be speculated that there must be a drastic competition between the two vapors, leading to the fabrication of the two nanowires with different composition and morphologies. The process of products fabricated with the 9 nm, 24 nm spherical and 30 nm six-horned octahedral catalysts are shown in Figure 4-16.

present experiment was 1000 °C. The reaction temperature higher than eutectic point the makes it possible to explain the growth of SiO_x nanowires by VLS mechanism. The process is described as follows:

(1) When the temperature reached 1000°C, the shape of the particles turned into domes.

At the same time, the vapor of MoO₃ and sulfur starts flowing into the reaction zone carried by Ar gas to deposit the precursor atoms (Mo, O and S) on to the particles.

The system of FeO-FeS tends to be formed as the results of the reaction between the sulfur adatoms and partial FeO of the nanoparticles. Besides, MoO₃ tend to evaporate rather quickly rather than diffuse into the particles.

(2) When the composition ratio of FeO and FeS reached a certain value, the eutectic point of the system could be reached. By the dissolution of the SiO vapor into the liquid drop, which is produced from the reaction of $\text{SiO}_2 + \text{S} \rightarrow \text{SiO} + \text{SO}_2$, the supersaturation for the nucleation of SiO_x nanowires occurs.

(3) By the precipitation from the supersaturate liquid, the SiO_x nanowires will be grown.

When the size of the spherical nanoparticles increased to 24 nm, SiO_x nanowires were grown in lower density, suggesting that it becomes difficult to grow SiO_x nanowires by using spherical nanoparticles of larger size. The reason is attributed to the decrease in the surface to volume, which gives rise to the fewer active sites for interaction with chemical adsorbate of the precursor materials. Thus, the certain value of FeS at which the melting points of FeO-FeS system lower than 1000 °C is more difficult to reach. Also, due to the same amount of SiO vapor as in the case of 9 nm, it is more difficult to form supersaturation when the size of the particles increased. Thus, only few nanowires can be found in the case of 24 nm spherical nanoparticles.

When using the six-horned octahedra FeO nanoparticles, MoS₂ nanowires were fabricated. The growth mechanism of MoS₂ nanowires is VS mechanism, which has been described in Chapter 3.

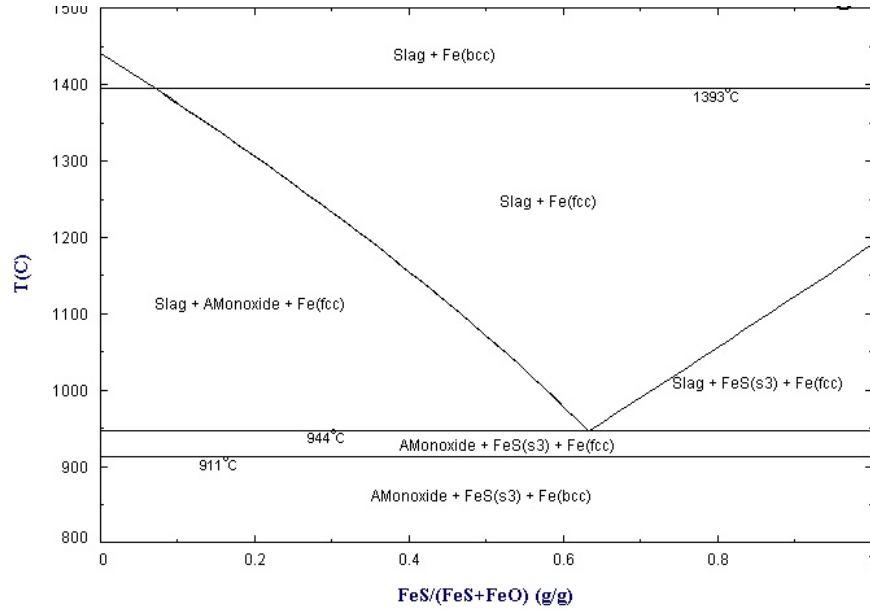


Figure 4-17. Phase diagram of FeO-FeS system.[41]

Above all, we can find that the composition of the nanowires can be drastically affected by the shape of the catalyst nanoparticles. A switching between SiO_x nanowires and MoS₂ nanowires could be found when we changed the shape of the FeO nanoparticles.

4.4 Size effect of the catalysts

The size of the catalyst nanoparticles is also an important consideration in determining the composition and morphology of the nanowires. In the shape effect section, I have used the 9 nm and 24 nm spherical nanoparticles and found that fewer SiO_x nanowires were grown when the size of the nanoparticles increased. In the following

section, I will discuss the size effect of nanoparticles on the MoS₂ nanowires by using six-horned octahedra FeO nanoparticles with different sizes.

The sizes of the nanoparticles I used were 50 nm and 100 nm. The synthesis method and the conditions were shown in the FeO nanoparticles section. After drop-coating substrates with the catalyst solutions, CVD experiments were conducted under the same conditions as the case in 30 nm six-horned octahedra FeO nanoparticles.

Their SEM results are shown in Figures 4-18 (a) and (b), respectively. When used the 50 nm particles, the diameter of the nanowires was about 100-200 nm and the length of the nanowires was about 5 μm . When the diameter of the catalyst particles increased to 100 nm, the diameter of the nanowires was larger than 250 nm and the length of the nanowires was about 5 μm . Compared with results of 30 nm [Figure 3-5, 4-12 (e) and (f)], it is clearly observed that the diameter of the nanowires was increased and the length became shorter.

TEM equipped with EDS was employed to measure the crystal structure and the composition of the nanowires synthesized with 50 nm particles. Figure 4-19 (a) displays the closed top of the nanowire and the composition have been proved to be composed of MoS₂ by EDS [Figure 4-19 (d)]. The same angle as in 30 nm case between the orientation of 100 and the direction of the nanowire indicates the structure of the nanowire is armchair. This similar results as in 30 nm suggests that the composition and structure of the nanowires will not change with size increase.

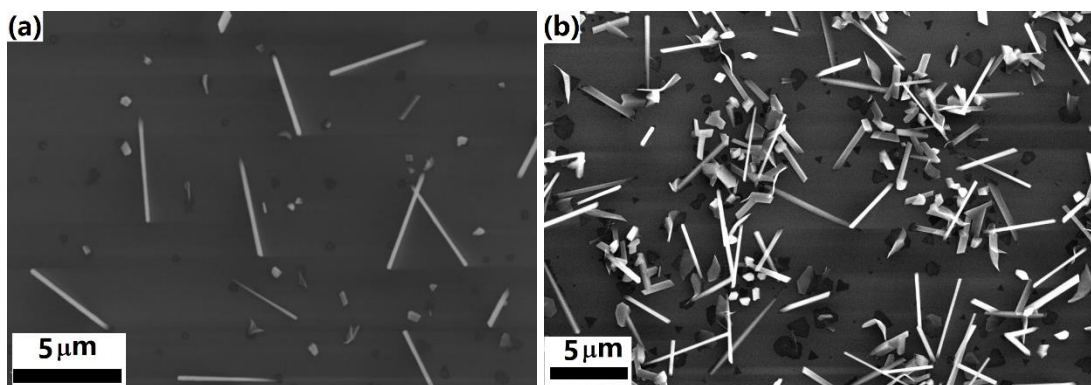


Figure 4-18. SEM images of CVD results with (a) 50 nm and (b) 100 nm FeO particles.

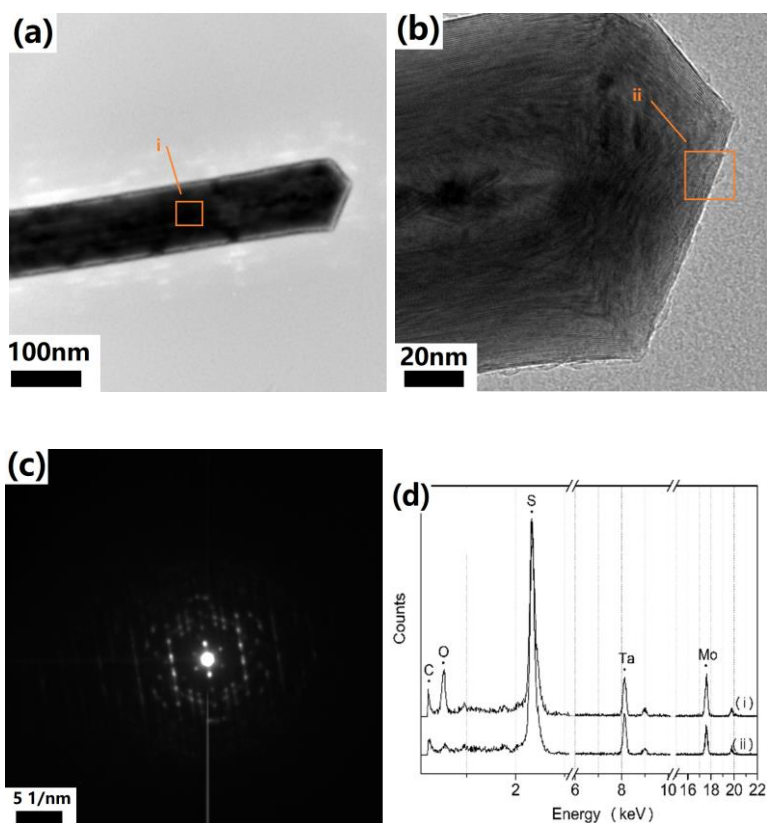


Figure 4-19. (a) TEM image, (b) high magnification TEM image and (c) SAED image of MoS₂ nanowires grown with 50 nm FeO particles. (d) EDS results of the different locations on the nanowire.

4.5 Conclusions

In this Chapter, I have studied the size and shape control of the FeO nanoparticles and their effects on the morphology and composition of the CVD products. Firstly, the effects of factors on the size and shape of the nanoparticles were studied, such as the composition of the mixture, the decomposition temperature and time, and the stirring during the decomposition. It was found that we could control the size and shape of the nanoparticles by regulating the decomposition conditions. Then, the shape effect of the catalysts on the CVD products was studied. The composition of the nanowires can be drastically affected by the shape of the catalyst nanoparticles. When we changed the shape of the FeO nanoparticles, a switching between SiO_x nanowires and MoS₂ nanowires could be found. Finally, the size effect of the catalysts on the CVD products was studied. The composition and structure of the nanowires were not changed with the increased size in catalyst nanoparticles while the aspect ratio became lower when the size of the nanoparticles increased.

References:

1. B.K. Miremadi, R.C. Singh, S.R. Morrison and K. Colbow, *Applied Physics A Materials Science & Processing*, 1996, **63**, 271-275.
2. B. Hinnemann, P.G. Moses, J. Bonde, K.P. Jørgensen, J.H. Nielsen, S. Horch, I. Chorkendorff and J.K. Nørskov, *J. Am. Chem. Soc.*, 2005, **127**, 5308-5309.
3. H. Li, Z. Yin, Q. He, H. Li, X. Huang, G. Lu, D.W.H. Fam, A.I.Y. Tok, Q. Zhang and H. Zhang, *Small*, 2012, **8**, 63-67.

4. Q. He, Z. Zeng, Z. Yin, H. Li, S. Wu, X. Huang and H. Zhang, *Small*, 2012, **8**, 2994-2999.
5. D.J. Late, Y. Huang, B. Liu, J. Acharya, S.N. Shirodkar, J. Luo, A. Yan, D. Charles, U.V. Waghmare, V.P. Dravid and C.N.R. Rao, *ACS Nano*, 2013, **7**, 4879-4891.
6. J. Kim, H. Yoo, H.O. Choi and H. Jung, *Nano Lett.*, 2014, **14**, 5941-5947.
7. S. Cui, Z. Wen, X. Huang, J. Chang and J. Chen, *Small*, 2015, **11**, 2305-2313.
8. B. Cho, M.G. Hahm, M. Choi, J. Yoon, A.R. Kim, Y. Lee, S. Park, J. Kwon, C.S. Kim, M. Song, Y. Jeong, K. Nam, S. Lee, T.J. Yoo, C.G. Kang, B.H. Lee, H.C. Ko, P.M. Ajayan and D. Kim, *Sci. Rep-Uk*, 2015, **5**.
9. Y. Yoon, K. Ganapathi and S. Salahuddin, *Nano Lett.*, 2011, **11**, 3768-3773.
10. K. Alam and R.K. Lake, *Ieee T. Electron Dev.*, 2012, **59**, 3250-3254.
11. H. Wang, L. Yu, Y. Lee, Y. Shi, A. Hsu, M.L. Chin, L. Li, M. Dubey, J. Kong and T. Palacios, *Nano Lett.*, 2012, **12**, 4674-4680.
12. S. Das, H. Chen, A.V. Penumatcha and J. Appenzeller, *Nano Lett.*, 2012, **13**, 100-105.
13. G. Fiori, B.N. Szafraneck, G. Iannaccone and D. Neumaier, *Appl. Phys. Lett.*, 2013, **103**, 233509.
14. Y. Du, H. Liu, A.T. Neal, M. Si and P.D. Ye, *IEEE Electr. Device L.*, 2013, **34**, 1328-1330.
15. X. Xie, D. Sarkar, W. Liu, J. Kang, O. Marinov, M.J. Deen and K. Banerjee, *ACS Nano*, 2014, **8**, 5633-5640.
16. H. Kwon, W. Choi, D. Lee, Y. Lee, J. Kwon, B. Yoo, C.P. Grigoropoulos and S. Kim, *Nano Res.*, 2014, **7**, 1137-1145.

17. J. Wang, X. Zou, X. Xiao, L. Xu, C. Wang, C. Jiang, J.C. Ho, T. Wang, J. Li and L. Liao, *Small*, 2015, **11**, 208-213.
18. H. Yuan, G. Cheng, L. You, H. Li, H. Zhu, W. Li, J.J. Kopanski, Y.S. Obeng, A.R. Hight Walker, D.J. Gundlach, C.A. Richter, D.E. Ioannou and Q. Li, *ACS Appl. Mater. Inter.*, 2015, **7**, 1180-1187.
19. T. Chen, S. Wang, Z. Yang, Q. Feng, X. Sun, L. Li, Z. Wang and H. Peng, *Angew. Chem. Int. Ed.*, 2011, **50**, 1815-1819.
20. S. Tongay, J. Zhou, C. Ataca, K. Lo, T.S. Matthews, J. Li, J.C. Grossman and J. Wu, *Nano Lett.*, 2012, **12**, 5576-5580.
21. J. Lin, C. Chan and S. Chou, *Chem. Commun.*, 2013, **49**, 1440.
22. M. Tsai, S. Su, J. Chang, D. Tsai, C. Chen, C. Wu, L. Li, L. Chen and J. He, *ACS Nano*, 2014, **8**, 8317-8322.
23. S. Lin, X. Li, P. Wang, Z. Xu, S. Zhang, H. Zhong, Z. Wu, W. Xu and H. Chen, *Sci. Rep-Uk*, 2015, **5**.
24. K. Yang, J. Sim, B. Jeon, D. Son, D. Kim, S. Sung, D. Hwang, S. Song, D.B. Khadka, J. Kim and J. Kang, *Progress in Photovoltaics: Research and Applications*, 2015, **23**, 862-873.
25. J. Gao, C.M. Bender and C.J. Murphy, *Langmuir*, 2003, **19**, 9065-9070.
26. J.M. Macák, H. Tsuchiya and P. Schmuki, *Angew. Chem. Int. Ed.*, 2005, **44**, 2100-2102.
27. A. UMAR, M. RAHMAN and Y. HAHN, *Talanta*, 2009, **77**, 1376-1380.
28. L. Kavan, P. Rapta, L. Dunsch, M.J. Bronikowski, P. Willis and R.E. Smalley, *J. Phys. Chem. B*, 2001, **105**, 10764-10771.

29. M.S. Strano, C.B. Huffman, V.C. Moore, M.J. O'Connell, E.H. Haroz, J. Hubbard, M. Miller, K. Rialon, C. Kittrell, S. Ramesh, R.H. Hauge and R.E. Smalley, *J. Phys. Chem. B*, 2003, **107**, 6979-6985.
30. K. Khoo, M. Mazzoni and S. Louie, *Phys. Rev. B*, 2004, **69**.
31. M.Y. Han, B. Ozyilmaz, Y. Zhang and P. Kim, *Phys. Rev. Lett.*, 2007, **98**, 206805.
32. W. An and C.H. Turner, *J. Phys. Chem. Lett.*, 2010, **1**, 2269-2273.
33. Y. Chen, D.G. de Oteyza, Z. Pedramrazi, C. Chen, F.R. Fischer and M.F. Crommie, *ACS Nano*, 2013, **7**, 6123-6128.
34. S. Kurian, H. Seo and H. Jeon, *J. Phys. Chem. C*, 2013, **117**, 16811-16819.
35. M. Weng, T. Yanase, F. Uehara, S. Watanabe, T. Miura, T. Nagahama and T. Shimada, *CrystEngComm*, 2017, **19**, 3915-3920.
36. Y. Hou, Z. Xu and S. Sun, *Angew. Chem.*, 2007, **119**, 6445-6448.
37. B. Pal and M. Sharon, *Thin Solid Films*, 2000, 379, 83-88.
38. ULVAC Inc., *Vacuum Handbook*, Ohm-sha; Tokyo, 2002.
39. J.L. Lensch-Falk, E.R. Hemesath, D.E. Perea and L.J. Lauhon, *J. Mater. Chem.* 2009, **19**, 849.
40. C.Y. Wen, M.C. Reuter, J. Tersoff, E.A. Stach and F.M. Ross, *Nano Lett.*, 2010, **10**, 514-519.
41. FEOxCN-FACT high-T oxycarbontrude databases.

Chapter 5. Other factors for the MoS₂ nanowires control

5.1 Introduction

In Chapter 3 and 4, I have fabricated the MoS₂ nanowires on the SiO₂/Si substrates by catalytic CVD and discussed the size and shape effects of the catalyst nanoparticles on the morphology and composition of the nanowires. While the catalysts morphology is an important prerequisite, many other factors such as the surface of the substrates, the heating reaction temperature and the growth time can also play crucial roles in determining the physical and chemical structures of the nanowires.

5.2 Surface pretreatments of the substrates

In our experiments, the 285 nm SiO₂/Si substrates were used with only RCA-cleaning [1], by which the metal impurities on the substrates could be moved. The solution of FeO nanoparticles was dropped onto the substrates directly before the CVD process. However, in most cases, the MoS₂ nanowires tended to be grown at the edge and the corner of the substrates and the nanowires grown on the middle of the surface were thicker than the one in the edge, as shown in Figure 5-1. It suggested that the nanoparticles dropped on the substrates were aggregated on the surface because of the higher surface energy and most of catalysts on the substrate surface were lost their catalytic activities due to the aggregation.

This would lead to the low yield of the MoS₂ nanowires. Thus, the surface treatment of the substrates needs to be studied.

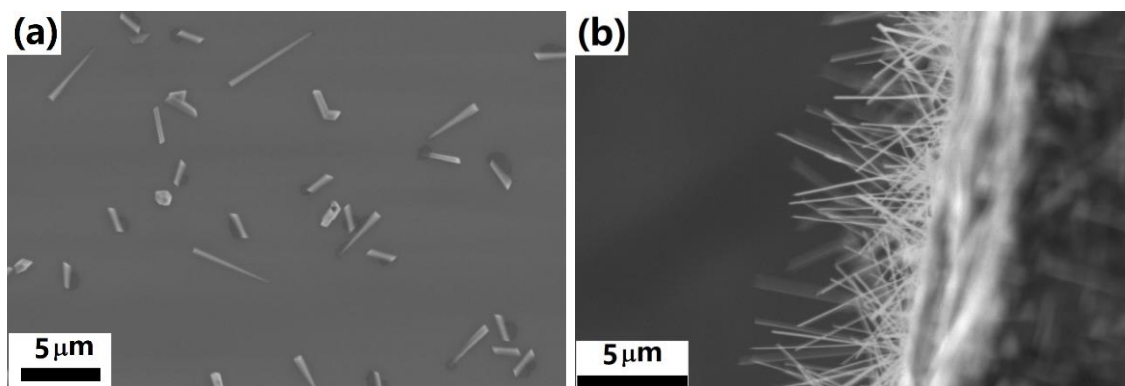


Figure 5-1. SEM images of MoS₂ nanowires grown on the (a) surface and (b) edge of the substrates.

Various methods of surface pretreatment have been reported in literature [2-33], such as plasma deposition, plasma etching, chemical etching or coating adhesives. The sections below will provide the results after different treatments of the substrate surfaces.

5.2.1 Plasma deposition of Al₂O₃

MoS₂ monolayer has been reported [38-40] to grow on both the substrates made of SiO₂ and Al₂O₃. In our previous experiment, we have found that the monolayer of MoS₂ could be grown in a large area when we used Al₂O₃ substrates instead of Si wafers with thermal oxide. The plasma deposition is a method to increase the surface roughness [2-11]. The trial of using Al₂O₃ deposited substrates is seemed to be feasible.

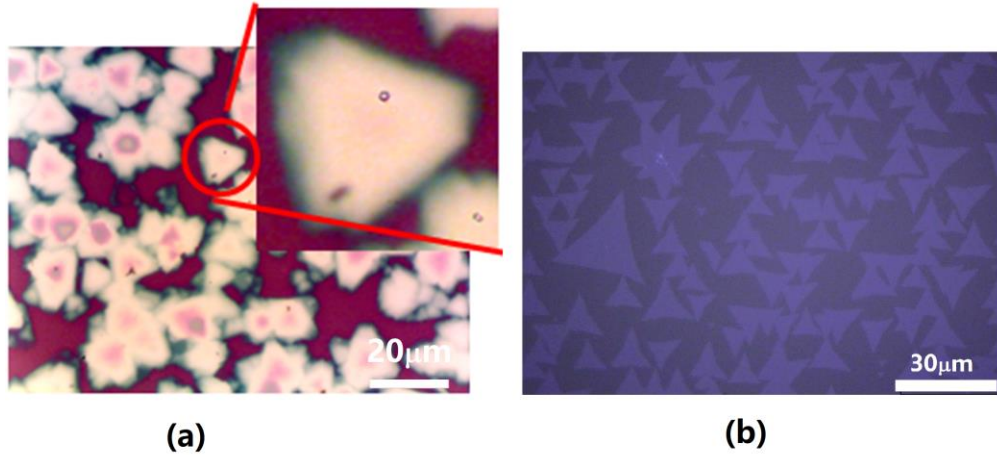


Figure 5-2. Optical images of the MoS₂ monolayer grown on (a) SiO₂/Si [12] and (b) Al₂O₃ substrates.

The substrates coated with Al₂O₃ were prepared by sputtering. The schematic image of the vacuum chamber is shown in Figure 5-3. The pressure of chamber was lowered to 10⁻⁴ Pa by using turbo molecular pump (TMP) before the deposition process. Then, the deposition was taken place under the Ar atmosphere and the flow rate of the Ar was 15 sccm. The pressure of the chamber was kept at 18 Pa. A ratio-frequency magnetron sputtering gun (13.56MHz, 80 W) equipped with an Al₂O₃ plate target was used to produce stable plasma glow. The supporting gun was set facing the substrate to direct deposition of sputtering Al₂O₃. The deposition time was 30 min.

Using the Al₂O₃ coated substrates, CVD experiment was taken after dropping the catalyst particles on the substrates. It should be noted here, one corner of the substrates were not coated by Al₂O₃ because of the shadowing by cramping screws. The SEM images of the results in two locations are shown in Figure 5-4. Figure 5-4(a) is the image located in the Al₂O₃ coated surface and Figure 5-4 (b) is a non-coated location. We can see no nanowires were grown on the surface of Al₂O₃ coated substrate; instead, standing thin films

were grown, indicating the composition of Al₂O₃ could be hindering the catalytic activities of FeO nanoparticles.

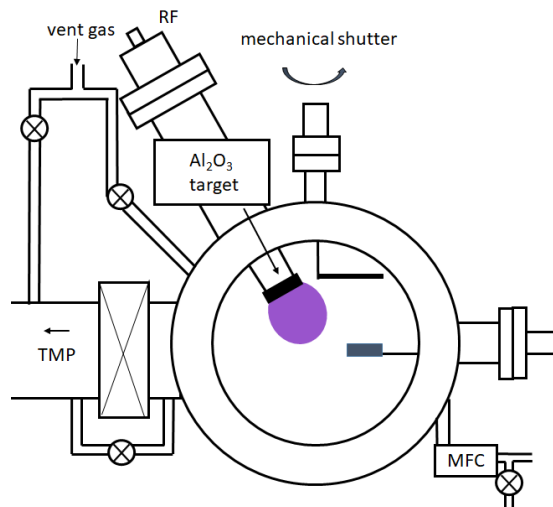


Figure 5-3. Scheme of the deposition chamber.

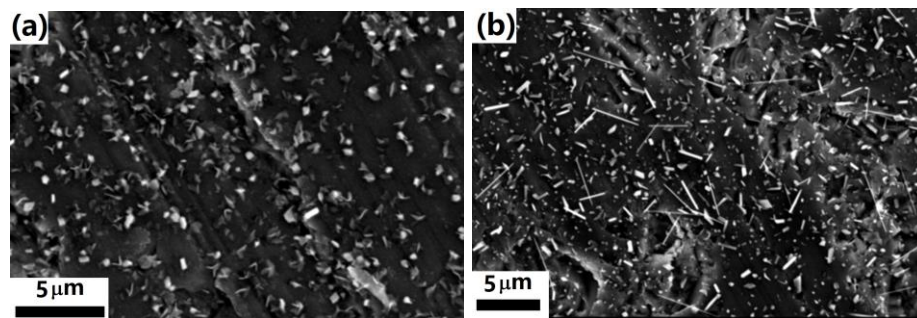


Figure 5-4. SEM images of the CVD results located at (a) Al₂O₃ coated and (b) non-Al₂O₃ coated substrates.

The reason for this result is still under investigation, but I propose a tentative model here. I searched stable compounds in M-Fe-O system (M: Al, Si) in the ICSD.[13] The compounds such as FeAl₂O₄ spinel (Figure 5-5) and so on were found in the Al-Fe-O system. On the other hand, no stable compounds were found in Si-Fe-O system.

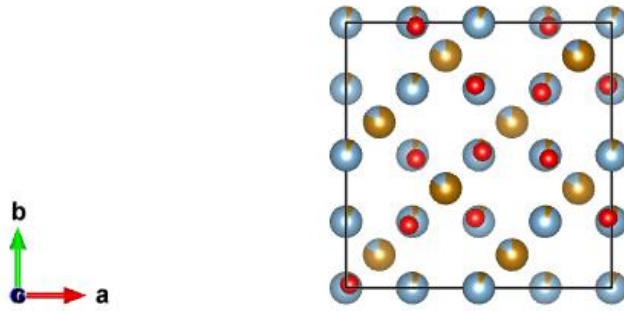


Figure 5-5. One structure (FeAl₂O₄ spinel) of Al-Fe-O compounds.

5.2.2 Plasma etching

Plasma etching is a method aiming at etching the surface uniformly by plasma process [14-20]. As reported, many plasma parameters have effect on the roughness of the substrates such as the pressure, the ion fluence and temperature and so on. For example, the surface will be smoothed at low ion fluence with neutrals, while the surface will become rough at the high ion fluence with neutrals [17]. In our experiment, for the purpose to increase the roughness of the substrate surface, Ar mixed with H₂ gas was chosen to irradiate protons to the surface. The pressure was set at 6.0 kPa.

The microwave plasma equipment uses a microwave (2.45GHz) antenna as the sample holder (AR105 DCVD-51A-SSP) [21]. 80 sccm Ar mixed with 20 sccm H₂ gas (purity 99.95%) was introduced into the chamber. The pressure of the chamber was 6.0 kPa and the etching time was 24 h. The schematic image of the apparatus is shown in Figure 5-6. A laser microscope (Keyence VK-8710) and FESEM were employed to observe the surface morphology of the substrates.

The surface roughness images are shown in Figure 5-7. It can be seen that the surface roughness of the substrate was increased obviously. From the FESEM image, we could found that the pores of the substrate surface were larger than 100 nm. By using the plasma-etched substrates, CVD was performed to fabricate the MoS₂ nanowires. The SEM results are shown in Figure 5-8. It could be seen that the growth density was increased and the aspect ratio of the nanowires was improved indicating that the aggregation of the catalyst particles could be presented effectively.

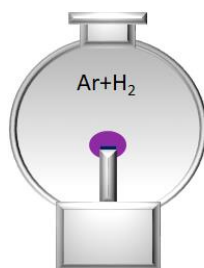


Figure 5-6. Scheme of the plasma chamber.

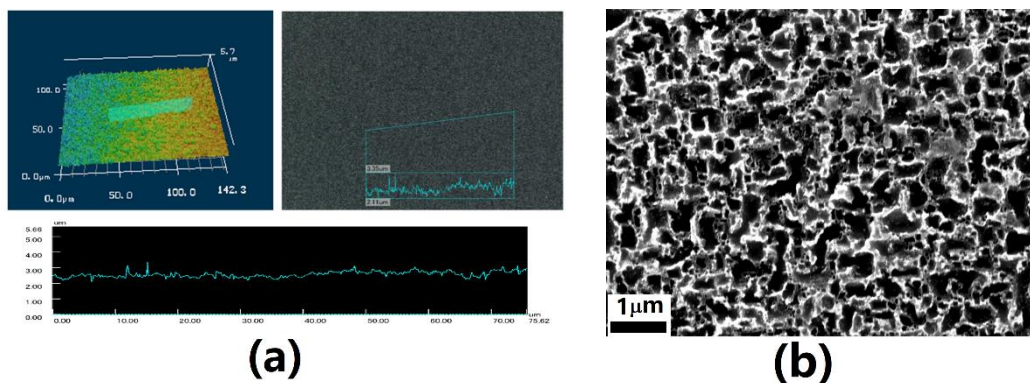


Figure 5-7. Surface morphology of the substrate after plasma etching: (a) laser microscope images (ID=profile along a line) and (b) FESEM image.

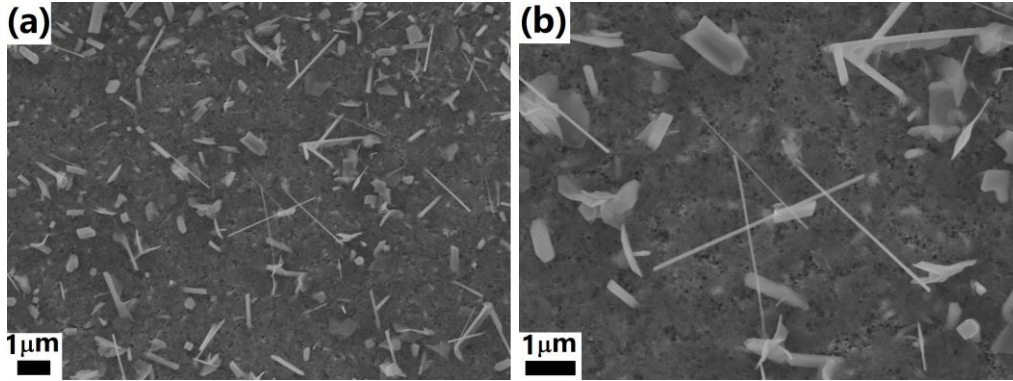


Figure 5-8. (a) SEM image and (b) the high magnification image of CVD results by using the plasma-etched substrates.

5.2.3 Chemical etching in alkaline solution

The chemical etching of silicon have been studied for many years [22-30]. Among them, the use of alkaline solutions attached considerable attention. (110) surface of the silicon substrates could be obtained by etching the (100) surface using the KOH solution with isopropyl alcohol [23-26]. The roughness of the substrates and the etched rates could be controlled by regulating the concentrations of KOH or alcohol. Kramkowska et al [26] have studied the concentration effect of isopropyl alcohol (IPA) in KOH solution on the etching results of the (100) silicon substrates. They found that the best morphology of (110) surface could be achieved when using 5M KOH+0.4M IPA or 3M KOH +1M IPA.

In this experiment, I used the solution with 3M KOH +1M IPA. The substrates were 285 nm SiO₂/Si substrates. The etching experiment was taken place at the temperature of 75 °C with string. Figure 5-9 displays the schematic image of the etched surface.

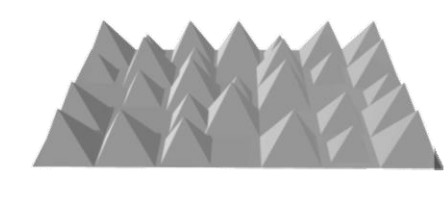


Figure 5-9. Schematic image of the substrate surface after chemical etching.

After the chemical etching process, RCA cleaning [1] of the substrates was used to remove the residues. Catalytic CVD experiment was taken after dropping the 30 nm six-horned octahedral FeO nanoparticles on the etched substrates. Figure 5-10 shows the results after CVD. The nanowires were fabricated in the length of 2-5 μm and in the diameter of 180-230 nm. Compared to the one grown on substrates without pretreatment, the aspect ratio of the 1D nanostructures was not improved but decreased, indicating (100) surface of silicon substrate performs better in the catalytic growth of 1D MoS₂ nanostructures.

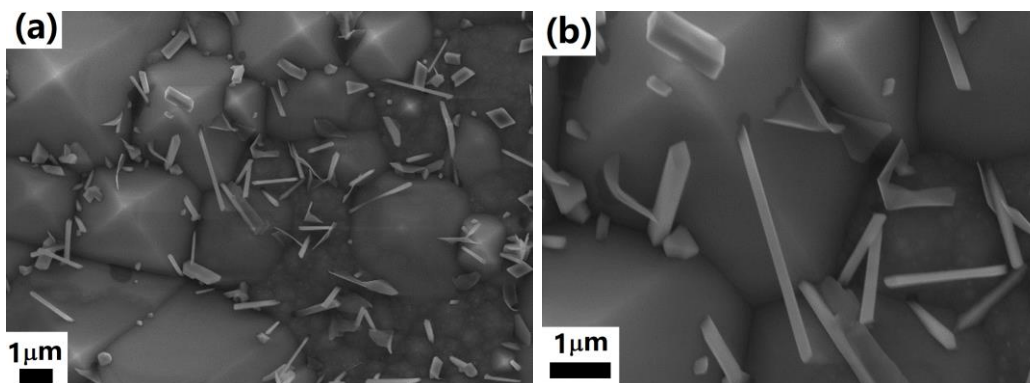


Figure 5-10. (a) SEM image and (b) the high-magnification SEM image of the CVD results using the chemical etched substrates.

5.2.4 Carbon coating

Coating adhesive on the substrates is a method to increase the surface roughness, promoting the dispensation of the catalyst particles on the substrate surface [31-37]. The coating material in our experiment was porous carbon. The wide applications of the porous carbon materials have been reported [41-46], such as water purification, gas separation and catalyst supports, due to its unique structures. In our experiment, the reasons to choose it as the coating adhesive are as follows:

- (1) The pores in the carbon materials facilities the dispersion of the nanoparticles.
- (2) Carbon materials are stable even at the temperature as high as 1000 °C.

The carbon coating method is described as follows and the flow chart is given in Figure 5-11.

- (1) 5.5 g Resorcinol [C₆H₄(OH)₂] was added into 41 ml alcohol (C₂H₅OH) and the mixture was kept in a warm water for 5 min to form a transparent solution;
- (2) 5.6 ml formaldehyde (HCHO) was added into the solution and the mixture was stirred in the room temperature for 10 min;
- (3) 1.1 ml HCl and 1.6 ml ultrapure water were added into the solution and the mixture was kept stirring for 1 hour to form resorcinol-formaldehyde (RF) gel;
- (4) 20 µl RF gel was dropped on the RCA-cleaned SiO₂/Si substrates and evaporated at 90 °C for 5h;
- (5) The substrates were annealed at 900 °C for 10h.

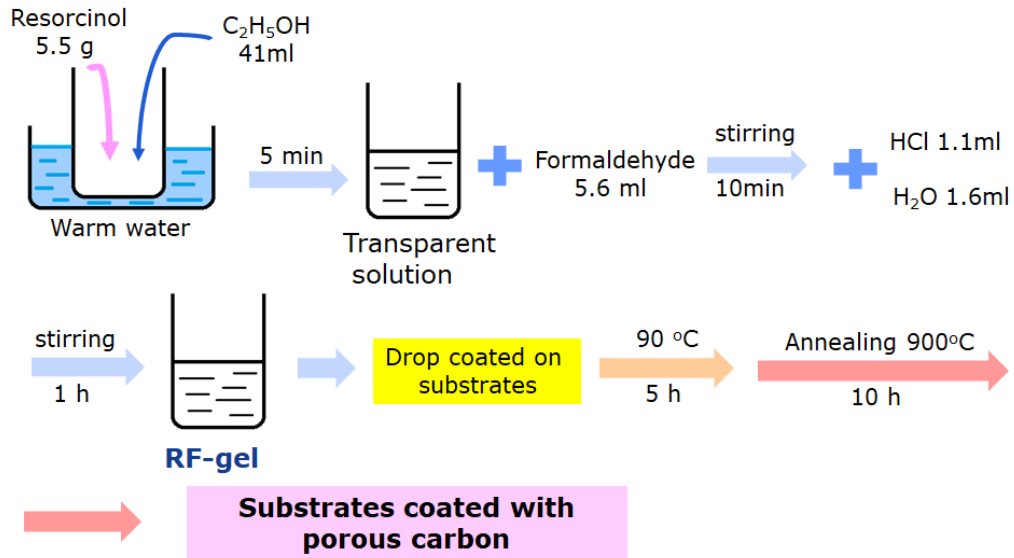


Figure 5-11. Flow chart of the carbon coating method.

The morphology of the porous carbon surface was observed by FESEM, as shown in Figure 5-12. It can be seen that the size of the pores on the surface was smaller than 100 nm.

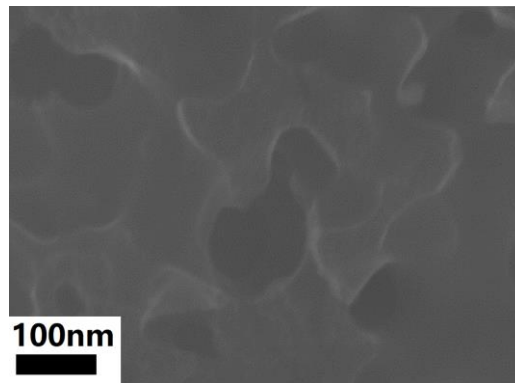


Figure 5-12. FESEM image of the porous carbon surface.

CVD experiment was taken place after coating the treated substrates with FeO particles. Figure 5-13 shows the SEM images of the CVD results. It can be seen from the images that the growth density of MoS₂ nanowires on the substrate surface was greatly

improved compared to Figure 5-1(a). The diameter of these nanowires was around 40 nm [Figure 5-13(b)] and the length of them was up to 12 μm .

In order to confirm that the growth of MoS₂ nanowires was not due to the catalytic activity of the porous carbon material, I conducted a CVD experiment without drop-coating FeO nanoparticles. Figure 5-14 shows the CVD result. No nanowires could be found on the substrates, instead, particles and small thin films were grown. This result indicates that the porous carbon coated on the silicon substrates cannot be the catalyst for the growth of MoS₂ nanowires.

It is of great interest to investigate the role of porous carbon played in the synthesis of the MoS₂ nanowires. The improved growth density and the thinner size of the nanowires demonstrate that dispensation of the FeO nanoparticles has been promoted. The increased surface roughness of the substrate by the carbon adhesive attained to the surface of the substrates and the pores of the carbon material itself are suggested to be responsible for the improved dispensation of the FeO catalyst.

Compared to the results of plasma etching method (Figure 5-8), the higher growth density of the nanowires suggests that the carbon coating method is more effective than the plasma etching method in the dispersion of the catalyst nanoparticles for the growth of MoS₂ nanowires.

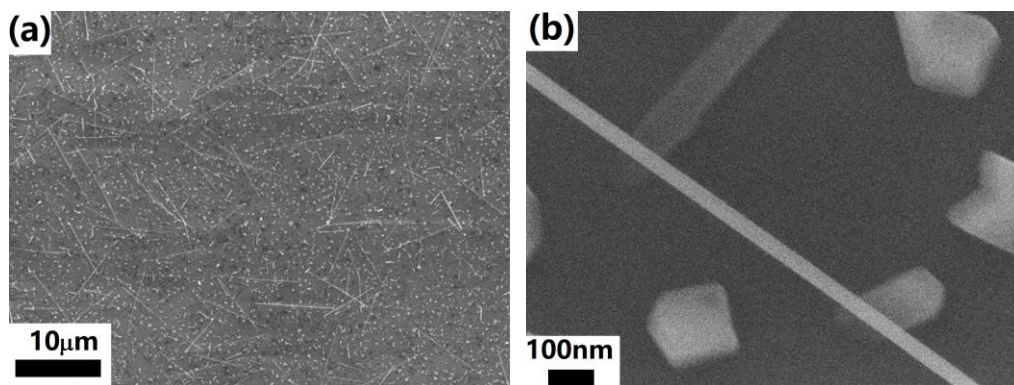


Figure 5-13. (a) SEM image and (b) the high-magnification SEM image of the CVD results using the carbon coated substrates.

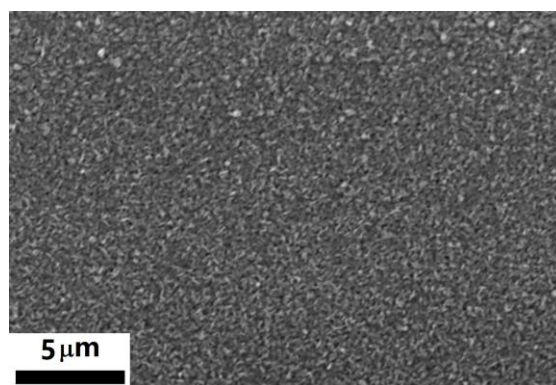


Figure 5-14. SEM image of the CVD result using the carbon coated substrates without FeO catalyst nanoparticles.

Summarizing the results of substrates with pretreatments, both of the plasma etching and the porous carbon coating methods can promote the dispersion of FeO catalyst nanoparticles, while the methods of depositing Al₂O₃ and chemical etching roughening of the substrates cannot facilitate the catalyst particle dispersion, and even hinder the growth of MoS₂ nanowires. These results indicate that the substrate composition and morphologies are important for the growth of MoS₂ nanowires.

5.3 Growth temperature

Lieber et al. have obtained a very special structure of the Si nanowires [Figure 5-15] by changed the growth pressure of Si nanowires. As they reported [47, 48], when the pressure was changed, the vapor pressure of the Si was also changed and the nanowires would tend to grow in to a stable lattice plane, giving rise to the special structure of the Si nanowires. Such structure can be used as localized bioprobes with field effect transistor (FET) functions.

It is also reported that temperature also affect the growth [49]. As I mentioned in Chapter 3, MoS₂ nanowires were grown in two steps, the nucleation and the growth. The growth temperature is an important factor to affect the catalysts activity of the nanoparticles and the deposition rate of the precursor materials. The growth of the MoS₂ is by the sequenced deposition of the precursor materials. Thus, it is of great interest to investigate the morphology of the nanowires when the growth temperature changed during the growth process.

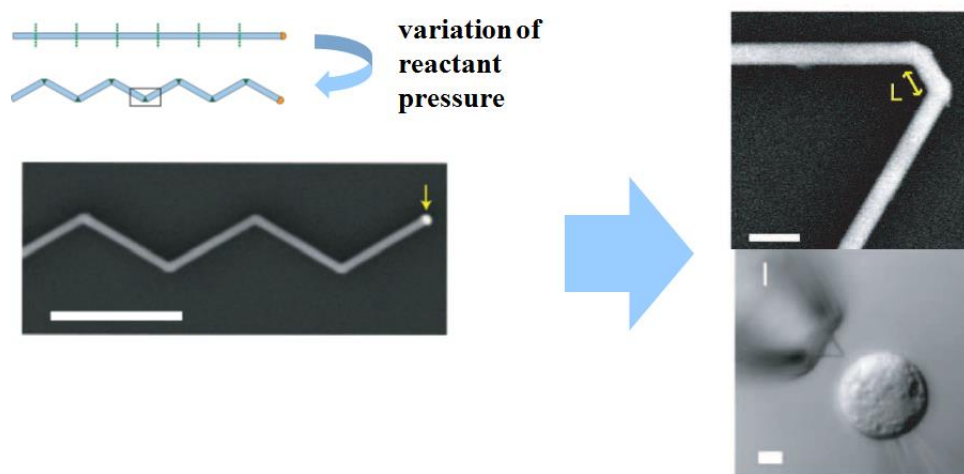


Figure 5-15. Special structure of Si nanowires obtained by Lieber et al. [47, 48]

CVD experiments were taken with changing the growth temperatures. One of the experiment was conducted using the raised temperature and the other one used the decreased temperature, as shown in Figure 5-16.

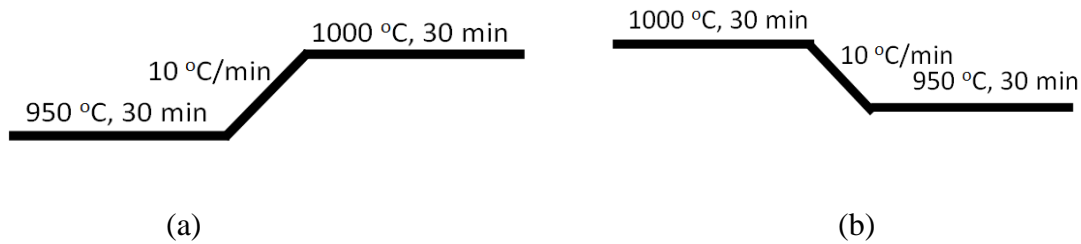


Figure 5-16. Two temperature changing process.

The CVD results are given in Figure 5-17. First, it is obviously observed that the density of the nanowires was totally different. In the case of 950 °C to 1000 °C, the density was lower than the case of 1000 °C to 950 °C, indicating that the catalyst activity was lower at 950 °C. One can find a change in diameter of nanowires in the high magnification image [Figure 5-17(b) and (d)]. In the case of 950 °C to 1000 °C, it is from thick to thin, and in the case of 1000 °C to 950 °C, it is thin to be thick. From the results of changing temperatures, I concluded that we could control the diameter and the growth density of the nanowires by controlling the temperature.

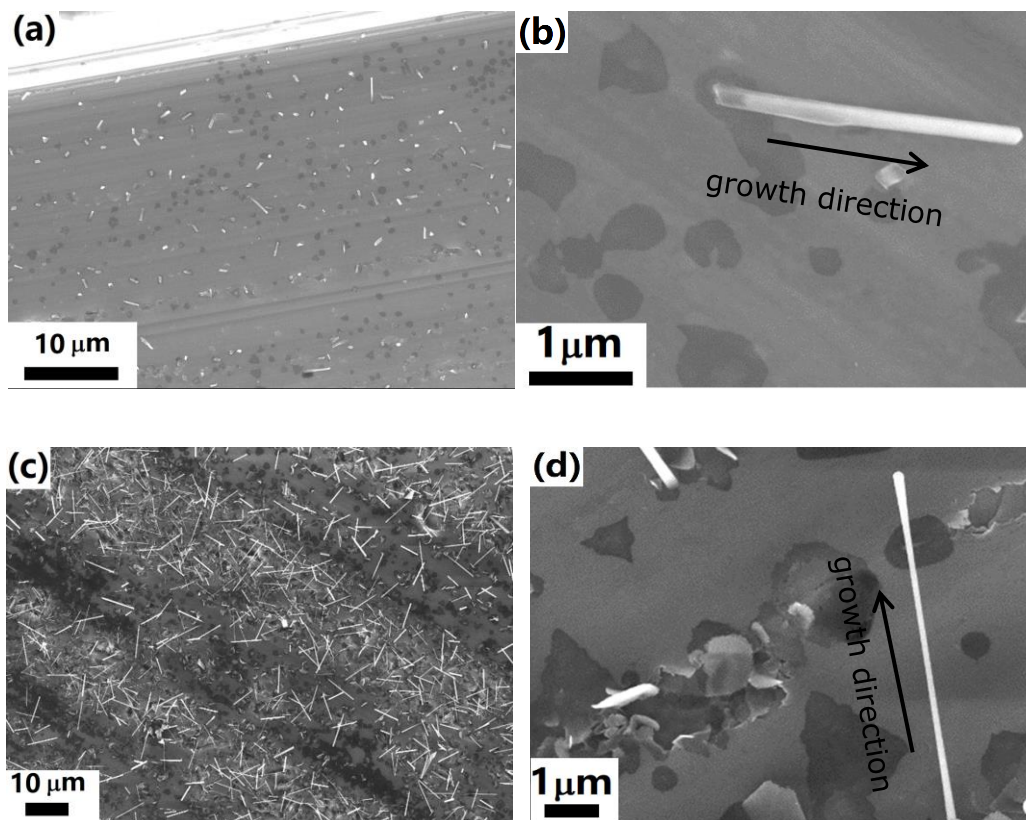


Figure 5-17. (a) SEM image and (b) high magnification SEM image of the CVD results with the temperature changed from 950 °C to 1000 °C. (c) SEM image and (d) high magnification SEM image of the CVD results with the temperature changed from 1000 °C to 950 °C.

5.4 Growth time

In Chapter 3, we have found that the growth mechanism of MoS₂ nanowires is VS. Thus it is important to investigate the morphology of the nanowires during the different time region. In this section, I will investigate the morphologies of the products with different growth time when using carbon coated substrates with 50 nm six-horned octahedra FeO particles.

CVD experiments were taken with the different growth time: 30 min and 1h. Figure 5-18 (a) and (b) show the SEM images of the CVD results grown in 30 min and 1h, respectively. When the growth time was 30 min, the diameter of the nanowires was about 100-200 nm and the length of the nanowires was about 1 μm . When the growth time increased to 60 min, the diameter of the nanowires was about 100-200 nm and the length of them was about 10 μm . It can be clearly found that the length of the nanowires became longer when the time increased from 30 min to 1h, indicating that we can control the length of MoS₂ nanowires by the set of growth time. Furthermore, the high density of the nanowires indicates that the carbon coated method can promote the dispersion of 50 nm six-horned octahedra FeO particles.

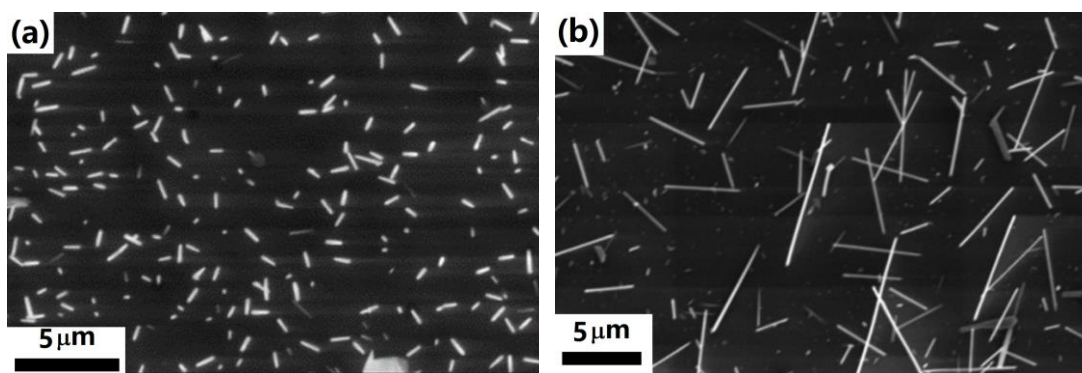


Figure 5-18. SEM images of the CVD results grown in (a) 30 min and (b) 60 min.

5.5 Conclusions

In this Chapter, I have tried to improve the growth density of MoS₂ nanowires by treated the substrate surface with various methods. I found that the composition and structure of substrate surface are important for the growth of MoS₂ nanowires. Among the

used treatments, both of the plasma etching and the porous carbon coating methods can promote the dispersion of FeO catalyst nanoparticles, while the methods of depositing Al₂O₃ and chemical etching cannot facilitate the catalyst particle dispersion, even hinder the growth of MoS₂ nanowires. I also studied the effects of growth temperature and time on the growth of MoS₂ nanowires. It was found that the diameter and length of the nanowires could be controlled by setting the growth temperature and time.

References:

1. W. Kern, *J. Electrochem. Soc.*, 1990, **137**, 1887-1892.
2. V.I. Konov, A.A. Smolin, V.G. Ralchenko, S.M. Pimenov, E.D. Obraztsova, E.N. Loubnin, S.M. Metev and G. Sepold, *Diam. Relat. Mater.*, 1995, **4**, 1073-1078.
3. X.L. Peng, Z.H. Barber and T.W. Clyne, *Surface and Coatings Technology*, 2001, **138**, 23-32.
4. M.C. Salvadori, D.R. Martins and M. Cattani, *Surface and Coatings Technology*, 2006, **200**, 5119-5122.
5. R. Thielsch, A. Gatto, J. Heber and N. Kaiser, *Thin Solid Films*, 2002, **410**, 86-93.
6. E. Gogolides, V. Constantoudis, G. Kokkoris, D. Kontziampasis, K. Tsougeni, G. Boulousis, M. Vlachopoulou and A. Tserepi, *J. Phys. D: Appl. Phys.*, 2011, **44**, 174021.
7. S. De Wolf, G. Agostinelli, G. Beaucarne and P. Vitanov, *J. Appl. Phys.*, 2005, **97**, 63303.
8. C.C. Tsai, J.C. Knights, G. Chang and B. Wacker, *J. Appl. Phys.*, 1986, **59**, 2998-3001.
9. K. Kim, S. Yoon, W. Lee and K. Ho Kim, *Surface and Coatings Technology*, 2001, **138**, 229-236.

10. K. Miyoshi, R.L.C. Wu, A. Garscadden, P.N. Barnes and H.E. Jackson, *J. Appl. Phys.*, 1993, **74**, 4446-4454.
11. K. Ellinas, A. Tserepi and E. Gogolides, *Langmuir*, 2011, **27**, 3960-3969.
12. T. Yanase, S. Watanabe, M. Weng, T. Nagahama, and T. Shimada, *J. Nanosci. Nanotechnol.*, 2016, **16**, 3223-3227.
13. G. Bergerhoff and I.D. Brown, in “Crystallographic Databases”, F.H. Allen et al. (ed.) Chester, International Union of Crystallography, (1987).
14. Y. Nakamura, Y. Suzuki and Y. Watanabe, *Thin Solid Films*, 1996, **290**, 367-369.
15. C.L. Lee, E. Gu, M.D. Dawson, I. Friel and G.A. Scarsbrook, *Diam. Relat. Mater.*, 2008, **17**, 1292-1296.
16. N. Agarwal, S. Ponoth, J. Plawsky and P.D. Persans, *Appl. Phys. Lett.*, 2001, **78**, 2294-2296.
17. M. Li, G.C. Wang and H.G. Min, *J. Appl. Phys.*, 1998, **83**, 5313-5320.
18. J. Fujita, Y. Ohnishi, Y. Ochiai and S. Matsui, *Appl. Phys. Lett.*, 1996, **68**, 1297-1299.
19. K. Zhu, V. Kuryatkov, B. Borisov, J. Yun, G. Kipshidze, S.A. Nikishin, H. Temkin, D. Aurongzeb and M. Holtz, *J. Appl. Phys.*, 2004, **95**, 4635-4641.
20. M. Li, G.C. Wang and H.G. Min, *J. Appl. Phys.*, 1998, **83**, 5313-5320.
21. T. Tamura, T. Takami, T. Yanase, T. Nagahama and T. Shimada, *Jpn. J. Appl. Phys.*, 2017, **56**, 06HF01.
22. C. Chartier, S. Bastide and C. Lévy-Clément, *Electrochim. Acta*, 2008, **53**, 5509-5516.
23. Z. Huang, N. Geyer, P. Werner, J. de Boor and U. Gösele, *Adv. Mater.*, 2011, **23**, 285-308.
24. X. Li and P.W. Bohn, *Appl. Phys. Lett.*, 2000, **77**, 2572-2574.

25. M. Zhang, K. Peng, X. Fan, J. Jie, R. Zhang, S. Lee and N. Wong, *J. Phys. Chem. C*, 2008, **112**, 4444-4450.
26. M. Steinert, J. Acker, M. Krause, S. Oswald and K. Wetzig, *J. Phys. Chem. B*, 2006, **110**, 11377-11382.
27. I. Zubel and I. Barycka, *Sensors and Actuators A*, 1998, **70**, 250-259.
28. I. Zubel, I. Barycka, K. Kotowska and M.G. Kramkowska, *Sensors and Actuators A: Physical*, 2001, **87**, 163-171.
29. J.E.A.M. van den Meerakker, *Electrochim. Acta*, 1990, **35**, 1267-1272.
30. I. Zubel, K. Rola and M. Kramkowska, *Sensors and Actuators A: Physical*, 2011, **171**, 436-445.
31. D. Hegemann, H. Brunner and C. Oehr, *Nuclear Instruments and Methods in Physics Research Section B: Beam Interactions with Materials and Atoms*, 2003, **208**, 281-286.
32. R. Jones, H.M. Pollock, J.A.S. Cleaver and C.S. Hodges, *Langmuir*, 2002, **18**, 8045-8055.
33. W. Chen, Y. Liu, H.S. Courtney, M. Bettenga, C.M. Agrawal, J.D. Bumgardner and J.L. Ong, *Biomaterials*, 2006, **27**, 5512-5517.
34. B. Min, G. Lee, S.H. Kim, Y.S. Nam, T.S. Lee and W.H. Park, *Biomaterials*, 2004, **25**, 1289-1297.
35. A. Della Bona, *Dent. Mater.*, 2004, **20**, 338-344.
36. L. Le Guéhennec, A. Soueidan, P. Layrolle and Y. Amouriq, *Dent. Mater.*, 2007, **23**, 844-854.
37. J. Forsgren, F. Svahn, T. Jarmar and H. Engqvist, *Acta Biomater*, 2007, **3**, 980-984.

38. A. Splendiani, L. Sun, Y. Zhang, T. Li, J. Kim, C. Chim, G. Galli and F. Wang, *Nano Lett.*, 2010, **10**, 1271-1275.
39. Y. Yu, C. Li, Y. Liu, L. Su, Y. Zhang and L. Cao, *Sci Rep-Uk*, 2013, **3**.
40. S. Wu, C. Huang, G. Aivazian, J.S. Ross, D.H. Cobden and X. Xu, *ACS Nano*, 2013, **7**, 2768-2772.
41. T. Horikawa, N. Sakao, T. Sekida, J.I. Hayashi, D.D. Do and M. Katoh, *Carbon*, 2012, **50**, 1833-1842.
42. D.R. Simpson, *Water Res.*, 2008, **42**, 2839-2848.
43. S.M. Saufi and A.F. Ismail, *Carbon*, 2004, **42**, 241-259.
44. D. Jiang, V.R. Cooper and S. Dai, *Nano Lett.*, 2009, **9**, 4019-4024.
45. R. Banerjee, H. Furukawa, D. Britt, C. Knobler, M. O Keeffe and O.M. Yaghi, *J. Am. Chem. Soc.*, 2009, **131**, 3875-3877.
46. P. Nugent, Y. Belmabkhout, S.D. Burd, A.J. Cairns, R. Luebke, K. Forrest, T. Pham, S. Ma, B. Space, L. Wojtas, M. Eddaoudi and M.J. Zaworotko, *Nature*, 2013, **495**, 80-84.
47. B. Tian, T. Cohen-Karni, Q. Qing, X. Duan, P. Xie and C.M. Lieber, *Science*, 2010, **329**, 830-834.
48. B. Tian, P. Xie, T.J. Kempa, D.C. Bell and C.M. Lieber, *Nat. Nanotechnol.*, 2009, **4**, 824-829.
49. Z. Pan, S. Dai, D.B. Beach and D.H. Lowndes, *Nano Lett.*, 2003, **3**, 1279-1284.

Chapter 6. General Conclusions

In this thesis, I have successfully synthesized MoS₂ nanowires by catalytic CVD with FeO nanoparticles and controlled the aspect ratio and growth density of the nanowires.

In Chapter 2, I have found that only FeO can be catalyst for the growth of MoS₂ nanowires in the iron and iron oxides group. SEM, TEM and Raman were employed to characterize the composition and the structure of the MoS₂ nanowires. The length of the nanowires could be up to 9.6 μm but the diameter was larger than 150 nm. The catalytic activities of other transitional metal oxides nanoparticles (MnO, CuO, NiO and Cu₂O) were also searched. It was found that NiO and Cu₂O could promote the growth of 1D MoS₂ nanostructures but MnO, CuO could not. Comparing the CVD results of FeO, NiO and Cu₂O particles, FeO had the best catalytic activity for the growth of MoS₂ nanowires.

In Chapter 3, I have successfully synthesized the 30 nm six-horned FeO nanoparticles and used it as the catalyst for the growth of MoS₂ nanowires. SEM, FESEM, XRD, Raman and TEM were used to characterize the morphology and the structure of the FeO nanoparticles and MoS₂ nanowires. It was found that the nanowires were multilayered and had a hollow structure. The cross section of the nanowire was in rectangular shape and the end was closed. The direction of S-S (or Mo-Mo) nearest neighbor was found to be parallel to the orientation of the nanowire indicating that the nanowires were in armchair structure. The growth mechanism of the nanowires was proved to be in VS growth.

In Chapter 4, I have studied on the size and shape control of the FeO nanoparticles and their effects on the morphology and composition of the CVD products. Firstly, the effect of factors on the size and shape of the nanoparticles, such as the composition of the

mixture, the decomposition temperature and time, and the stirring during the decomposition. It was found that we can control the size and shape of the nanoparticles by regulating the decomposition conditions. Then, the shape effect of the catalysts on the CVD products were studied. The composition of the nanowires can be drastically affected by the shape of the catalyst nanoparticles. When I changed the shape of the FeO nanoparticles, a switching between SiO_x nanowires and MoS₂ nanowires was observed. Finally, the size effect of the catalysts on the CVD products was studied. The composition and structure of the nanowires were not changed with the increased size in catalyst nanoparticles while the aspect ratio became lower when the size of the nanoparticles increased.

In Chapter 5, I have tried to improve the growth density of MoS₂ nanowires by treated the substrate surface with various methods. I found that the composition and structure of substrate surface were important for the growth of MoS₂ nanowires. Among the used treatments, both of the plasma etching and the porous carbon coating methods can promote the dispersion of FeO catalyst nanoparticles, while the Al₂O₃ deposition and chemical etching of the substrates cannot facilities the catalyst particle dispersion, but even hinder the growth of MoS₂ nanowires. I also studied the effects of growth temperature and time on the growth of MoS₂ nanowires. It was found that the diameter and length of the nanowires could be controlled by setting the growth temperature and time.